CORA Cork Open Research Archive
Cartlann Taighde Oscailte Chorcaí

Title	Spectrally-sliced optical receiver for coherent passive optical networks
Authors	Othman, Muhammad Hilmi
Publication date	2024
Original Citation	Othman, M. H. 2024. Spectrally-sliced optical receiver for coherent passive optical networks. PhD Thesis, University College Cork.
Type of publication	Doctoral thesis
Rights	© 2024, Hilmi Othman. - https://creativecommons.org/licenses/by-nc-nd/4.0/
Download date	2026-11-04 13:54:35
Item downloaded from	https://hdl.handle.net/10468/17409



UCC
University College Cork, Ireland
Coláiste na hOllscoile Corcaigh

Spectrally-sliced Optical Receiver for Coherent Passive Optical Networks

Muhammad Hilmi Othman
MEng
119220038

Thesis submitted for the degree of Doctor of Philosophy



NATIONAL UNIVERSITY OF IRELAND, CORK

School of Engineering and Architecture

Department of ELECTRICAL AND ELECTRONIC ENGINEERING

Tyndall National Institute

Photonics Systems Group

August 2024

Head of Department: Prof. Jorge C. Oliveira

Supervisors: Prof. Paul D. Townsend
Dr Cleitus Antony
Dr Xing Ouyang

Contents

List of Figures . . . iii
List of Tables . . . ix
Acknowledgements . . . xi
Abstract . . . xii

Symbols & Abbreviations **1**

1 Introduction **1**
1.1 Evolution of Passive Optical Network . . . 3
1.2 Evolution of Coherent Optics . . . 4
1.3 Digital Coherent Drivers for Access Network . . . 5
1.4 Objectives . . . 8
1.5 Thesis overview . . . 9

2 Coherent systems for optical communication **11**
2.1 Theory & Operation of Digital Coherent Optics . . . 11
2.1.1 Digital Modulation . . . 12
2.1.2 Optical Coherent Transmitter . . . 13
2.1.3 Optical Coherent Receiver . . . 15
2.2 Noise & Channel Impairments . . . 17
2.2.1 Receiver Noises . . . 17
2.2.2 Optical Fiber Linear & Nonlinear Propagation . . . 18
2.2.3 Polarization Mode Delay . . . 21
2.2.4 Phase Noise . . . 21
2.3 Post-Digital Signal Processing . . . 23
2.3.1 I-Q Imbalance Compensation . . . 25
2.3.2 Static Equalization . . . 26
2.3.3 Adaptive Equalization . . . 27
2.3.4 Carrier Frequency Offset & Phase Recovery . . . 29
2.4 Sensitivity Assessment of a Coherent Receiver . . . 32
2.4.1 Simulations . . . 32
2.4.2 Experiments . . . 36
2.5 Practical Limits & Technical Challenges for Access Networks . . . 39
2.5.1 Bandwidth Restrictions of the Receiver . . . 40
2.5.2 Phase Noise Tolerances . . . 41
2.5.3 Fiber Non-Linearities Constraints . . . 43
2.6 Summary . . . 44

3 Design of a Spectrally Sliced Coherent Receiver (SSRx) for Access Networks **45**
3.1 Motivations . . . 47
3.2 Theory of Spectrally-Sliced Detection . . . 48
3.3 Receiver Architecture . . . 51
3.3.1 Optical Frequency Comb . . . 51
3.3.2 Array of Coherent Receiver . . . 53

3.3.3 Reconstruction Digital Signal Processing 54
3.4 Numerical Simulation Model 57
3.4.1 Simulation Flow 57
3.4.2 25 Gbaud QPSK performance with the scaling of slicing number 58
3.4.3 Performance of Reconstruction Equalization 59
3.4.4 Bandwidth and Comb Spacing Restrictions 62
3.4.5 Comments on the Complexity of SSRx 63
3.5 50 & 100 Gb/s Coherent Link Experiment Utilizing an SSRx . . 65
3.5.1 Experimental Setup 65
3.5.2 Receiver Performance with Comb Power 67
3.5.3 Estimation of the Free Spectral Range of the LO Comb . 68
3.5.4 Optimization of Reconstruction Equalizer 70
3.6 Performance Assessment of SSRx in PON 71
3.6.1 Addressing Burst-Mode PON Challenges 71
3.6.2 Comparison of SSRx with Coherent PON Candidates . . 75
3.7 Summary 79

4 SSRx with Enabling Photonic Integrated Circuit (PIC) Technologies 80
4.1 Introduction & Motivation 81
4.1.1 Optical Frequency Comb Candidate for Spectral Slicing . 82
4.1.2 Comb De-multiplexer Candidate for Spectral Slicing . . . 84
4.2 Investigation of Comb & De-multiplexer Properties on SSRx Performance 85
4.2.1 Spectral Flatness 88
4.2.2 Optical Linewidth 89
4.2.3 Comb Coherence 90
4.2.4 Comb-Line Suppression Ratio 92
4.3 Gain-Switched Comb with Injection Locking (IL-GS OFC) 93
4.3.1 Key Concept 93
4.3.2 Module Characterization 96
4.3.3 Demonstration of an SSRx Utilizing an IL-GS OFC 98
4.4 Integrated Comb Laser Assembly (iCLA) 103
4.4.1 PIC System Design 103
4.4.2 Module Characterization 104
4.4.3 Demonstration of an SSRx Utilizing an iCLA 106
4.5 Summary 110

5 Conclusion & Future Work 111
5.1 Summary of Research 111
5.2 Outlook & Future Work 112
5.2.1 Spectral Reconstruction based on the Channel Estimation 112
5.2.2 Burst-Mode SSRx 112
5.2.3 Higher Scalability of SSRx, $N=4$ 113
5.2.4 Fully-PIC SSRx Demonstration 114
5.2.5 Spectrally Sliced System, Tx with Rx 114

List of Figures

1.1 Optical fiber communication topology including core, metropolitan, data centre interconnect, and access network. OLT: Optical line terminal, ONU: Optical network unit, 5G: Fifth Generation, LTE: Long-term evolution. 2
1.2 Evolution of PON standardized technology. 3
1.3 Simplified diagram of the building blocks of a fully coherent transceiver 6

2.1 Constellation diagrams showing the bit-rate scaling in various dimensions, including (a) advanced modulation formats by employing more bits in a symbol, and (b) capacity doubling by multiplexing the signal in dual-polarization of the lightwave. . . . 12
2.2 Probability of a symbol error for different QAM 13
2.3 General structure of a multi-format optical coherent transmitter employing amplitude and phase modulations in two polarizations of lightwave. Inset: Illustration of modulated signal on a carrier frequency spectrum. 14
2.4 Configuration of a phase and polarization diversity optical coherent receiver 15
2.6 (a) Example FM-noise spectrum of a semiconductor laser using a delayed self-heterodyne setup. (b) Field spectra of beat tones between two ECLs in an experimental setup where the two ECLs were connected to the coherent receiver inputs and the output waveform was taken within 0.2 ms time window; each spectra plotted here has a span of 2 μs. 22
2.5 Delayed self-heterodyne method to measure the FM-noise of a laser. AOM: Acousto-optic modulator. ESA: Electrical spectrum analyzer. 22
2.7 Digital signal processings flow to compensate for impairments and to recover the data stream. Constellation diagrams of both QPSK and 16QAM modulation signals were taken after the associated DSP blocks to illustrate the data processing. 24
2.8 An example of the I-Q channel imbalance induced due to the path mismatches of the RF cables connecting from an integrated coherent receiver to the oscilloscopes 25
2.9 Basic structure of an FIR filter with a length of *N* taps 26
2.10 Basic structure of 2×2 MIMO adaptive FIR filters. 27
2.11 Block processing of frequency offset estimation technique based on peak power search. 29
2.12 Estimated frequency offset measured from the simulated signal transmission (left axis) and the relative error between the estimation and simulation offset values (right axis). 30
2.13 Block processing of CPR based on feed-forward estimation. $\angle(\cdot)$ represents the phase of complex number. 30

2.14 Simulated Wiener laser phase noise by using system modelling presented in Section 2.4.1 later. The total linewidth of the system was set to 100 kHz as shown in black trace. The estimated phase was generated by using the Viterbi-Viterbi algorithm with different symbols averaging L. 31
2.15 Block diagram of a coherent simulation setup. 32
2.16 (a) BER versus received optical power for QPSK and 16QAM modulation formats on different transmission links with single-polarization, and dual-polarization operation. (b) Sensitivity penalty as a function of the LO power (P_{LO}) in the BtB link for different modulation formats. 34
2.17 (a) Performance of the coherent receiver sensitivity against accumulated CD with varied number of taps of chromatic dispersion equalizer. (b) Dispersion-induced broadening of a Gaussian pulse in a fiber transmission at different fiber lengths. 36
2.18 (a) Experimental setup for optical coherent transmission system of 50 and 100 Gb/s of single- and dual-polarization QPSK respectively. (b) Captured optical spectrum of transmitted signal centered at 1553.1 nm wavelength. (c) Optical spectrum used for comparison between transmitted signal with LO. (d) Recovered constellation of DP-QPSK at -22 dBm receive power. 37
2.19 Experimental results of the ICR sensitivity performance of a single-carrier 25 Gbaud QPSK signals employing single-pol (left) and dual-pol (right) in a back-to-back link. 38
2.20 Experimental results of the ICR sensitivity performance over 40 km G.652 standard optical fiber. 39
2.21 The receiver sensitivity tolerance with varied receiver bandwidths for three different baud rate operation. Insets show the associated spectra of the signal from each operating baud rate. 40
2.22 (a) Sensitivity penalty versus combined linewidths symbol duration products for QPSK and 16QAM modulation formats. (b) Constellation diagram without phase domain equalization using QPSK (top) and 16QAM (bottom) for different combined laser linewidths. 42
2.23 Optical link budget as a function of launch power. 43

3.1 Schematic diagram of a spectrally-sliced optical coherent receiver. The received signal is split by a factor of N via an optical splitter and fed into an array of N-integrated coherent receivers. The multi-optical lines are separated by a wavelength de-multiplexer and act as LO that mixes with a portion of signal frequencies. After sub-signal photodetection and ADC readout inside the ICRs, N-complex signal slices are generated. Following the sub-ADC sampling, the whole signal spectrum can be reconstructed by "stitching" together each sampled slice using DSP; thus recovering the received signal. 46

3.2 (a) Experimental setup of an optical frequency comb based on a single-drive MZM. RF Gen.: RF Source Generator. (b) The experimental setup for comb signal demultiplexing using the wavelength selective switch based on liquid crystal on silicon technology. (c) The optical spectrum of the OFC was captured using an optical spectrum analyzer (OSA) with resolution bandwidth of 20 MHz. The two traces represent two different bias settings of the EO-modulator to generate the frequency comb. (d) The optical spectrum of the comb after demultiplexing. The comb line suppression ratio is measured based on the difference between the peak power of the demultiplexed comb line with the adjacent lines. 52
3.3 Schematic of two DP–I-Q coherent receivers configured in parallel, generating $XI_n(t)$, $XQ_n(t)$, $YI_n(t)$ and $YQ_n(t)$ components to the oscilloscopes. 53
3.4 (a) Block diagram of processing steps performed to calibrate timing delay between receiver channels. (b) Captured experimental waveforms of channel 1 (in-phase tributary) from the two separate coherent receivers. (c) Cross-correlation response of the captured waveforms between coherent receivers in each lane. 54
3.5 (a) Functional blocks in a spectrally sliced receiver DSP. The schematic of reconstruction DSP is based on FIR filters for (b) single-polarization, and (c) dual-polarization modulation. 55
3.6 Block diagram of an SSRx simulation system setup. 57
3.7 Simulated BER versus ROP for 50 Gb/s SP-QPSK and 100 Gb/s DP-QPSK. Solid lines refer to a spectral slicing receiver with different number of slicing operation *N*, and the dashed lines refer to a conventional coherent receiver, ICR. 58
3.8 Visualisation of the stitching process of the frequency-shifted signal sliced on a 25 Gbaud signal. (a) N=2, (b) N=3, (c) N=4, and (d) N=5. 59
3.9 Receiver sensitivity measured as a function of phase variance for SSRx with N=2 scheme. Inset: Optical signal waveforms in the time domain where slice 2 was delayed by 20 ps compared to slice 1. 60
3.10 The performance of BER versus ROP with (a) 0 ps, (b) 50 ps, (c) 100 ps, and (d) 150 ps delay between slice 1 and slice 2. 61
3.11 Receiver sensitivity penalty performance in 25 Gbaud QPSK signal transmission versus the frequency spacing of the comb with varied receiver's bandwidth. 62
3.12 (a) The quantity of component required in the front-end receiver. (b) Receiver front-end bandwidth requirement. 64

3.13 (a) Experimental setup for proof-of-concept of 25 Gbaud signal transmission. Spectrally-sliced coherent receiver diagram with two slicing operations (N=2) on two different modulation schemes: SP-QPSK and DP-QPSK. The spectra in (b) illustrate the comb tones aligned to the signal spectrum, subsequently reduced into two smaller spectra, each known as a 'slice', shown in (c). 66
3.14 (a) Experimental results of BER performance versus ROP for the different optical power per comb line. (a) 50 Gb/s SP-QPSK comparing the SSRx performance over BtB and 40 km fiber link. (b) 100 Gb/s DP-QPSK over 40 km fiber comparing the ICR with SSRx detection scheme. 68
3.15 (a) Receiver sensitivity measured as a function of frequency shift for signal reconstruction. (b) Illustration of the impacts of frequency shift on the reconstructed spectra. 69
3.16 (a) Setup for measuring the free spectral range of the comb. (b) The spectra of the beating tone captured by an ESA operating at the resolution bandwidth of 3 Hz. 70
3.17 Receiver sensitivity penalty as a function of the number of taps required for the reconstruction adaptive equalizer in BtB and over 40km fiber link. 71
3.18 Implementation diagram of multipoint-to-point link transmission of PON according to ITU-T standard. 73
3.19 Tolerances to frequency offsets with varied bandwidth of the receiver. 73
3.20 (a) Illustrative signal frame design operating in burst mode. EOB: End of burst. (b) Error convergence versus the symbol length in the equalization training in SSRx (N=2). (c) BER performance of 100 Gb/s DP-QPSK using the SSRx scheme versus the preamble length at a received power of -29 dBm. 74
3.21 Sensitivity for 200 Gb/s DP-16QAM employing SSRx (N=2) over 40 km. 77

4.1 Free spectral range requirement of a comb source in spectral slicing. 83
4.2 Measured intensity transfer function of bandpass filters generated from WSS. The filter bandwidth was configured at the narrowest setting, which was measured to be around 10 GHz. 84
4.3 (a) Simulation system model of optical frequency comb signal generation (brown blocks) and comb de-multiplexing for a spectrally-sliced coherent system using N=2 slices. Schematic comb spectra at various points in the simulation illustrating key parameters for consideration: (b) comb linewidth; (c) phase coherence of comb line; (d) comb line side-mode suppression ratio (CLSR) after de-multiplexing; (e) comb amplitude flatness. 86
4.4 Simulated receiver sensitivity penalty as a function of local oscillator power. The red curve indicates the relative sensitivity penalty between the ICR and SSRx detection schemes. 88

4.5 Simulated sensitivity penalty versus the spectral flatness generated by comb source relative to the spectral flatness of 0 dB. . . 89
4.6 Simulated sensitivity penalty as a function of the product of the laser linewidth Δv and symbol duration $1/B_d$ for two different modulation formats. 90
4.7 (a) Phase noise traces of comb line (Δv=100 kHz) with delayed versions of itself. (b) Simulated sensitivity penalty versus applied time delay for three different linewidth. 91
4.8 (a) Spectra were captured for the whole frequency comb (blue) and two isolated combs filtered by de-multiplexer with finite bandwidth (red and green traces). (b) Simulated sensitivity penalty versus CLSR for SSRx detection. 93
4.9 (a) Schematic diagram of an injection-locking gain-switched frequency comb. (b) Optical spectrum captured with 20 MHz spectral resolution of: (Left) Comb signal from gain-switched DFB laser and tunable ECL laser. (Right) Injection locking with gain-switched comb signal. 94
4.10 Top: The pulse sampling of the optical frequency comb in the time-domain, bottom: Optical spectrum captured with the spectral resolution of 20 MHz for different gain-switching configurations. (a) DFB laser driven at 12.5 GHz sinusoidal RF signal with +5 dBm amplitude, (b) DFB laser driven by +20 dBm RF signal, and (c) DFB laser driven at +20 dBm RF signal with applied injection locking from an ECL laser. 95
4.11 (a) Schematic diagram of an injection-locking gain-switched Fabry–Pérot (FP) laser-based frequency comb. (b) The output optical spectrum of the comb source with 12.5 GHz frequency spacing. 96
4.12 (a) Calculated FM-noise spectrums for both EO-OFC tones and for IL-GS OFC (all five main tones). (b) RF beat tones generated between the pair of comb lines for all four IL-GS OFC pairs captured at 12.5 GHz offset frequency. 97
4.13 (a) Experimental setup for 50 Gb/s SP-QPSK with (N=2) SSRx over 40 km of SMF. The GS-OFC used in this experiment is based on Pilot Photonics LYRA-OCS-1000, while the Finisar Waveshaper (WSS) is used as the comb de-multiplexer. 98
4.14 (a) Receiver power sensitivity performance of the conventional and proposed SSRx for 25 Gbaud QPSK signals. (b) Digitized and frequency-shifted by $\pm$ 6.25 GHz spectral slices (red, blue) and synthesized 25 Gbaud data signal (green) spectra. 100
4.15 (a) Measured receiver sensitivity performance of the SSRx obtained with the IL-GS OFC. The red marker (right y-axis) represents the measured receiver sensitivity of the SSRx for four sets of comb pairs, while the CLSR measured for the demultiplexed comb tones in each pair is represented by the blue and green markers (left y-axis). (b) Sensitivity penalty measured versus CLSR of SSRx obtained with EO-OFC. 101

4.16 The schematic and fabricated PIC layout of both comb source and de-multiplexer respectively. 103
4.17 (a) Phase noise measurements comparing the comb signal with the primary laser, (b) optical spectrum of the output comb signals with frequency spacing of 12.8 GHz and each having CLSR of more than 30 dB, (c) resultant beating tone between the two output tones generated at a frequency of 12.8 GHz. 105
4.18 (a) Experimental setup for 100 Gb/s DP-QPSK with (N=2) SSRx utilizing iCLA. (b) optical spectrum of the transmitted 100 Gb/s signal with two demultiplexed comb lines which each directly mixing with portion spectrum of the received signal. 106
4.19 (a) 100 Gb/s DP-QPSK BER versus ROP performance over 40 km transmission distance. (b) Constellation diagram of SSRx captured at receive power of -20 dBm. 108

5.1 Schematic of an integrated spectrally sliced coherent receiver (N=4) envisioned for PON upstream transmission. 113
5.2 Proposed schematic design of a photonic integrated spectrally sliced coherent transmitter (N=4). SiP: silicon photonic; SOA: semiconductor optical amplifier. 115

List of Tables

2.1 Simulation parameters 33

3.1 Simulation of SSRx system parameters 58
3.2 Polarization and phase diversity coherent receivers. AEQ: Adaptive Equalization. CFO: Carrier Frequency Offset estimation. CPR: Carrier Phase Recovery. 76
3.3 Comparison of component requirements of the front-end receivers. The number in the bracket indicates bandwidth requirement for 200 Gb/s. 77

4.1 Comb generation techniques comparison 82
4.2 Simulation parameters 87

I, Muhammad Hilmi Othman, certify that this thesis is my own work and has not been submitted for another degree at University College Cork or elsewhere. All external references and sources are clearly acknowledged and identified within the contents. I have read and understood the regulations of University College Cork concerning plagiarism and intellectual property.

Muhammad Hilmi Othman

Acknowledgements

I would like to express my highest gratitude to a few people who have made this PhD journey an enriching and rewarding experience.

First and foremost, I would like to express my highest appreciation to my main supervisor, Professor Paul Townsend who has been extremely supportive throughout my entire time spent in Tyndall National Institute. He was there during the difficult times to advise me not only on professional matters, but also, on occasions, personal matters. I also would like to express my gratitude to my co-supervisor, Dr. Cleitus Antony and Dr. Xing Ouyang who has been kind enough to provide the necessary support and guidance. Without either, my PhD would have been very difficult to accomplish.

For enabling me to come to Tyndall National Institute and start my PhD, I would like to thank my sponsors, Science Foundation Ireland for providing me with research fund to support my research. I take this opportunity to recognize the invaluable industrial contribution to my research works especially those from Pilot Photonics, in particular, Dr. Frank Smyth and Dr. Gaurav Jain who developed comb laser module that were used for my experimental testbed.

I would also like to thank my fellow colleagues who have made my day-to-day work a very interesting and enjoyable experience, particularly to Stephen, Conor, Shivangi, Julie, Yeasir, and the rest of the members of Photonics System Group. Xing was the first person to greet me when I arrived at Tyndall and has since provided me with insightful advices throughout my research. Stephen was always there every morning asking me about my well-being and has been supportive in research study related matters. Without these people, my days in the lab would not have been such an enjoyable experience as it was.

Personally, I would like to thank my beloved wife, Aishah for her endless love and support for the last five years particularly during the difficult times of my PhD. Special thank you to my pillars of life, my family for always supporting me and praying for my success. Finally, I would like to thank the whole Malaysian community in Cork in general for supporting me with good food, fun activities, and good companionship from the day I arrived to the day I submitted this thesis.

Abstract

The recent popularity of bandwidth-intensive applications, such as high-definition video streaming, virtual reality, and augmented reality generative platforms, has resulted in a huge demand for higher data transmission speeds over the telecommunication network based on optical fiber. As the line rates of the access network move toward 100 Gbit/s and beyond, legacy intensity modulation with direct detection will struggle to continue to support high-link power budgets and distances. Meanwhile, digital coherent optics opens up clear improvements for the next-generation access network and easily meets the high-speed, power budget, and distance requirements. However, significant challenges must be addressed to make such technology suitable for the cost-sensitive access network, such as redesigning and minimizing the cost of the technology. In particular, the complexity of the coherent transceiver design is compounded by the need for expensive broad-analog-bandwidth components, which is an obstacle to the deployment of high-bitrate coherent technology for the next-generation access network.

This could be potentially addressed with the optical spectral slicing technique, which would allow the utilization of high-volume and low-cost commodity receiver components. Hence, this dissertation focuses on the development of a spectrally sliced coherent receiver, which enables the parallel coherent detection of a wideband optical waveform in the frequency domain. By harnessing the low-cost manufacturing potential of maturing photonic integration technologies such as silicon photonics and micro-transfer printing, together with the bandwidth reduction capability of spectral slicing, new opportunities for the application of coherent communication technology in future access network systems may be realized.

The objectives of this dissertation encompass the investigation and validation of spectrally sliced detection design, and receiver performance in the context of an optical access network. This work successfully demonstrates a spectrally sliced receiver with high optical receiving sensitivity operating over 40 km of optical fiber employing 100 Gb/s dual-polarization modulation. In addition, the author has demonstrated that the bandwidth requirements in the optical receiver component can be significantly reduced by a factor corresponding to the number of slices implemented. Overall, the technical contribution presented in this dissertation provides a series of analytical and experimental research studies on parameter requirements of the optical frequency comb as well as the recon-

struction signal processing; which are the two main components in the proposed receiver design. However, since the receiver must address the challenge of scaling economics in the access network, the digital, electrical, and optical complexity must be minimized. To this end, the author has incorporated a monolithically integrated comb source and an active demultiplexer with the proposed detection scheme, which leverages the great potential of the photonic integrated circuit to reduce the size and cost. These are pragmatic and important steps to pave the route towards a low-cost, fully integrated spectrally sliced system. To the best the author knowledge, the works presented here represent the first spectral-slicing demonstrations in the context of access network. Finally, the author discusses some of the prospective research directions and the interesting challenges that arise for the proposed receiver that can be implemented in future access network applications.

Symbols & Abbreviations

Physics Constants

c	Speed of light in a vacuum	$299\,792\,458\,\mathrm{m\,s^{-1}}$
k_B	Boltzmann constant	$1.380649\times10^{-23}\ \mathrm{J\,K^{-1}}$

Abbreviation

ADC	analog-to-digital converter
AEQ	adaptive equalization
AWG	arbitrary waveform generator
BER	bit error rate
BPD	balanced photodiode
BPF	band pass filter
BPSK	binary phase-shift keying
BtB	back-to-back
CD	chromatic dispersion
CLSR	comb line suppression ratio
CPR	carrier phase recovery
DAC	digital-to-analog converter
DCI	data center interconnect
DD	direct detection
DP	dual polarization
DSCM	digital subcarrier multiplexing

DSP	digital signal processing
ECL	external cavity laser
EDFA	Erbium-doped fiber amplifier
EO	electro-optic
ESA	electrical spectrum analyzer
FEC	forward error correction
FSR	free spectral range
FTTH	fiber-to-the-home
GS	gain-switched
I/Q	in-phase and quadrature
iCLA	integrated comb laser assembly
ICR	integrated coherent receiver
IL-GS	injection locking gain-switched
IM	intensity modulation
ITU	International Telecommunication Union
LO	local oscillator
MIMO	multi-input–multi-output
MLL	mode-locked laser
MZM	Mach–Zehnder modulator
NRZ	non-return zero
OFC	optical frequency comb
OIF	Optical Networking Forum
OLT	optical line terminal
ONU	optical network unit
OSA	optical spectrum analyzer
P2MP	point-to-multipoint
P2P	point-to-point

PBC	polarization beam combiner
PBS	polarization beam splitter
PC	polarization controller
PD	photodiode
PIC	photonics integrated circuit
PMD	polarization mode dispersion
PON	passive optical network
PSK	phase-shift keying
QAM	quadrature amplitude modulation
QPSK	quadrature phase-shift keying
ROP	received optical power
RTO	real time oscilloscope
SMF	single mode fiber
SNR	signal-to-noise ratio
SOP	state of polarization
SP	single polarization
SSRx	spectrally-sliced receiver
TIA	transimpedance amplifier
VOA	variable optical attenuator
WSS	wavelength selective switch

Units

b/s	bit per second
$baud$	symbol per second
dB	decible
dBm	decibel milliwatt
Hz	hertz

Chapter 1

Introduction

Chapter 1 describes the evolution of optical communication networks, in particular the application of the optical access network, as well as the growth of access capacity today. Then, the potential of coherent optics for next-generation access networks is examined, concurrently addressing its main challenges and several driving technologies that can be facilitated for future access deployment. Finally, the outline of the remaining chapters in this thesis is presented.

Communication technology has a profound impact on today's society. The 2020 pandemic has emphasized how important internet broadband is to daily life for everyone, and since then it has been estimated that people have created, stored, and shared 1.7 MB of data every second [1]. Recent advances in generative artificial intelligence and machine learning, such as the highly publicized and debated ChatGPT, is driving investment in data centers to address huge data demands in optical interconnects. It is expected that more than 200 Zettabytes will be housed in cloud storage worldwide [2]. In Europe, this similar upward trend is observed, with fiber broadband networks now reaching 57% of households [3]. These huge volumes of data are not only growing continuously, but are also becoming more and more accessible, helping people to interact, educate, entertain and connect around the world.

For the last four decades, this ever-increasing demand for information has always been enabled by the development of new optical telecommunication technology such as the introduction of optical fiber, optical amplifier, wavelength-division multiplexing, coherent detection, and more recently digital signal processing. This has driven the International Telecommunication Union - Telecommunica-

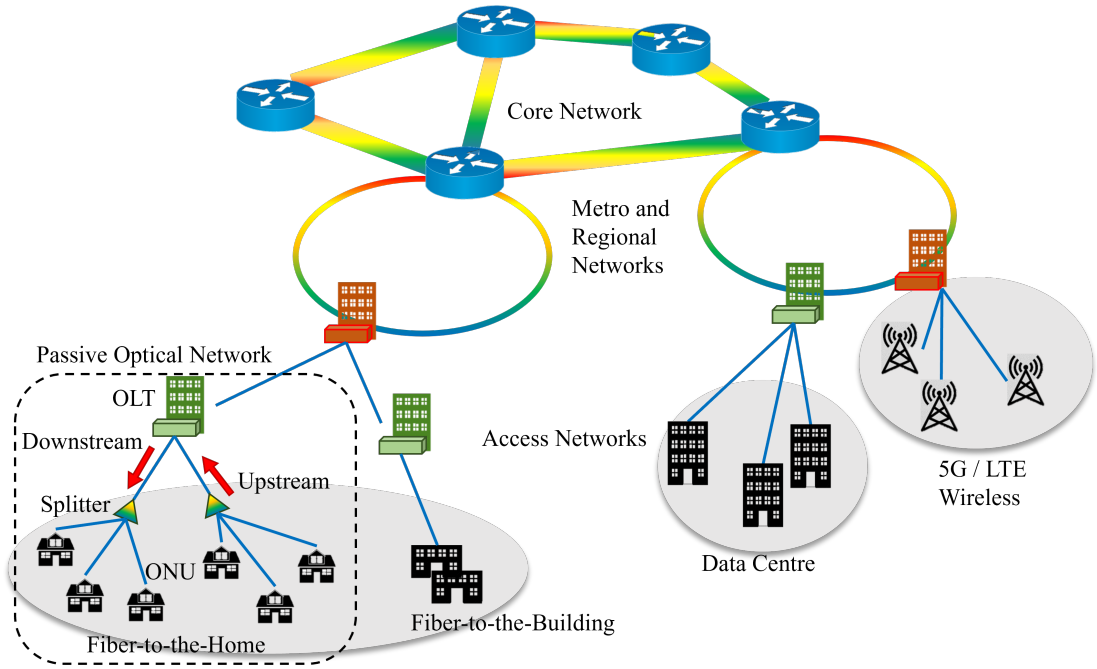


Figure 1.1: Optical fiber communication topology including core, metropolitan, data centre interconnect, and access network. OLT: Optical line terminal, ONU: Optical network unit, 5G: Fifth Generation, LTE: Long-term evolution.

tion Standardization Sector (ITU-T) to work together with network operators to design and develop optical fiber communication networks, which form the backbone of today's telecommunication system to meet user Internet demands. As illustrated in Figure 1.1, this network has been designed in a hierarchical structure; the core network that provides ultra-large capacity (>100 Gb/s per wavelength and many tens of wavelengths per fibre) over long-haul transmission (hundreds and thousands of kilometers) between countries or continents via terrestrial or submarine fibers, the metropolitan network that connects between cities (tens to hundreds of kilometers), and finally the access network that provides the Internet service connectivity to a large number of customers via Fiber-To-The-Home (FTTH), for example [4].

Access network connections can be wired or wireless, and a passive optical network (PON) is part of this wired connectivity that has replaced traditional copper networks to carry high-speed data, video, and voice services directly to subscribers. The PON network configuration has a point-to-multipoint (P2MP) topology with an optical line terminal (OLT) acting as a gateway in a central office for up to 64 subscribers, all connected via a single trunk fiber using passive optical splitters. Network capacity is shared amongst optical network units (ONUs) through time division multiplexing, with wavelength division multiplexing an

option for capacity enhancement. There are no active components installed between the OLT and the ONU (thus, a 'passive' optical network), therefore reducing operating costs, with the majority of investments involved in the initial fiber installation [5]. PON has become a dominant technology in the optical access market due to its relatively low cost and sustainability for mass deployment. This presents significant advantages for the telecommunications sector and comes on the back of a massive investment cycle. However, as network providers and operators will be all too aware, the quality of networks is as crucial as the cost [6]. Operators are working hard to ensure that their network systems are capable of delivering high capacity demands to customers, with the added goal of reducing the cost per bit, footprint, and power consumption.

1.1 Evolution of Passive Optical Network

The technological trend of PON technology can be illustrated in Figure 1.2, which is standardized by ITU-T and the Institute of Electrical and Electronics Engineers (IEEE) [7]. Since the advent of Gigabit PON (GPON), the PON standard has progressed towards a higher data rate scale by approximately an order of magnitude every decade. In recent years, Ireland has reported the implementation of the XGS-PON system to provide 10 Gb/s symmetric capacity of broadband services to homes and businesses across the country [8]. These PON standards implement intensity modulation with direct detection technology (IM/DD), due to its sim-

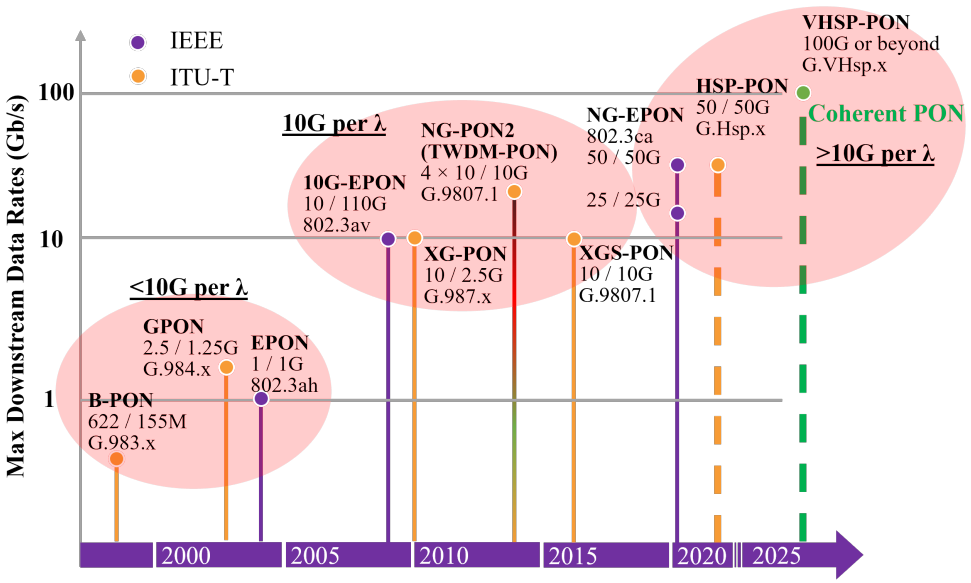


Figure 1.2: Evolution of PON standardized technology.

plicity and cost-effectiveness. In September 2021, ITU-T published its latest PON recommendations, which outlined the requirements for the next generation 50 Gb/s high-speed (HS) PON [9]. For the first time, a PON standard is tentatively set to embrace digital signal processing (DSP) technology for upstream transmission, and DSP is expected to play an important role in enabling next-generation PON that supports 50 Gbit/s and beyond. Then, through the judicious use of DSP, to compensate for impairments that arise from performance deficiencies in the enabling components. For example, the 50G standard envisages the use of 25G-class optoelectronics and employs digital equalizers to compensate for bandwidth limitations that would otherwise occur in a 50G non-return-to-zero (NRZ) modulation context.

Due to the difficulty in addressing the large ($\sim$30 dB) power budget requirement in P2MP PONs, especially at higher speeds, the 50G standard may be the last to use conventional IM/DD [10]. This raises the question of whether coherent detection, with its higher receiver sensitivity and ability to fully compensate for the effects of large fiber dispersion in the digital domain, may be required for future 100G PON and beyond. Following the progression of PON technology, a new standardization work on the Very High Speed (VHSP) PON [11] has begun to aim at line rate operation above 50 Gb/s. The recent literature and discussion that are currently ongoing for ITU-T G.suppl.VHSP are proposing the use of coherent technology in PON for higher bit rates on a single wavelength and long-reach of fiber link [12, 13].

1.2 Evolution of Coherent Optics

Since 2008, DSP has begun to be introduced into coherent optics technology to exploit the amplitude, phase, and polarization of light waves to carry information at high speed, 40 Gb/s data rates and beyond per wavelength [14]. Furthermore, it allows the processing of complex signals, compensating for various impairments that occur during signal propagation, to achieve a longer fiber transmission distance (>20 km) [15]. This emergence led to the first commercialization in 2010 in the form of 5"$\times$7" Optical Networking Forum (OIF) compliant Multi-Source Agreement (MSA) modules and was designed using the best-in-class discrete optical and electrical components that supported 100 Gb/s transmission across the 2000 km fiber distance [16]. Since then, it has been deployed in most parts of core networks, and the last decade has seen investments and continued innovation drive advances in pursuit of efficiency, speeds, and cost-per-bit reduction

for digital coherent optics technology.

The next generation of coherent optics in the core network is taking the form of 1.2 Tb/s rate capabilities, which allows the operator to double the network capacity compared to previous deployments while reducing power consumption and equipment footprint by up to 50% [17]. Following successful deployments in the core network, coherent DSPs have opened the door to their application in metro and data center interconnect (DCI) networks. With the addition of flexibility in the C-band wavelength, transmission reachability, and further reduction in footprint to pluggable quad small form factor, the OIF 400ZR transceiver module has advanced as an enabling step toward the next-generation DCI system [18].

The next progression for coherent technology is likely to be in the context of the future PON system [19]. A similar migration pattern has been seen before in the optical network industry. The wavelength division multiplexing system and forward error correction technologies were started in the core network before being migrated to metro and edge access. However, simply migrating the relatively expensive existing coherent optics from long-haul and metro is not a practical proposition, since cost is a critical aspect in access networks. The next section will discuss potential approaches to redesign and reengineer conventional digital coherent optics, leveraging further reductions in complexity and cost.

1.3 Digital Coherent Drivers for Access Network

For the past few years, coherent PON has been the subject of much research attention as a potential future PON technology [20, 21], and both academia and industry are actively exploring enabling technologies, such as novel system structures with an O-band($\sim$1300 nm) optical wavelength window, reduced complexity DSP, new materials, simplified devices, and network architectures, to address this digital coherent optics in PON. As mentioned in the previous section on access network upgrade criteria, a critical consideration to be highlighted is the cost [22]. In other words; what else could be done to further cost-reduce the coherent technology towards the cost points required for PON?

One of the emerging research directions was to exploit the simplification of the optical coherent receiver architecture by reducing the number of components required. Recent demonstrations of 100G coherent PON using the minimal coherent receiver based on a single polarization heterodyne receiver circuit have been carried out over 25 km of fiber [23]; also showing that the number of components

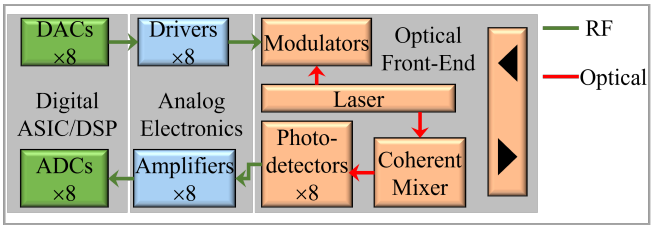


Figure 1.3: Simplified diagram of the building blocks of a fully coherent transceiver

required in a receiver, such as photodiode, transimpedance amplifier (TIA), and analog-to-digital converter (ADC), can be reduced compared to a fully coherent receiver (as depicted in Figure 1.3), thus simplifying the complexity of the receiver design. Similar approaches have been shown by using heterodyne coherent detection; which not only can halve the number of components required, but also replaces the optical hybrid with an inexpensive 3dB coupler [24]. Although most of the mentioned works have proven the simplification concept compared to the state-of-the-art coherent receiver, there are major drawbacks associated. In some cases, the receiver sensitivity performance of these simplified receivers is reduced by at least 3 dB compared to a conventional coherent receiver [19], and the simplified receiver configuration comes at the expense of higher bandwidth requirements in the component, which is a major obstacle in an integrated platform.

To reduce the cost and footprint of a coherent system even further and facilitate the deployment in an optical network, significant efforts have been made to integrate optical and electronic components into a single chip known as a photonic integrated circuit (PIC). PICs have played a key role in enabling the transition of coherent technology from long-haul to lower-cost applications, such as short-reach DCI, through new "stripped down" coherent approaches, as exemplified by the 400G ZR standard [18]. Another perfect example, a transceiver product that is compliant with IEEE 802.3^{TM}, the first coherent transceiver available in a standard QSFP28 form factor that uses PICs based on indium phosphide (InP) and silicon photonics (SiPh) that allows wafer-level integration of a variety of active and passive components [25, 26]. This has realized 400G data rate transceivers with sufficiently high yields to drive coherent technology pricing down, and hence suitable for commercial products.

Recent innovation for a coherent access network; XR optics was introduced by Infinera and is attracting much interest from network operators [27]. Although the physical architecture of the transceiver remains the same as the conventional design shown in Figure 1.3, the addition of digital subcarrier multiplexing modulation has provided a more flexible approach to data rate provision on a conventional PON P2MP overlay. Consequently, allowing the use of low-speed pluggable optical solutions on a low-speed subcarrier, thus promoting flexibility,

cost, and power-efficient pluggable optical solutions [28]. However, the granularity of bandwidth provision is limited to a single subcarrier, which is large by PON standards given the numbers of subarriers envisioned. In contrast, the historical guiding design principle for PON development to date, has been to use time division multiplexing (TDM downstream) and time division multiple access (TDMA upstream) to allow all users to dynamically access a wide range of bandwidths up to the maximum supported by the PON via the TDM/TDMA network control protocol. This feature has enormous advantages for network operators in terms of mixed service provision and is historically the reason why this has been maintained throughout the standardized PON technology.

Overall, a "simplified" coherent system scheme and the integration capability of PIC technology are emerging areas of research for high-speed, yet low-cost coherent technology. Combining these two aspects allows for the development of a high-performance and highly integrated coherent transceiver in a compact chip, which advances the coherent technology roadmap directed toward future PON.

1.4 Objectives

The primary motivation and novelty presented throughout this thesis was to propose, develop, and explore some of the key practical considerations for future access networks, focusing mainly on whether the proposed work; a spectrally sliced coherent receiver (SSRx) could play a role in coherent technology that promotes a cost-effective solution. To achieve the given objective, the following methodologies are used:

- To design a spectrally sliced receiver and a novel DSP algorithm to enable spectral reconstruction.

The proposed receiver architecture should be based on the conventional optical coherent receiver architecture and be able to slice a single-carrier coherent optical waveform. The reconstruction algorithm should be able to synthesize baseband slices and recover the signal within the DSP implementation capabilities, and it should be simple and efficient. To prove this concept, the proposed receiver should be demonstrated on a PON transmission link (downstream) at a speed rate envisioned for coherent technology and modulation format.

- Investigate enabling technologies to implement spectrally sliced receivers efficiently for cost-effective solutions.

PIC technology has already proved to be essential for reducing the cost of conventional coherent receivers, and this will also be the case for receiver development for future coherent PON applications, where new PIC innovations will be required. For example, as will be shown, a novel aspect of the spectral slicing approach explored in this work, is that the receiver PIC would need to incorporate an integrated optical frequency comb source and associated wavelength demultiplexer. Therefore, a central aspect of the research is to explore the attributes of the photonic devices in the receiver for efficient spectral slicing and reconstruction of the wideband signal. By focusing on this aspect, the author has shown component developers what types of specifications are required and how potential design trade-offs in the device may affect the transmission system performance.

1.5 Thesis overview

The rest of the thesis is organized as follows:

Chapter 2. Coherent systems for optical communication
This chapter is divided into two main parts.

The first part reviews conventional technologies in digital coherent optics, which are believed to be promising solutions toward a high-speed future PON. Fundamental impairments that affect the systems' performance, such as chromatic dispersion and phase noise, have been taken into account, and the associated DSP (on the receiver side) has been explored to compensate for fiber transmission impairments.

In the second part, the author has experimentally verified such system performance at 50 Gb/s and 100 Gb/s data rates using single- and dual-polarization QPSK modulation formats, respectively. Additional analyses on bandwidth limitations, impairment tolerance, and DSP optimization were performed to meet the required performance in a PON link transmission. The results measured here are necessary as a performance benchmark for the spectrally-sliced receiver scheme proposed in the following chapters.

Chapter 3. Design of a Spectrally Sliced Coherent Receiver
Chapter 3 presents the concept of a coherent receiver based on the spectral slicing technique, which is proposed throughout this dissertation as a potentially cost-effective solution for coherent PON applications. The following section presents a detailed theoretical and mathematical description of spectral slicing and reconstruction operations. The crucial building blocks to enable such a technique, an array of coherent receivers, optical frequency comb, and reconstruction digital signal processing, are elaborated. Simulations and experiments were carried out to test the feasibility of the proposed receiver, and the performance was compared and analyzed with a conventional receiver. Further investigations of different system parameters, such as fiber length, receiver sensitivity, post-processing configurations, and scalability, were carried out to understand the behavior of the system.

Chapter 4. Spectrally Sliced Receiver with Enabling PIC Technologies
The chapter examines the importance of PIC technology in the development of the proposed SSRx scheme for the coherent PON application, in particular in the context of the optical frequency comb; which must be amenable to low-cost photonic integration in a transceiver and need only have a modest number of lines. The impacts of these frequency-comb properties on the spectral slicing scheme with observations on the receiver sensitivity performance were investigated. Following the comb and the de-multiplexer's parameters investigation, the author has demonstrated the proposed receiver by utilizing a photonic integrated frequency comb source and integrated comb laser assemblies. These studies and demonstrations have resulted in high-impact publications and collaborations with the Irish photonics company, Pilot Photonics.

Chapter 5. Conclusion and Future Work
This chapter summarizes the achievements of the work and discusses related prospective future research directions.

Chapter 2

Coherent systems for optical communication

This chapter introduces the basic concepts of digital coherent optics needed to understand the work and the results presented in subsequent chapters. In particular, the modern coherent transmitter and receiver typically used in optical communication systems, major impairments that impair the transmitted signal in the fiber link, and the associated DSP to recover the data are presented. The capabilities of a coherent receiver were evaluated taking into account various aspects of the system, such as noise and sensitivity limitations, front-end bandwidth requirements, fiber distances, phase noise tolerance, and post-processing configurations.

2.1 Theory & Operation of Digital Coherent Optics

Digital coherent detection has enabled optical communication to fully leverage the benefits of advanced modulation formats that exploit the optical carrier's multiple dimensions (phase, amplitude and polarization) to convey information. Any kind of multi-level modulation format can be detected using the coherent receiver. Although the spectral efficiency of binary modulation formats is limited to 1 bit/s/Hz/polarization, modulation formats with k bits of information per symbol (where $k>1$) can achieve up to the spectral efficiency of k bit/s/Hz/polarization. In this section, some of the advanced modulation formats of practical interest enabled by optical-coherent technology are discussed.

2.1.1 Digital Modulation

Digital modulation is the mapping of information bits (typically represented as a binary sequence) to a set of symbols that dictate the property of the signal. Every symbol can be described by the position in the constellation diagram, which is represented as the amplitude and phase of the signals. These dimensions can be utilized for modulation in fiber-optic communication to carry the data. Here, the number of bits k can be assigned to each symbol S as follows:

$$S = \{s_m\}_{m=1}^{M}, M = 2^k. \tag{2.1}$$

By encoding more amplitude/phase changes in the carrier, it is possible to increase the number of bits carried in each symbol. An example of signal constellations is shown in Figure 2.1(a) for multilevel modulation formats. Note that the I and Q abbreviations refer to "in-phase" and "quadrature", respectively, representing a complex message signal that allows simultaneous change of both amplitude and phase. In addition, an optical fiber can be regarded as a circular waveguide and, as such, supports two orthogonal polarization signals, which can also be used to carry data. By selectively transmitting modulated signals using polarization multiplexed carriers, the spectral efficiency of a given modulation technique can be effectively doubled by exploiting a polarization diversity receiver. Therefore, compared to single-polarization (SP) signals, dual-polarization (DP) schemes such as DP-QPSK, DP-16QAM, and DP-64QAM offer doubling the data rate. In this case, a symbol is a combination of amplitude and phase and occupies two polarization states (X and Y polarizations), as illustrated in Figure 2.1(b).

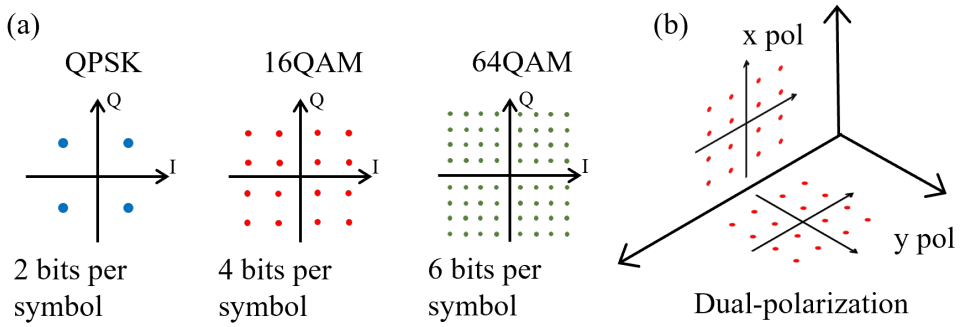


Figure 2.1: Constellation diagrams showing the bit-rate scaling in various dimensions, including (a) advanced modulation formats by employing more bits in a symbol, and (b) capacity doubling by multiplexing the signal in dual-polarization of the lightwave.

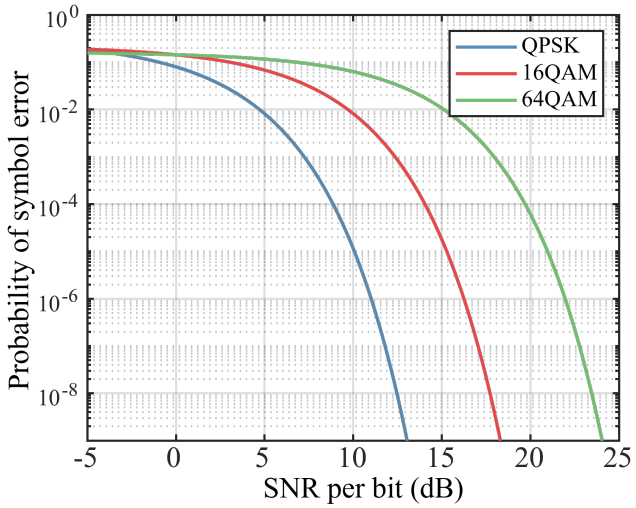


Figure 2.2: Probability of a symbol error for different QAM

Figure 2.2 shows the theoretical signal recovery performance for different QAM modulation formats. Note that the QPSK modulation format is identical to 4QAM. Using the expression for the probability of error in QAM signaling [29], the required signal-to-noise ratio (SNR) per bit is plotted as a function of the probability of an error in the received signal. For a higher-order modulation format, the SNR required to achieve the same symbol error probability is increased as the minimum Euclidean distance between signal constellation points is reduced. Hence, if a given SNR is guaranteed in a communication system, this provides insight to the system designer on how to maximize capacity through the optimum choice of modulation format.

In the following sections, the author discusses the state-of-the-art of a multiformat optical transmitter and coherent receiver that are commonly deployed for current coherent systems in the telecommunication network system. Note that the configuration and common features of the following modules are compliant with OIF standards [30, 31].

2.1.2 Optical Coherent Transmitter

Fig. 2.3)(a) depicts a dual-polarization I-Q transmitter that would be required to generate a multi-format optical signal, for instance, a single carrier of 100 Gb/s DP-QPSK [30]. The fundamental components in this transmitter system incorporate a laser, both polarization beam splitter (PBS) and combiner (PBC), and two I-Q optical modulators; which consist of two-nested structures of the Mach-Zehnder modulator (MZM). First, the continuous-wave (CW) light gener-

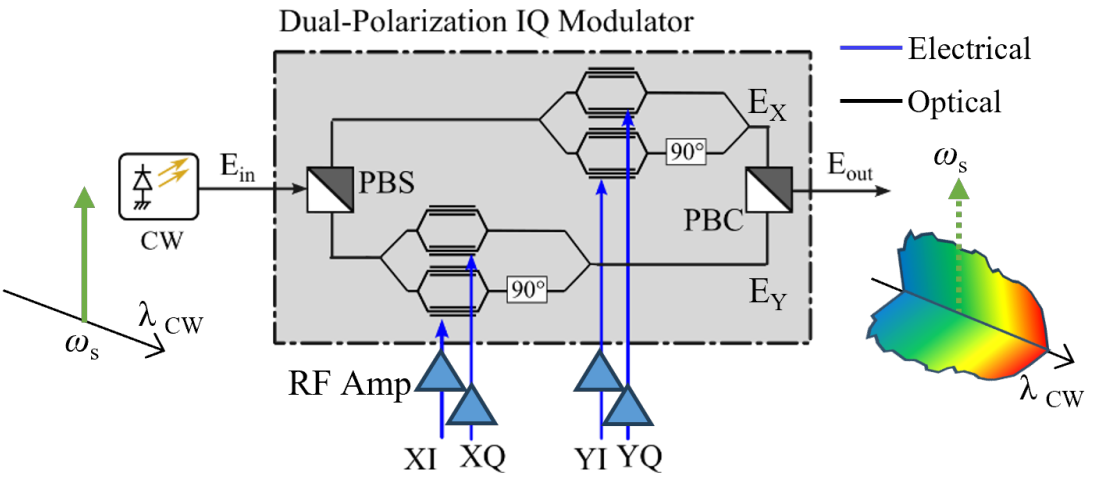


Figure 2.3: General structure of a multi-format optical coherent transmitter employing amplitude and phase modulations in two polarizations of lightwave. Inset: Illustration of modulated signal on a carrier frequency spectrum.

ated from the laser is split into two orthogonal linear polarizations through a PBS. Then, it is further split and fed into two arms of nested MZMs (I-Q modulator), which generate in-phase and quadrature tributaries to form a complex signal. The light is then modulated by the amplified electrical signals generated by a pair of digital-to-analog converters (DACs) for optical signal generation. Following Equation 2.1, electrical waveforms can be mathematically represented in the time domain as:

$$\begin{aligned} u(t) &= s_k(t) * g(t), \\ &= \sum_n s_k(n) \cdot g\left(t - nT_s\right), \end{aligned} \tag{2.2}$$

where the function $g(t)$ represents the baseband waveform and $s(n)$ is the train of the symbol signal. After that, the two modulated optical signal is routed into a PBC so that the signal from the upper half of the circuit (X-polarized) is combined and orthogonal to the lower half of the circuit (Y-polarized). The inset image (right side) in Figure 2.3 illustrates a modulated optical spectrum of the dual-polarization signal centered at the wavelength of the carrier laser. The spectrum of the modulated signal is confined or shaped into a single spectrum where the width is determined by the temporal characteristics of the symbol signal. Assuming the laser used for modulation has an angular frequency of ω_s, the output signal E_{out} generated from the optical transmitter can be expressed as:

$$E_{out}(t) = \begin{bmatrix} E_X \\ E_Y \end{bmatrix} = A_s \begin{bmatrix} u_X(t) \\ u_Y(t) \end{bmatrix} exp(j\omega_s t). \tag{2.3}$$

2.1.3 Optical Coherent Receiver

Figure 2.4 shows the configuration of a polarization and phase diversity optical coherent receiver [31]. First, the input optical signal is split into two orthogonal linearly polarized components via a PBS; each aligns with a copy of a linearly polarized local oscillator (LO) before being routed into a 90° optical hybrid. The optical hybrid consists of a two-by-two optical coupler with 90° phase delay implemented at one arm of the coupler. This circuit allows for the extraction of the I- and Q components of the signal resulting from the mixing product between the received signal and the LO. The phase extraction process enabled by the LO laser is the essence of coherent detection.

Assuming that the incoming signal from the transmitter is represented by the previous Equation 2.3, the optical field of LO can be described as:

$$E_{LO}(t) = A_{LO}(t) exp\left(j\omega_{LO} t\right), \tag{2.4}$$

where both A_s and A_{LO} represent the complex amplitude of the signal and the

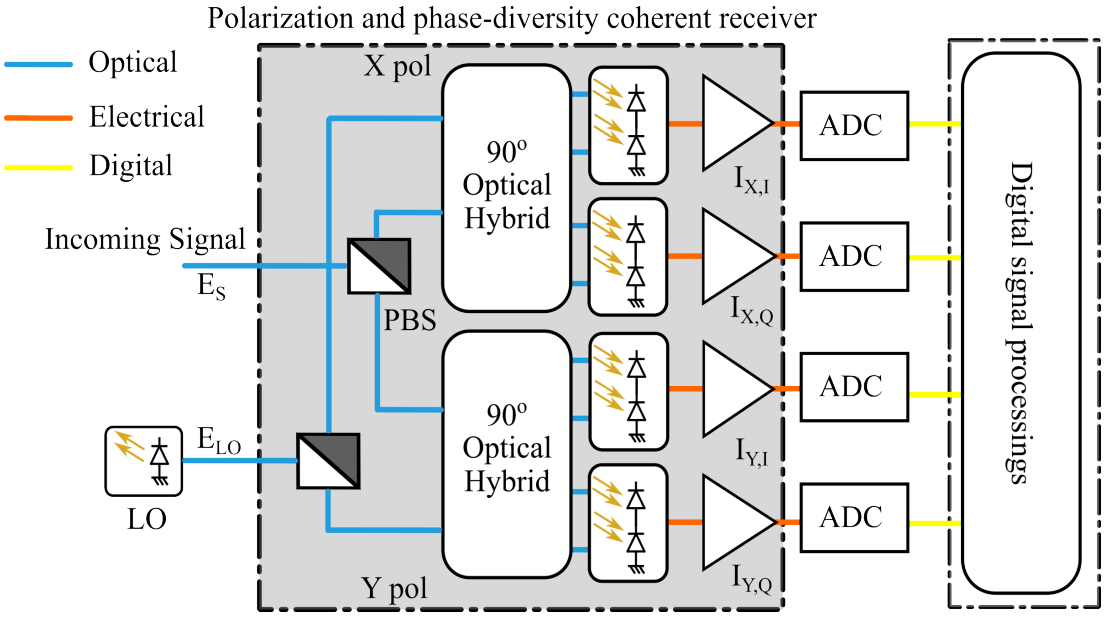


Figure 2.4: Configuration of a phase and polarization diversity optical coherent receiver

LO, respectively; while ω_s and ω_{LO} are the angular frequencies of the signal and LO, respectively. As both signals are mixed in the 90^o optical hybrid; which provides a phase shift of 90^o between the input branches, the output fields of the two 90^o optical hybrids can be represented as:

$$\begin{bmatrix} E_{X1} \\ E_{X2} \\ E_{X3} \\ E_{X4} \end{bmatrix} \propto \begin{bmatrix} E_X \\ E_{LO} \end{bmatrix} + \frac{1}{2} \begin{bmatrix} 1 & 1 \\ 1 & j \\ 1 & -1 \\ 1 & -j \end{bmatrix}, \qquad \begin{bmatrix} E_{Y1} \\ E_{Y2} \\ E_{Y3} \\ E_{Y4} \end{bmatrix} \propto \begin{bmatrix} E_Y \\ E_{LO} \end{bmatrix} + \frac{1}{2} \begin{bmatrix} 1 & 1 \\ 1 & j \\ 1 & -1 \\ 1 & -j \end{bmatrix} \tag{2.5}$$

After that, the signal is converted from the optical domain to the electrical domain by using a series of balanced photodiodes (BPD). The purpose of using balanced photodiodes here is to cancel the signal and local oscillator self-interference terms whilst adding the signal-local oscillator beat terms that contain the phase information, which reduces unwanted relative intensity noise in the digital domain. Assuming both photodiodes are identical in responsivity, R and 50/50 power splitting in the design, the photocurrent from each photodiode can be represented as:

$$\begin{aligned} I_1(t) &= \frac{R}{2}\left\{P_s(t) + P_{LO}(t) + \sqrt{2P_s(t)P_{LO}(t)}\right\}\cos\left[\varphi_{IF}(t)\theta_{tx}(t)\theta_{LO}(t)\right], \\ I_2(t) &= \frac{R}{2}\left\{P_s(t) + P_{LO}(t) - \sqrt{2P_s(t)P_{LO}(t)}\right\}\cos\left[\varphi_{IF}(t)\theta_{tx}(t)\theta_{LO}(t)\right], \end{aligned} \tag{2.6}$$

where both θ_{tx} and θ_{LO} represent the phase noise term of the transmitter laser and the LO, respectively. P_s and P_{LO} refer to the power of the optical field of the signal and the LO, respectively. Note that these terms are related to the complex amplitude A_s and A_{LO}, respectively, as $P_s = |A_s|^2/2$ and $P_{LO} = |A_{LO}|^2/2$. The resultant photocurrent after the two are combined (output of balanced photodiode) can be given by:

$$I_{I,Q}(t) = I_1(t) - I_2(t)$$

$$I_I(t) = 2R\sqrt{P_s P_{LO}}\cos\left[\varphi_{IF}(t)\theta_{tx}(t)\theta_{LO}(t)\right], \tag{2.7}$$

$$I_Q(t) = 2R\sqrt{P_s P_{LO}}\sin\left[\varphi_{IF}(t)\theta_{tx}(t)\theta_{LO}(t)\right],$$

Compared to a single photodiode, the balanced photodiode offers a higher optical power dynamic range and improved noise performance. From these equations, it can be deduced that the underlying concept of coherent detection is the product of the modulated light signal with the continuous-wave LO. The photocurrents generated from the coherent receiver (after balanced photodetection in each polarization channel) can be represented as:

$$\begin{aligned} I_c &= I_I(t) + jI_Q(t), \\ &= 2R\sqrt{P_s P_{LO}}e^{\varphi_{IF}(t)\theta_n(t)}. \end{aligned} \tag{2.8}$$

If the beat frequency, φ_{IF}; defined as the frequency offset between the signal and the LO frequency ($\varphi_{IF} = f_s - f_{LO}$), is larger than the electrical bandwidth of the front-end receiver, then this part of the photocurrent will be rejected through low-pass filtering. Thus, it is crucial to optimize the receiver bandwidth according to the signal bandwidth generated by the transmitter to enable full reception of the signal without filtered loss. Later in this chapter; Section 2.5.1, the author simulates how this requirement will affect transmission performance.

2.2 Noise & Channel Impairments

This section discusses several noise contributions and channel impairments that are specifically relevant in an optical access network application scenario.

2.2.1 Receiver Noises

Considering a non-amplified link such as in a PON, the total noise generated from the receiver is defined as the total sum of thermal noise $\overline{i^2_{Thermal}}$ and shot noise, $\overline{i^2_{shot}}$, which can also be computed as:

$$\overline{\sigma_{Rx}} = \overline{\sigma_{Thermal}} + \overline{\sigma_{shot}};$$

$$\overline{\sigma_{Thermal}} = \frac{4k_BTB}{R_{ext}}, \tag{2.9}$$

$$\overline{\sigma_{shot}} = 2qR\frac{P_{LO} + P_s}{2},$$

where k_B is the Boltzmann constant, T is the temperature, B represents the receiver noise bandwidth, R_{ext} is the external load resistance for double balanced photodiodes and q is the elementary charge. Taking the equation of the photocurrent from Equation 2.8, the SNR of the system can be expressed as:

$$\begin{aligned} SNR &= \frac{\langle I_c \rangle^2}{\overline{\sigma_{Rx}}}, \\ &= \frac{4R^2 P_s P_{LO} e^{\varphi_{IF}(t)\theta_n(t)}}{\frac{4k_BTB}{R_{ext}} + qR\left(P_{LO} + P_s\right)}, \end{aligned} \tag{2.10}$$

From this equation, the scaling of the receiver sensitivity performance is determined by the shot noise, which is investigated in the later Section 2.4.1. By increasing the LO power, the SNR of the system improves as well; however, the shot noise term increases and at some point will limit the SNR scaling.

2.2.2 Optical Fiber Linear & Nonlinear Propagation

Aside from the receiver noise, the quality of the received signal is also impaired by the fiber channel transmission. The G.652 ITU-T standardized single-mode fiber (SMF) is the most widely deployed fiber in optical transmission networks due to its low loss and wide wavelength transparency window, as well as its fabrication process maturity, making the technology suitable for mass production at relatively low cost [32]. SMF typically consists of a 9.2 μm diameter germanium doped silica core, surrounded by a 250 μm diameter undoped cladding layer, with the resulting difference in core-cladding refractive index resulting in the confinement of light within the core. Historically, the O-band ('O' stands for Original) wavelength windows around 1300 nm and the C-band ('C' stands for Conventional) around 1550 nm have been the preferred operating wavelength windows for telecommunication systems due to the low attenuation coefficients ($\sim$0.35 and 0.2 dB/km, respectively) and chromatic dispersion coefficients (0

and 17ps/(nm.km), respectively) in these windows. PON standards have historically used a mixture of O- and C-band channel allocations. However, as PON data rates continue to increase, system power budgets will become harder to meet in the O-band due to the higher loss, so in this thesis work the focus is confined to C-band operation. Pragmatically, this choice is also driven by the current lack of commercial availability of the required enabling components for coherent systems research in the O-band, although in principle the concepts developed in this thesis are equally applicable in both O- and C-bands and indeed other wavelength regions.

Theoretically, the propagation of optical signals in optical fibers can be represented by the non-linear Schrödinger equation [33] as follows:

$$\frac{\partial \mathbf{E}}{\partial z} = \frac{\alpha(z)}{2}\mathbf{E} + \frac{j\beta_2}{2}\frac{\partial^2}{\partial t^2}\mathbf{E} + j\gamma\left|\mathbf{E}\right|^2, \tag{2.11}$$

where $\mathbf{E}$ is the electric field that propagates over spatial dimension z and varies in time t, while α and β_2 are the fiber propagation constants representing the attenuation and dispersive group delay, respectively. On the right side of this equation, the first and second terms represent the parameters of the attenuation and chromatic dispersion of the fiber, respectively. The parameter γ is the fiber non-linearity coefficient; hence the last term of this equation represents the non-linear phase modulation of the propagating light due to the Kerr effect. The fiber attenuation coefficient can be presented as a in units of dB/km as:

$$\alpha = \frac{10}{z} log_{10}\left(\frac{P_{out}}{P_{in}}\right), \tag{2.12}$$

where z is the fiber length, and P_{out} and P_{in} are the output and input power of the fiber channel, respectively [34].

In addition to the attenuation profile, chromatic dispersion (CD) is one of the major impairments in optical fiber communication. The information signal contains a range of frequency components, each of which experiences a different group velocity on propagation through the fiber. This causes the different frequencies of a given signal pulse to arrive at the output with different phases, resulting in the pulse spreading in time. Consequently, the received signal is distorted, and the spreading of the pulses causes interference with subsequent pulses, a phenomenon called inter-symbol interference. The total dispersion is made up of a combination of the dispersion of the silica glass material itself and the waveguide

dispersion resulting from the geometry and index profile of the optical fiber [34]. When solving for the second term only in Equation 2.11, the CD can be modeled as an all-pass filter transfer function given by:

$$H_{CD}(\omega, z) = exp\left(-j\frac{B_2}{2}\omega^2 z\right), \tag{2.13}$$

where ω is the angular frequency. Typically, in an optical communication system, the chromatic dispersion is specified as the dispersion parameter D at a given wavelength, λ as:

$$D = -\frac{2\pi c\beta_2}{\lambda^2} \quad ps/nm \cdot km. \tag{2.14}$$

Finally, the third term in Equation 2.11 represents the Kerr nonlinearities effect that can be described as changes in the refractive index silica glass in the optical fiber in proportion to the incident power of the optical signal. This effect is represented by the non-linear coefficient γ as:

$$\gamma = \frac{n_2\omega_0}{cA_{eff}}, \tag{2.15}$$

where n_2 is the refractive index parameter, A_{eff} is the effective area of the SMF and ω_0 the angular frequency of the optical carrier. In the case of phase-modulated signals, changes in refractive index during signal propagation can induce intensity-dependent phase modulation on optical pulses, known as self-phase modulation (SPM), resulting in spectra broadening. This nonlinear phase shift can be given as:

$$\phi_{SPM} = \gamma P_{Tx}\left(1 - exp(\alpha L)\right), \tag{2.16}$$

where L is the span of fiber propagation, and P_{Tx} is the launched power onto the optical fiber. However, this impairment is not typically critical in the context of the access network, as the launch power of the transmitter is usually not too high and the propagation distances are relatively low (a few tens of kilometers) . For example, the optical transceiver of class N1 (from the latest ITU-T standard 50G-PON [9]) is specified to transmit an output power of +5.5 to +11 dBm into 20 km of optical fiber. Nevertheless, the impact of non-linearity on the receiver sensitivity was investigated in Section 2.5.3 for completeness.

2.2.3 Polarization Mode Delay

Polarization is a property of electromagnetic waves that governs the orientation of the transverse electric field. Considering a dual-polarization case; two orthogonal polarization states of the light are utilized to convey the information. As a result of fiber birefringence, each polarization of light travels at a different group velocity, which leads to a difference in propagation time between the two polarizations at the receiver. Due to changes in temperature, stress, and mechanical vibrations on the cable, the polarization states evolve rapidly with time leading to fluctuating impairments, in contrast to the static impairments considered up to this point. This rapid change in the state of polarization (SOP) along the optical fiber can be emulated as a unitary 2×2 Jones matrix [35], H as follows:

$$H = \begin{bmatrix} \sqrt{\alpha}exp(j\delta) & -\sqrt{1-\alpha} \\ \sqrt{1-\alpha} & \sqrt{\alpha}exp(-j\delta) \end{bmatrix}, \tag{2.17}$$

where α and δ represent the power and phase change between the fast and slow polarization axes. Although polarization-maintaining fibers can preserve the SOP during propagation, these fibers are expensive and exhibit higher attenuation coefficients compared to SMF so are not used in deployed networks. However, by utilizing DSP technology in the coherent receiver, polarization de-multiplexing and recovery can be performed by adapting to the rapid changes introduced by polarization mode delay (PMD) impairments. Section 2.3.3 discusses how this impairment can be adaptively tracked and compensated for to recover the signal information by using DSP.

2.2.4 Phase Noise

Phase noise is a critical impairment in a coherent system, as the phase of the optical field is utilized to carry the information. In the context of this work, the phase noise is determined from the finite 3-dB linewidth properties (Δv) of the transmitter and LO lasers and is defined as the random variations of phase over time, which can be modeled as a random walk effect (known as the Wiener process) as:

$$\sigma^2 = 2\pi\Delta v T, \tag{2.18}$$

where T is the observation time window. Section 2.5.2 discusses how this noise would be influenced by the baud rate and the modulation format of the signal.

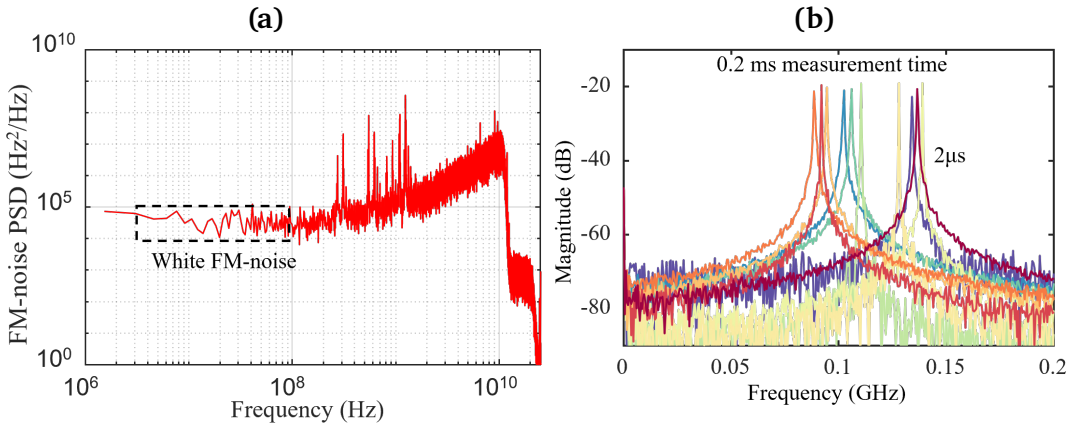


Figure 2.6: (a) Example FM-noise spectrum of a semiconductor laser using a delayed self-heterodyne setup. (b) Field spectra of beat tones between two ECLs in an experimental setup where the two ECLs were connected to the coherent receiver inputs and the output waveform was taken within 0.2 ms time window; each spectra plotted here has a span of 2 μs.

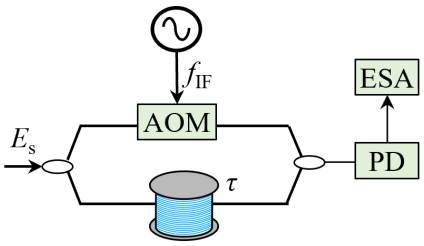


Figure 2.5: Delayed self-heterodyne method to measure the FM-noise of a laser. AOM: Acousto-optic modulator. ESA: Electrical spectrum analyzer.

The frequency-modulated (FM) noise spectrum is commonly used to describe the Fourier domain frequency noise of a laser. This can be measured, for example, with delayed self-heterodyne detection as illustrated in Figure 2.5, to obtain the power spectral density of the beat spectrum, as long as the delay path is greater than the coherence time of the input light [36, 37]. Figure 2.6(a) depicts the FM noise of an external cavity laser using the setup shown in Figure 2.5. The measurement was taken experimentally with a 10 km fiber used as the delay line. The AOM was used to frequency-shift the signal in one of the paths by 35 MHz. As a result, the incoherent mixing of the frequency-shifted optical signal with its delayed version detected by a PD to generate a beat signal at an intermediate frequency f_{IF}. Then, the optical linewidth can be measured from the width of the Lorentzian spectral line and is associated with a white frequency-independent FM noise spectrum [38]. Thus, by referring to the flat-frequency regime of the FM-noise power spectral density, the full width at half-maximum linewidth of a laser can be measured quantitatively. Throughout the thesis, this FM-noise measurement is used to describe the laser linewidth and phase noise properties of a laser.

In addition to 'white' FM noise, a laser also suffers from slow but large frequency

deviations in the regime below 1 MHz, also known as flicker noise, which arises from mechanical coupling, vibrations, power supplies, and electrical circuits [39, 40]. The impact of flicker noise on coherent detection can be examined in Figure 2.6(b), showing an example of the multiple spectra of a beat signal (configured at 0.1 GHz frequency offset) between the two tunable lasers, which experience frequency dither over a long measurement time (2 μs). Although this issue can be suppressed by having a stabilized laser control system, these slow fluctuations can also be mitigated in DSP by compensating for frequency offset of the signal [41].

2.3 Post-Digital Signal Processing

Some conventional modulation formats, such as NRZ or pulse amplitude modulation (PAM) use a direct detection method known as the IM/DD scheme. In direct detection, the output of the detector is proportional to the optical intensity which is in turn proportional to the square of the input signal electric field magnitude, according to the square-law principle. While the direct detection has the practical advantage of being simple to implement, it does not allow for the post-compensation of linear channel distortions like CD and PMD. On the other hand, coherent detection is a linear process that preserves complex tributary I and Q information, enabling linear equalization to effectively compensate for CD, PMD, and phase noise in the digital domain.

In this section, the author will discuss the operations of DSP in the coherent receiver. The incoming signals from the front-end receiver consist of phase and polarization diversity components (XI, XQ, YI, and YQ) which are processed by a series of DSP blocks. These blocks are designed to restore the baseband signals by compensating for channel impairments, polarization demultiplexing, equalization, and phase de-rotation prior to signal decoding.

The DSP procedure typically involves a sequence of operations, as depicted in Figure 2.7. Prior to DSP, the four-channel ADCs sample the received waveforms asynchronously to generate the digitized complex terms, which can be expressed as:

$$\begin{aligned} X_{ADC}(n) &= i_{c,XI}(n) + j * i_{c,XQ}(n), \\ Y_{ADC}(n) &= i_{c,YI}(n) + j * i_{c,YQ}(n), \end{aligned} \tag{2.19}$$

where X_{ADC} and Y_{ADC} represent the raw data tributaries X and Y polarization

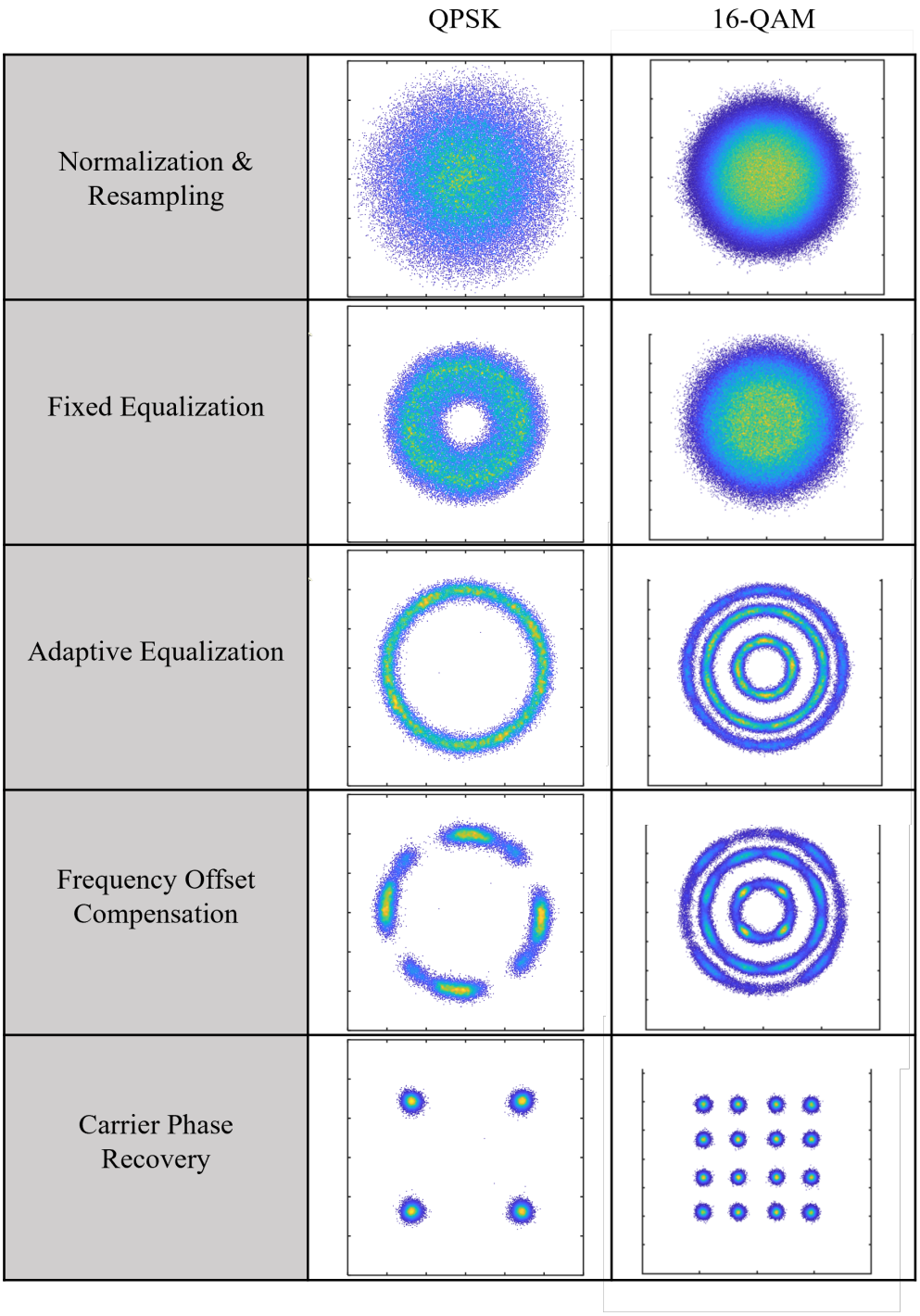


Figure 2.7: Digital signal processings flow to compensate for impairments and to recover the data stream. Constellation diagrams of both QPSK and 16QAM modulation signals were taken after the associated DSP blocks to illustrate the data processing.

of the signal, respectively. According to the Nyquist–Shannon sampling theorem, the required sampling frequency of the ADCs to capture the waveform is at least twice the symbol rate to overcome the aliasing effect.

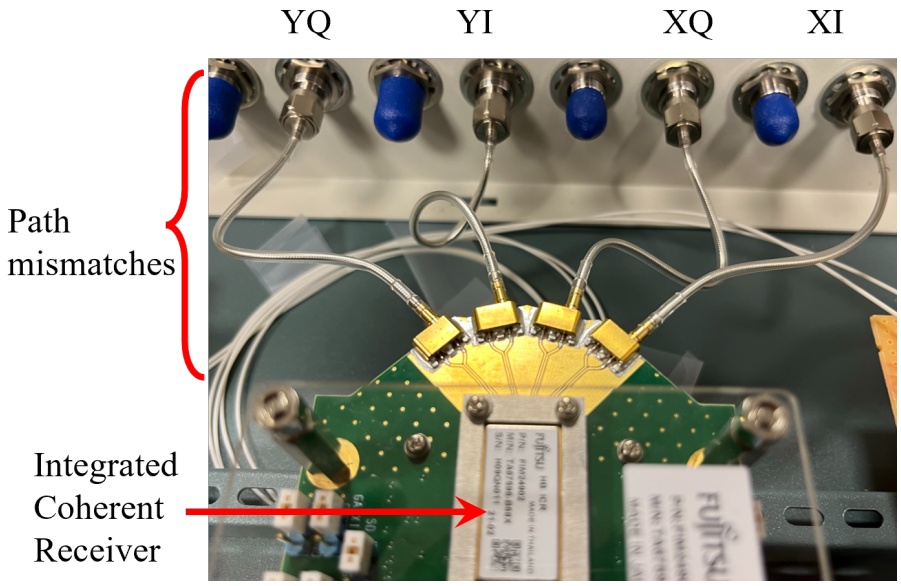


Figure 2.8: An example of the I-Q channel imbalance induced due to the path mismatches of the RF cables connecting from an integrated coherent receiver to the oscilloscopes

2.3.1 I-Q Imbalance Compensation

The delay skew between the I and Q components is primarily caused by path length mismatches in the front-end receiver and cable, as exemplified in Figure 2.8. In addition, imperfections in the design of receiver components, such as the 90° optical hybrid, balanced photodetector, and transimpedance amplifier, can also lead to differences in phase and amplitude between the I and Q components of the signal.

To mitigate this impairment, the Gram-Schmidt orthogonalization algorithm is implemented to correct the I-Q phase and gain imbalances [42]. By normalizing the signal to unity power and vector rotation by the same angle, a mutually orthogonal vector on the signal constellation can be achieved, hence compensating for the I-Q gain and phase mismatches. The orthonormal output signals from this operation can be mathematically represented as:

$$\begin{aligned} I_{out} &= I_{in}/\sqrt{\{(I_{in})^2\}}, \\ Q_{out} &= Q_{in}/\sqrt{\left\{\left(Q_{in} - \frac{\rho I_{in}}{\{(I_{in})^2\}}\right)^2\right\}}, \end{aligned} \tag{2.20}$$

where ρ is the correlation coefficient of the mean input signal and $\{\cdot\}$ denotes

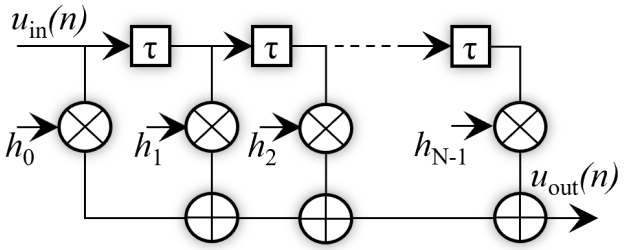


Figure 2.9: Basic structure of an FIR filter with a length of *N* taps

the averaging operator.

2.3.2 Static Equalization

In theory, using a static digital filter for equalization can effectively compensate for any level of chromatic dispersion, thus eliminating the need for a dispersion-compensating fiber (DCF) from the optical link. The static filter can be designed based on the inverse of the CD transfer function (using the second-order approximation in Equation 2.11), which can be expressed as:

$$\begin{aligned} H_{filt,CD}(\omega) &= \frac{1}{H_{CD}(\omega)}, \\ H_{CD}(\omega) &= exp\left(-\frac{j\omega^2\beta_2 z}{2}\right), \end{aligned} \tag{2.21}$$

where λ is the central wavelength of the carrier signal, β_2 is the dispersion group delay parameter, c is the speed of light, and z is the length of the fiber. By using this transfer function, an equalizer based in the time domain can be implemented as the *N*-tap finite impulse response (FIR) filter configuration, as shown in Figure 2.9 where both output $u_{out}(n)$ and impulse response $h_{CD}(z,t)$ are derived as:

$$\begin{aligned} u_{out}(n) &= \sum_{k=0}^{N-1} h_k u_{in}(n-k), \\ h_{CD}(z,t) &= \frac{1}{2\pi j\beta_2 z} exp\left(-j\frac{t^2}{2\beta_2 z}\right), \end{aligned} \tag{2.22}$$

where integer multiples of τ are used to delay the input signal, $u_(in)$. If large numbers of taps are used, the discrete $h_{CD}(z,t)$ can be approximated as a continuous-time impulse response and can compensate for a large dispersion value. In Section 2.4.1, the author analyzed the performance of static equalization over the accumulated CD in the fiber.

2.3.3 Adaptive Equalization

As mentioned in Section 2.1, the polarization state of the signal in the receiver differs from that of the signal transmitted due to fiber birefringence. In addition, this change evolves randomly with time because of fiber birefringence fluctuations. The purpose of the dynamic/adaptive equalizer block is to compensate for time-varying impairments in the channel. In contrast to static equalization, the adaptive equalization DSP compensates for dynamic Jones rotation (where the SOP dynamically changes during fiber propagation) and PMD. In this context, a butterfly-structured FIR filter with 2×2 multiple inputs and multiple outputs (MIMO) configuration (as depicted in Figure 2.10) is employed to estimate the inverse Jones matrix of the channel. This approach enables the demultiplexing and rotation of the X and Y polarization tributaries by recovering the SOP and compensates for residual channel impairments such as chromatic dispersion.

Following the Jones matrix shown in Equation (2.17), the output complex of this equalization filter can be given as:

$$\begin{bmatrix} X_{out} \\ Y_{out} \end{bmatrix} = \begin{bmatrix} H_{xx} & H_{yx} \\ H_{xy} & H_{yy} \end{bmatrix} \begin{bmatrix} X_{in} \\ Y_{in} \end{bmatrix}, \tag{2.23}$$

where H_{xx}, H_{xy}, H_{yx}, and H_{yy} denote the equalizer tap vectors. The tap weights have a length of N_{Tap}, and can be updated using commonly used error convergence algorithms in coherent systems such as the Constant-Modulus Algorithm (CMA) and Decision-Directed Least Mean Square (DD-LMS). In CMA, the tap

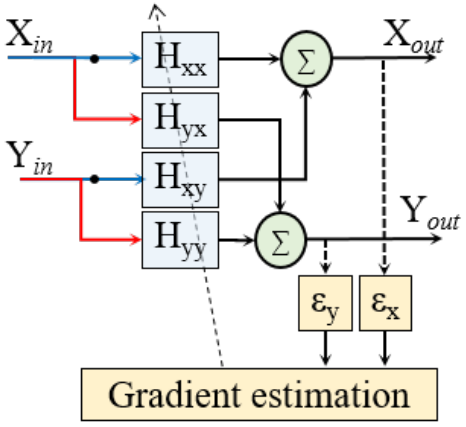


Figure 2.10: Basic structure of 2×2 MIMO adaptive FIR filters.

filters are updated as

$$\begin{aligned} H_{xx}(n+1) &= H_{xx}(n) + \mu\varepsilon_x X_{in} X^*_{out}(n), \\ H_{yx}(n+1) &= H_{yx}(n) + \mu\varepsilon_x X_{in} Y^*_{out}(n), \\ H_{xy}(n+1) &= H_{xy}(n) + \mu\varepsilon_y Y_{in} X^*_{out}(n), \\ H_{yy}(n+1) &= H_{yy}(n) + \mu\varepsilon_y Y_{in} Y^*_{out}(n), \end{aligned} \tag{2.24}$$

where μ and ε refer to the step size and the error function, respectively. The superscript $(\cdot)^*$ denotes the complex conjugate operation. The error terms can be given as:

$$\begin{aligned} \varepsilon_x(n) &= 1 - |X_o(n)|^2, \\ \varepsilon_y(n) &= 1 - |Y_o(n)|^2. \end{aligned} \tag{2.25}$$

For higher modulation formats such as 16QAM, the error term in CMA can never converge to zero. Hence, the CMA can be adapted to the radius-directed equalization (RDE) where its error terms can be computed as:

$$\begin{aligned} \varepsilon_x(n) &= R_d\left(|x_o(n)|^2\right) - |X_o(n)|^2, \\ \varepsilon_y(n) &= R_d\left(|y_o(n)|^2\right) - |Y_o(n)|^2, \end{aligned} \tag{2.26}$$

where $R_d(x_n)$ is the radius of the ring that is closest to the symbol x. Alternatively, adaptive equalization can be done using a DD-LMS algorithm, which is initialized by a training sequence, and its error term can be calculated as:

$$\begin{aligned} \varepsilon_x(n) &= D\left\{x_o(n)\right\} - |X_o(n)|, \\ \varepsilon_y(n) &= D\left\{y_o(n)\right\} - |Y_o(n)|, \end{aligned} \tag{2.27}$$

where $D\left\{x\right\}$ represents the symbol closest to x. The initial tap-weight calculation is trained using data-aided sequences before transitioning to decision-directed processing to ensure reliable convergence for each incoming signal. In the presence of phase noise, the equalization process can be modified to compensate for this by making decisions on the phase of each symbol within the equalizer loop. Compared to the previous algorithm, RDE offers lower latency than DD-LMS, since the error terms are computed directly from the filter output.

2.3.4 Carrier Frequency Offset & Phase Recovery

In intradyne detection (where the frequency offset between the signal and LO is within the receiver bandwidth), the transmitter and LO lasers are free-running and not frequency-locked. This results in a residual frequency offset impairment in the signal, which must be estimated and compensated for. Similarly, phase noise would impair the signal by rotating the constellation about the origin and, therefore, requires carrier tracking in the DSP. A digital coherent receiver can estimate both phase noise and frequency offset by implementing a tracking-based algorithm using a feedforward structured algorithm as illustrated in Figures 2.11 and 2.13, respectively.

The frequency estimation method presented and used in this work is based on peak power search methods in the frequency domain [43]. The operation of the fourth power operation $(.)^4$ shown in Figure 2.11 removes the modulation from the input signal and, therefore, exhibits a peak in the spectrum at four times the offset frequency. Then, this estimation is used to frequency shift the input signal and eliminate the frequency offset between the signal carrier and the LO, thus preventing the constellation rotation effect as shown in Figure 2.7. From this algorithm, the estimated frequency offset Δf_{est} can be expressed as:

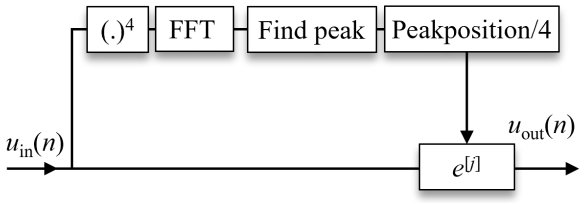


Figure 2.11: Block processing of frequency offset estimation technique based on peak power search.

$$\Delta f_{est} = \frac{1}{2\pi T_s} arg \left\{ \sum_{L}^{n=1} u_{in}(n) u_{in}^{*}(n-1)^4 \right\}, \tag{2.28}$$

where L is the averaging span, u_{in}^{*} is the complex conjugate of the input signal, and T_s is the symbol period. Figure 2.12 shows the simulated performance of this algorithm to compensate for the varied frequency offset between the transmitter and receiver sides. The simulation block diagram is presented in Section 2.4.1. The frequency offset is effectively estimated over a wide range of frequencies, in this example up to 100 MHz away. Therefore, by applying the frequency-shift to the input signal, the offset impairment can be compensated for.

A similar approach is used in carrier phase recovery (CPR) processing, where the

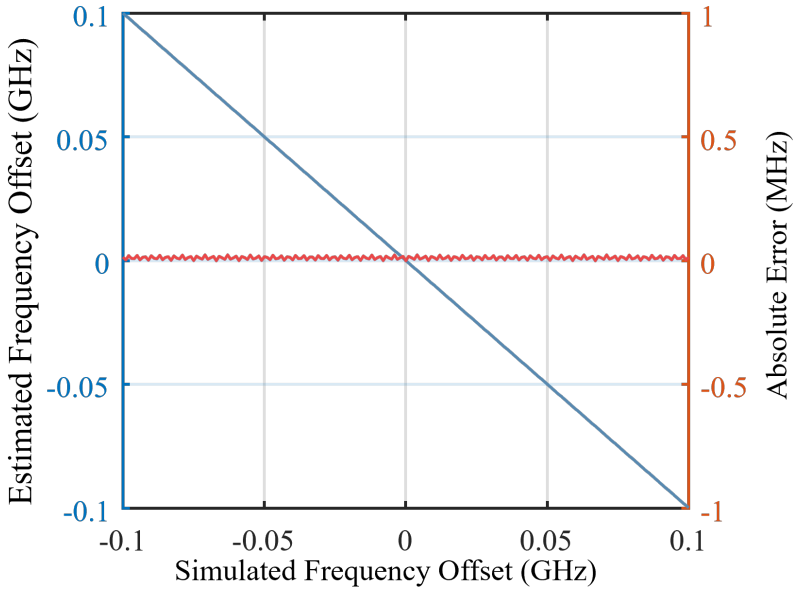


Figure 2.12: Estimated frequency offset measured from the simulated signal transmission (left axis) and the relative error between the estimation and simulation offset values (right axis).

fourth-order operation is implemented to remove phase modulation, as illustrated in Figure 2.13, giving the estimated phase as

$$\theta_{est}(n) = \frac{1}{4} arg \left[\sum_{k=-(N-1)/2}^{(N-1/2)} u_{in}(n+k)^m \right]. \tag{2.29}$$

The phase estimation algorithm based on Viterbi-Viterbi algorithm [44] can be optimized for carrier phase recovery by choosing the optimal symbol length in process block L for averaging. Each block undergoes processing to the fourth power to eliminate phase modulation. The resulting averaged phase is then divided by four to yield the estimated phase evolution. Finally, the received signal is phase-shifted by this estimated phase error to compensate for phase noise prior to symbol decoding. For higher modulation format such as 16QAM,

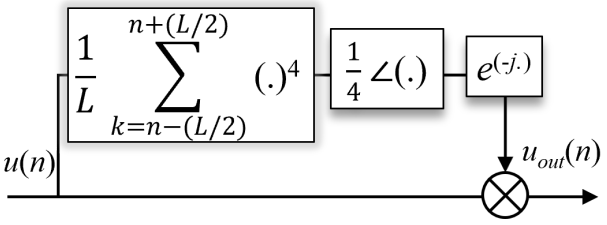


Figure 2.13: Block processing of CPR based on feed-forward estimation. $\angle(\cdot)$ represents the phase of complex number.

the algorithm can be adapted to QPSK partition scheme where the constellation points are divided into subgroups of QPSK signal rings, thus allowing multi-stage Viterbi-Viterbi phase estimation to be performed as described for QPSK [35].

For algorithm optimization, insufficient symbol averaging length can lead to inaccurate phase error tracking due to noisy estimated phase fluctuations, while selecting a longer symbol averaging length can result in narrow-band filtering, leading to imprecise estimation. This estimation is considered for Lorentzian laser linewidth shapes. Figure 2.14 demonstrates that optimal symbol averaging length (in red trace) enables accurate tracking of the estimated phase error to the simulated laser phase noise intrinsic to the system (vertically shifted for clarity).

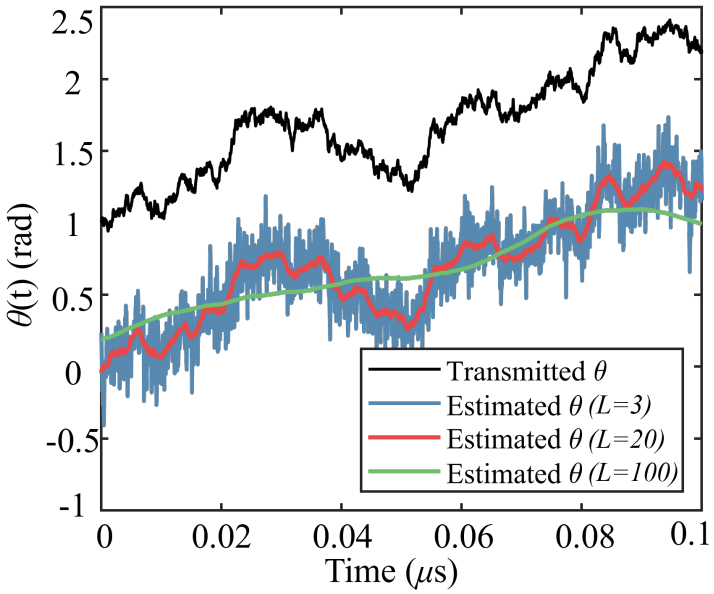


Figure 2.14: Simulated Wiener laser phase noise by using system modelling presented in Section 2.4.1 later. The total linewidth of the system was set to 100 kHz as shown in black trace. The estimated phase was generated by using the Viterbi-Viterbi algorithm with different symbols averaging L.

2.4 Sensitivity Assessment of a Coherent Receiver

So far, an overview of conventional optical coherent transmitter-receiver, DSP, and optical communication impairments has been discussed. In this section, the transmission performance of such a system is analyzed and the power sensitivity limit of an optical receiver is assessed, as this will be important for comparison purposes in the later work. The author has modeled a coherent signal transmission system based on numerical derivations of each module's functionalities. Some of the simulation parameters refer to the device/module specifications used in subsequent experimental work. Optical transmission experiments were then conducted using a commercial coherent receiver to evaluate its sensitivity performance over the fiber link.

2.4.1 Simulations

System Modeling

The system simulation is illustrated in Figure 2.15 and was numerically modeled in MATLAB. First, a random binary sequence was generated and mapped into a vector of complex data sequences based on the number of polarizations and modulation formats, such as QPSK and 16QAM. The symbols were subsequently pulse shaped with a raised-cosine filter followed by up-sampling to 16 samples per symbol for optical bandwidth modelling, and the addition of phase noise to simulate the impairment arising from the transmitter laser linewidth. The signal was then transmitted over a fiber channel, which was modeled using a

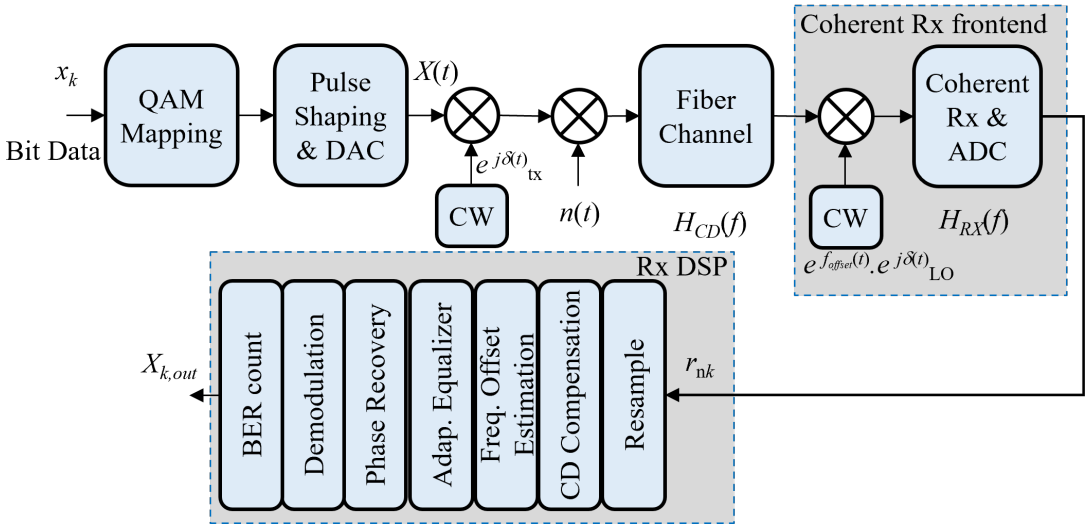


Figure 2.15: Block diagram of a coherent simulation setup.

Table 2.1: Simulation parameters

Parameter	**Value**	**Unit**	**Parameter**	**Value**	**Unit**
Baud Rate, B_d	*25*	*Gbaud*	*Signal Frequency,* f_c	193.41	*THz*
Tx Pulse shaping Filter Roll-off	*0.1*		*Dispersion Parameter*	17	*ps/nm .km*
Linewidth, δ_{Tx}	*100*	*kHz*	*Dispersion Slope*	80	s/m^3
Optical power, P_{Tx}	*+4*	*dBm*	*Nonlinear Index*	0.0013	*m/W*
$\text{RIN}_{Tx,LO}$	–140	*dB/Hz*	*Bandwidth* $_{Rx}$	40	*GHz*
Optical power, P_{LO}	*15*	*dBm*	$Freq_{offset}$	1	*MHz*
Responsivity_{PD}	0.07	*A/W*	Linewidth,δ_{LO}	100	*kHz*
Noise $\sigma_{Thermal}$	19	*pA/Hz*	ENOB_{ADC}	8	*bits*

split-step symmetric Fourier method (as described in Equation 2.11) to solve the non-linear Schrödinger equation numerically. In addition to CD impairments and third-order fiber non-linearity, the transmitted signal was also impaired by additive noise, $n(t)$, and attenuation of signal power.

At the receiver, the signal was mixed with an LO (adding phase noise and frequency offset between the transmitter and the LO laser) and then down-converted to the baseband signal. The receiver utilized a coherent quadrature receiver model with a 4th-order Bessel low-pass filter. Following this, a series of receiver DSP methods was employed to compensate for channel impairments and demodulate the received signal. These methods included resampling to 2 samples per symbol, time-domain chromatic dispersion compensation (static equalization), adaptive equalization based on the CMA or RDE algorithm, frequency offset estimation utilizing peak power search, and carrier phase recovery with the Viterbi-Viterbi algorithm Finally, digital demodulation and bit error counting were performed to measure the bit error rate (BER); which is a measure of the received signal's quality considering noise, interference, and distortions in a data transmission system. Table 2.1 details the parameters governing this simulation work.

Current coherent transceivers utilize hard-decision forward error correction (HD-FEC) with 7% overhead of the information bits to recover the bit signal [45]. This allows for the correction of the pre-FEC BER as high as BER=3.8×10^{-3} to ensure error-free signal transmission. Therefore, in this study and subsequent discussions, 'receiver sensitivity' refers to the received optical power (ROP) to achieve a BER of 3.8×10^{-3}.

Results: Receiver Sensitivity Performance

To validate the receiver sensitivity performance, the author adjusted the power of the received optical field and recovered the signal for different modulation formats and number of polarization schemes. In Figures 2.16(a), the simulation results are presented as BER versus the input power of the receiver with a constant LO power (+15 dBm) for both single and dual polarization schemes. The coherent receiver achieved superior sensitivity performance when employing the QPSK modulation format (≈5 dB gain) compared to the 16QAM modulation

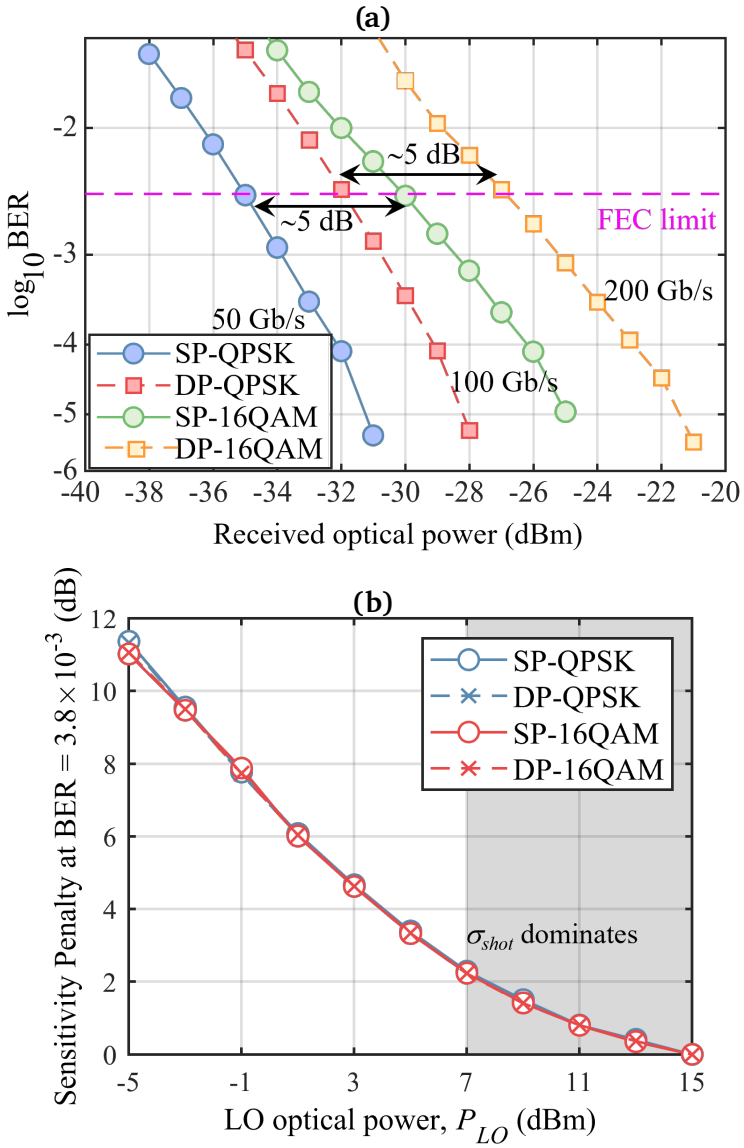


Figure 2.16: (a) BER versus received optical power for QPSK and 16QAM modulation formats on different transmission links with single-polarization, and dual-polarization operation. (b) Sensitivity penalty as a function of the LO power (P_{LO}) in the BtB link for different modulation formats.

format in both polarization schemes.

Although 16QAM offers more bits per symbol than QPSK, it is more susceptible to noise due to the closer spacing of symbols, as indicated in Figure 2.2, leading to a significant degradation in receiver sensitivity performance. Note that the 3-dB sensitivity penalty for dual-polarization multiplexing is because the results are plotted as a function of the total received power, so the power per polarization is 3dB lower in the dual polarization case compared to the single-polarization case.

The impact of LO intensity on receiver sensitivity penalty was evaluated and shown in Figure 2.16(b). Each penalty curve was plotted relative to the sensitivity performance at P_{LO}=+15 dBm. As the LO power increases, the receiver sensitivity also improves while almost reaching the saturation level at P_{LO}=+15dBm. This behaviour can be explained by Equation 2.10, where most of the photodiode noise is contributed by the thermal and shot noise. At lower LO power levels, thermal noise from the receiver dominates, determining the overall SNR based on the optical power of both the received signal (P_S) and the LO (P_{LO}). However, as the LO power surpasses a certain threshold, the shot noise term becomes dominant, resulting in only a small improvement in the SNR.

Results: CD Tolerances Performance

Finally, the impact of the accumulated CD from optical fiber transmission was analyzed. The author maintained a constant number of taps for the adaptive equalizer to isolate the impact on the performance of the static equalizer alone. Figure 2.17(a) shows that for a given total CD value, there exists an optimal number of taps for the static equalizer. This optimization enables the 25 Gbaud SP-QPSK system to achieve a receiver sensitivity of -34.6 dBm. Here, a sensitivity penalty margin of less than 0.4 dB is observed for transmission at 40 km (680 ps/nm) employing an equalizer of 11-taps or more compared to the BtB case. To demonstrate the effect of chromatic dispersion in the fiber, Figure 2.17 (b) shows the pulse broadening response at different fiber distances. It is evident that as the fiber span increases, the pulse undergoes a more dispersion-induced broadening. This broadening may lead to inter-symbol interference as the dispersive pulse extends into neighboring pulses. Consequently, this would require a large FIR filter size to compensate for a large accumulated CD. Although a large filter size is crucial for fiber transmission optimization, it also increases the design complexity and power consumption in the receiver DSP.

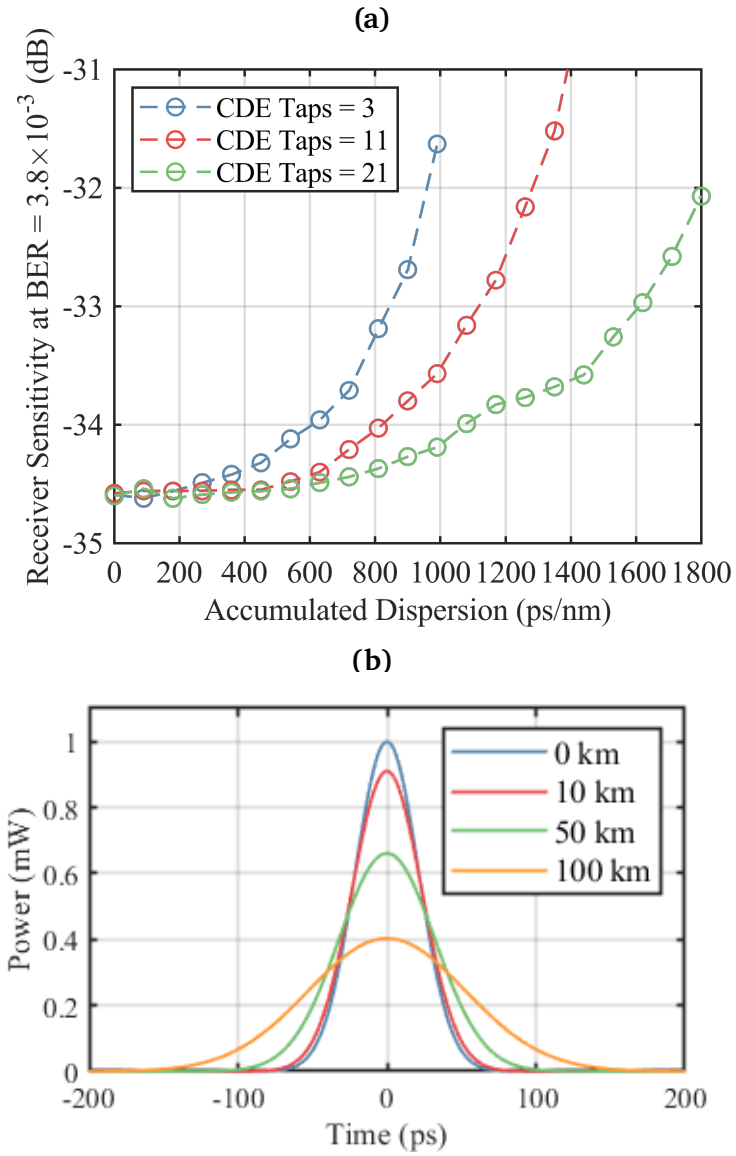


Figure 2.17: (a) Performance of the coherent receiver sensitivity against accumulated CD with varied number of taps of chromatic dispersion equalizer. (b) Dispersion-induced broadening of a Gaussian pulse in a fiber transmission at different fiber lengths.

2.4.2 Experiments

Experimental Setup

The experimental setup for the coherent fiber transmission system for 50 Gb/s and 100 Gb/s data rates is depicted in Figure 2.18(a). On the transmitter side, an external cavity laser (ECL) with a wavelength of 1553.1 nm and a specified linewidth of around 30 kHz was modulated using a coherent optical transmitter (Tektronix OM5110), driven with random signal sequences of length 2^{15} at a

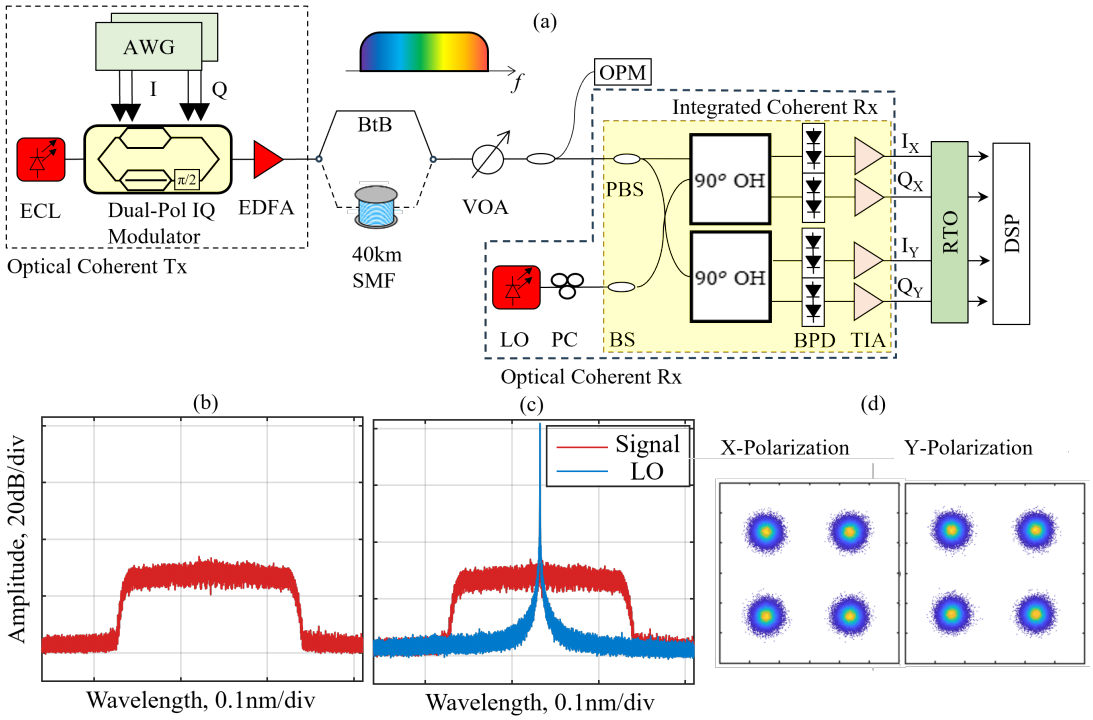


Figure 2.18: (a) Experimental setup for optical coherent transmission system of 50 and 100 Gb/s of single- and dual-polarization QPSK respectively. (b) Captured optical spectrum of transmitted signal centered at 1553.1 nm wavelength. (c) Optical spectrum used for comparison between transmitted signal with LO. (d) Recovered constellation of DP-QPSK at −22 dBm receive power.

speed of 25 Gbaud; generated by an arbitrary waveform generator (AWG) of 50 GSa/s (Tektronix AWG70001A). This resulted in a single- and dual-polarization QPSK signal with a total bit rate of 50 and 100 Gb/s, respectively. An erbium-doped fiber amplifier (EDFA) was used to amplify the optical signal power up to +4 dBm to compensate for insertion losses from the transmitter and adjust the optical power launched into the fiber channel. The launched optical signal spectrum is depicted in Figure 2.18(b).

This experiment used the back-to-back (BtB) channel configuration or 40 km fiber length based on the G.652 optical fiber standard as the channel link. These link configurations were used for subsequent work in the thesis. The ROP was controlled using a variable optical attenuator (VOA), and the optical intensity was measured using an optical power meter (OPM) before it reached the receiver.

The author employed a commercial micro-integrated coherent receiver (ICR) with a specified 3-dB bandwidth of 40 GHz. Additionally, a second tunable ECL was used as the LO, with operating center wavelength and linewidth specifications similar to the transmitter laser. The optical spectrum depicted in Figure

2.18(c) shows the comparison of the signal and the LO prior to input into the coherent receiver. For single-polarization transmission, a polarization controller (PC) aligned the LO's polarization with the signal's polarization. Subsequently, the electrical signals from the receiver were sampled and digitized using real-time oscilloscopes (RTO, Tektronix DPO70002SX), followed by offline DSP using the block processing techniques described in Section 2.4.1.

Results: Receiver Sensitivity Performance

In a similar approach to the previous simulation work, the author varied the P_{LO} to examine the coherent receiver's sensitivity response. Figure 2.19(a) and (b) show the performance in BtB for single and dual polarization signals in terms of BER versus received optical power. The receiver exhibits shot-noise limitation behaviors as P_{LO} increases up to +13 dBm, which aligns with previous simulation findings. The receiver sensitivity can reach -37 and -34 dBm for SP and DP operation, respectively, illustrating the high-power sensitivity benefits of an optical coherent receiver. The value of the receiver sensitivity here is similar to the work in [46] which also showed the coherent receiver can achieve 14.3 dB higher receiver sensitivity compared to a direct-detection receiver (SOA + PIN). In a PON context, this suggests a high-link budget of up to 41 dB (given that the transmitted launch power at +4 dBm), supporting a high splitting ratio (1:64 or even 1:128). Figure 2.18(d) presents the constellation diagrams after post-processing, where the signal was captured at ROP=-25 dBm, demonstrating the

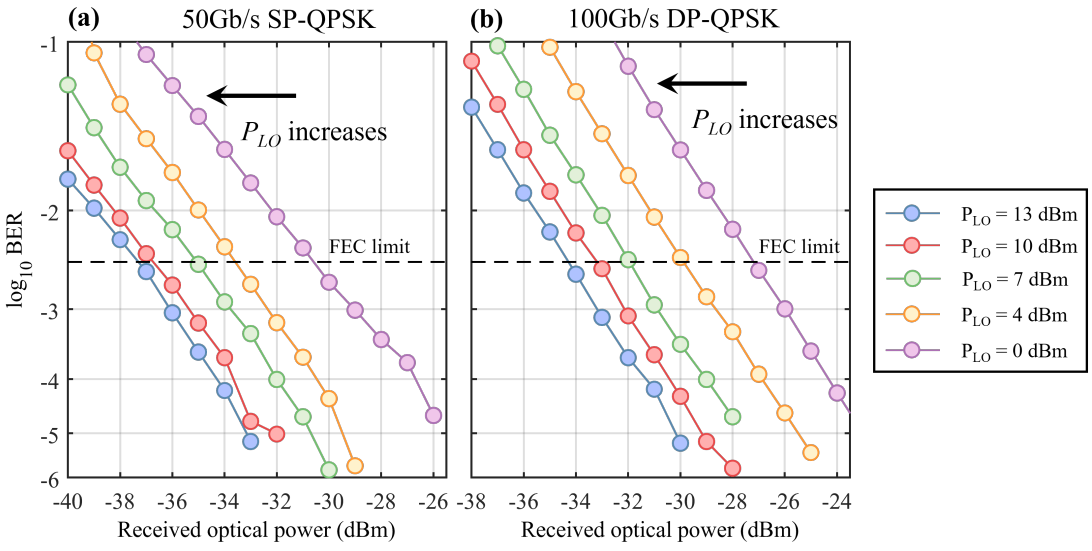


Figure 2.19: Experimental results of the ICR sensitivity performance of a single-carrier 25 Gbaud QPSK signals employing single-pol (left) and dual-pol (right) in a back-to-back link.

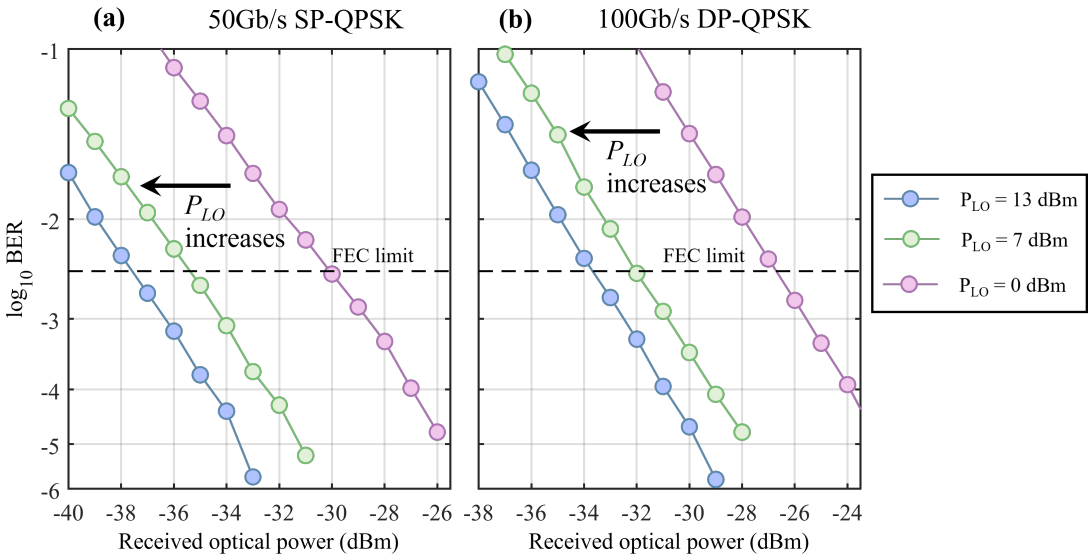


Figure 2.20: Experimental results of the ICR sensitivity performance over 40 km G.652 standard optical fiber.

effectiveness of the DSP in compensating for channel impairments to demultiplex and recover the received signal.

Additionally, Figure 2.20 shows the receiver sensitivity performance when the signal is transmitted over 40 km of optical fiber. At the FEC limit, the sensitivities achieved are the same as those of the BtB link, indicating that the static equalizer (filter size of 9 taps) effectively compensated for the CD introduced by the 40 km optical fiber. Considering that a 20 km reach is the current standard for an access network [47], achieving high receiver sensitivity performance over 40 km signifies a reasonable benchmark that anticipates potential future reach extensions.

2.5 Practical Limits & Technical Challenges for Access Networks

While a coherent receiver's excellent sensitivity can lead to high power budgets, which are highly desirable for high data rate PONs where splitting loss is a limiting factor, the high cost of the technology has so far prevented its deployment. The experimental work in the previous section provides important 'ideal case' performance benchmarking results, but it was conducted with laboratory-grade equipment that is not representative of what would be required for a cost-effective solution for coherent PON.

Minimizing receiver module specifications and selecting suitable system components are crucial strategies for achieving low cost whilst achieving performance optimization. In this section, the author investigates some key component parameters that impact cost , such as the bandwidth of the coherent optical receiver, the laser linewidth, and the optical launched power (impact of fiber non-linearity) in the access link.

2.5.1 Bandwidth Restrictions of the Receiver

In the context of this work, receiver bandwidth refers to the equivalent front-end bandwidth in the coherent receiver (including BPD, TIA, and ADC). This is a crucial concept to understand, as it directly impacts the receiver's performance and cost. Although in previous experiments, the receiver bandwidth was primarily limited by the RTO (with a specified 3-dB bandwidth of 33 GHz), it is more than sufficient to capture the 25 Gbaud signal bandwidth effectively.

In this simulation analysis, the author sweeps the receiver bandwidth to simulate the narrowing effect of the filter bandwidth in the coherent receiver. This

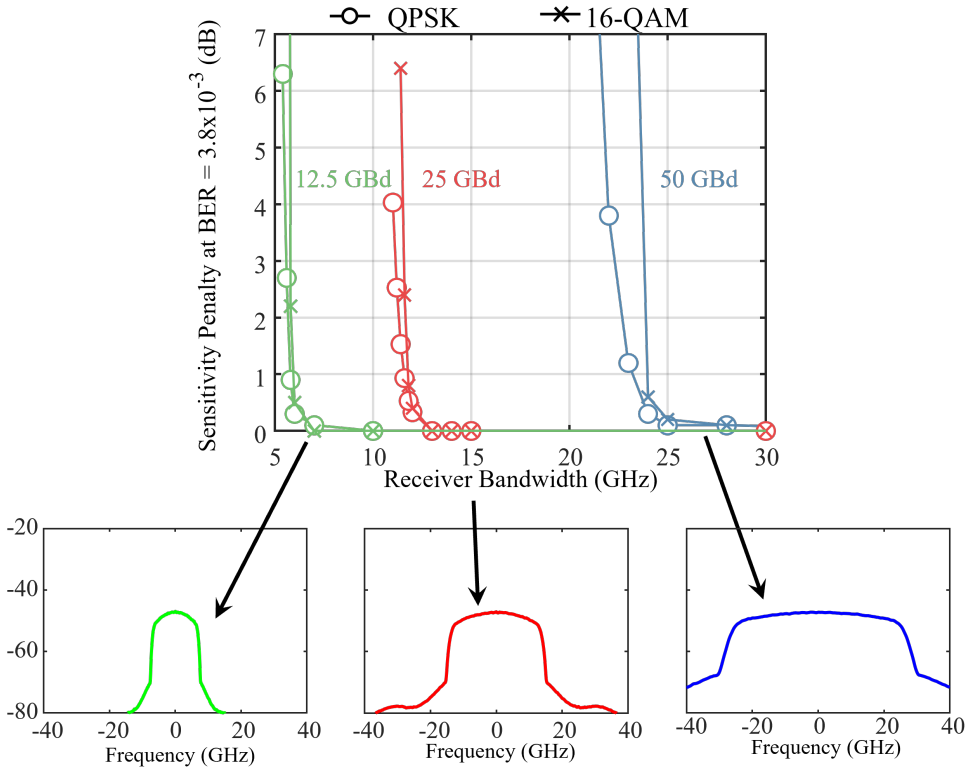


Figure 2.21: The receiver sensitivity tolerance with varied receiver bandwidths for three different baud rate operation. Insets show the associated spectra of the signal from each operating baud rate.

is achieved by varying the 3-dB filter bandwidth in the receiver model. The results depicted in Figure 2.21 show the impact on different baud rate operations using DP-QPSK and DP-16QAM modulation formats. Sensitivity benchmarks are measured at a receiver bandwidth of 33 GHz for all cases. It can be observed that optimal receiver bandwidths are measured at around half of the signal baud rate. The sensitivity penalty increases significantly as the receiver bandwidth is reduced beyond the optimum point due to the inter-symbol interference introduced by bandwidth restriction. The 16QAM case exhibits a sharper onset of significant penalties compared to QPSK, as multilevel modulation formats are more susceptible to SNR degradation due to the closer constellation point spacing.

The study suggests that for high baud rate operation, high-bandwidth optoelectronics and electronics are required, which can be a predominant cost in a photonics integration [48] and hindering the use of high-commodity, low-cost and low-bandwidth components for coherent PON (100G and beyond). The next chapter will explore how the spectral-slicing technique could enable continued 10G-class components [14] in the front-end receiver for higher-speed detection, potentially offering a cost-effective PON solution.

2.5.2 Phase Noise Tolerances

The laser linewidth has a significant impact on coherent system performance as described in Section 2.2.4, so it is important to study this aspect for conventional receiver systems in order to make a comparison with the spectrally sliced systems that are the focus of this work. A realistic linewidth tolerance analysis would be desirable through experimental demonstration to evaluate the impact of these linewidths. However, this is not realistic to achieve, as the linewidth depends strongly on the type and design of a laser. To address this, the author used a random walk noise process to emulate the magnitude of phase noise variance in a simulation platform. The receiver sensitivity performance in the BtB link without applied phase noise was then used as a benchmark to measure the sensitivity penalty over a linewidth range. The product of linewidth and symbol duration ($\Delta v \cdot T_d$) was quantified for phase noise measurements in the system, where Δv is the total laser linewidth (transmit and LO lasers) and T_d is the symbol period.

Figure 2.22(a) shows the receiver sensitivity penalty at FEC limit versus $\Delta v \cdot T_d$ where the Viterbi-Viterbi phase recovery algorithm was used to compensate for phase noise. When comparing the tolerance of the total laser linewidth in QPSK

to 16QAM at 1-dB sensitivity penalty, it is found that the total linewidth tolerance in 16QAM is measured at 1.75 MHz which is lower compared to QPSK (10 MHz).

The signal constellations without phase noise compensation are shown in Figure 2.22(b). Clearly, phase-domain inter-symbol interference is much larger in 16QAM compared to QPSK as the linewidth of the laser increases due to the stricter and closer spacing of the symbol constellation points. However, for QPSK, which is mainly used throughout the thesis due to its relative simplicity

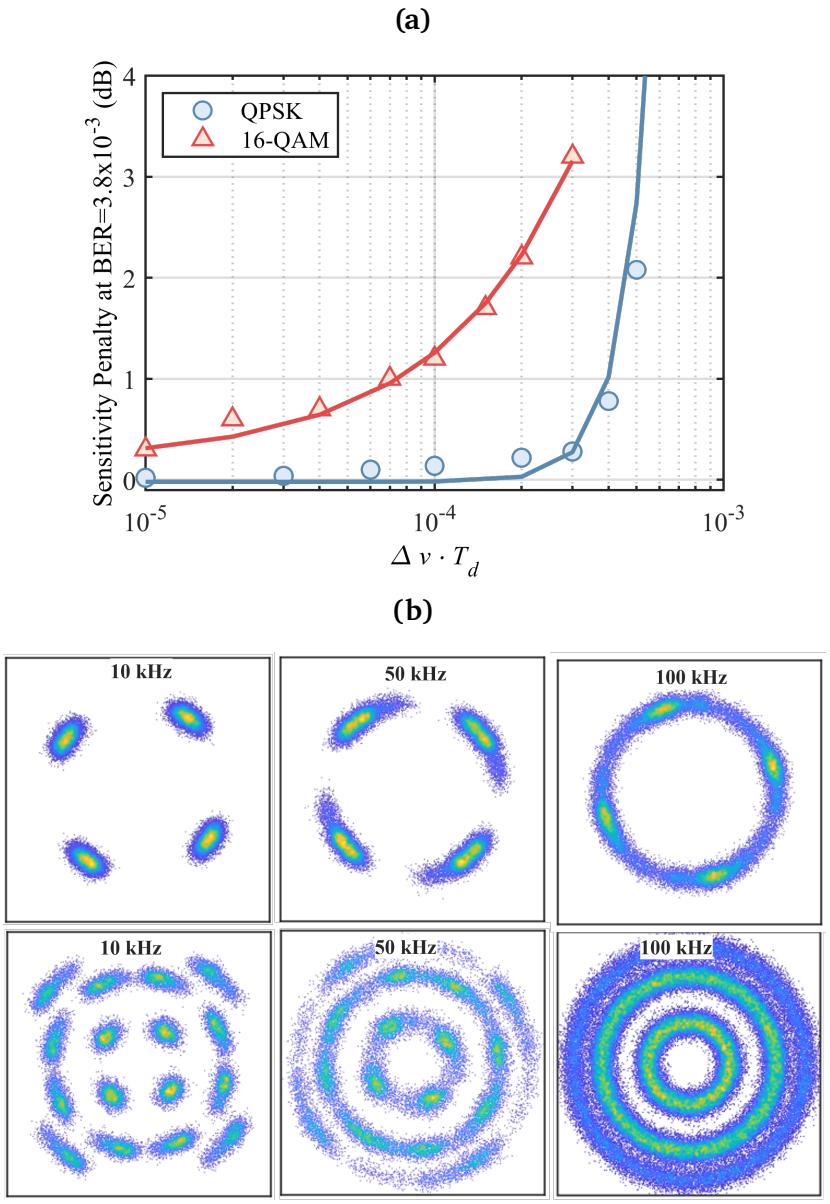


Figure 2.22: (a) Sensitivity penalty versus combined linewidths symbol duration products for QPSK and 16QAM modulation formats. (b) Constellation diagram without phase domain equalization using QPSK (top) and 16QAM (bottom) for different combined laser linewidths.

and higher receiver sensitivity (compared to 16QAM), can tolerate a total laser linewidth of up to 10 MHz at 25 Gbaud operation. The ECL which was used for the previous experimental works and hereafter has a linewidth measure at 30 kHz. For this magnitude, the laser would not be a limiting factor for the sensitivity performance in a coherent system.

2.5.3 Fiber Non-Linearities Constraints

The impact of fiber non-linearities is crucial, especially in long-haul transmission, where multicarrier transmission with high-launched optical power over long spans is used. However, in PON scenarios, fiber lengths are typically less than 40 km, and generally only two relatively widely spaced in wavelength carriers are used, one for upstream and one for downstream communication between the central office and the subscribers. Nevertheless, it is important to assess the expected impact of non-linear fiber propagation distortion on the optical link power budget in the coherent PON scenario.

When high optical power is launched into the fiber, the non-linear self-phase modulation occurs, leading to frequency chirping of the optical pulses. This spectral broadening increases the signal bandwidth and may limit the transmission performance.

To determine the optimal launched optical power over 40 km fiber, the author varied the launch power and assessed both linear and non-linear fiber distortions.

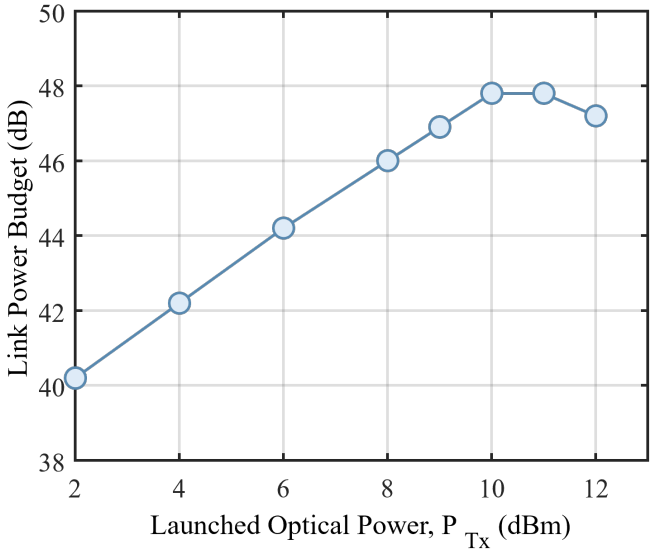


Figure 2.23: Optical link budget as a function of launch power.

The link power budget can be determined by measuring the receiver sensitivity at the FEC limit using the optical testbed illustrated in Figure 2.18(a). The measurement results for the 50 Gb/s data rate of SP-QPSK are presented in Figure 2.23. An optimal launch power of +10 dBm is achieved with a maximum link budget of 49 dB, even though the sensitivity is reduced due to the effects of fiber non-linearity. However, the launched power is kept at +4 dBm throughout the experiment work to avoid the receiver sensitivity performance being restricted due to fiber-nonlinearity impairments.

2.6 Summary

In this chapter, the author discussed coherent detection concepts and introduced conventional coherent transmitters and receivers in Section 2.1. The main impairments in the coherent system, especially those relevant to optical access network applications are highlighted in Section 2.2. The author also discussed the post-DSP to compensate for channel impairments and recover the transmitted signal in Section 2.3. Generally, digital coherent optics offer several advantages for fibre-optic communication, including:

- Enabling higher modulation formats by modulating the signal in various dimensions of the optical field, such as amplitude, phase, and polarization of the lightwave.
- Providing superior received optical power sensitivity, leading to a higher power budget for access network links.
- Utilizing DSP to compensate for fiber transmission impairments.

In addition to these benefits, the author evaluated the performance of a commercial coherent receiver in Section 2.4 over a 40 km optical fiber link. It was observed that by increasing the LO power towards shot-noise-limited performance, the receiver sensitivity could reach up to −37 dBm. The performance measurements will be used in the subsequent chapters as a conventional optical coherent receiver benchmark for comparison with spectrally sliced receivers.

Finally, the author presented further investigations on receiver bandwidth limitations, laser linewidth tolerance, and fiber nonlinearity in Section 2.5. Due to the cost-constrained requirements of the PON application, the current coherent receiver architecture is not ideal for mass deployment in the future access network. We will explore potential redesign and optimization solutions of the coherent receiver in the next chapter.

Chapter 3

Design of a Spectrally Sliced Coherent Receiver (SSRx) for Access Networks

Coherent optical communication offers numerous benefits to access networks, particularly due to its superior receiver sensitivity compared to direct detection approaches. This advantage becomes particularly critical as the required data rates for PON evolve into the hundreds of Gb/s regime, due to the increasing difficulty of meeting demanding PON link budgets with IM/DD solutions. However, coherent technology is relatively complex and costly, so there are significant barriers to achieving this in an access network where equipment cost is shared across only a relatively small number of end users. To address this, the author proposes a detection technique that could potentially reduce the overall cost of a coherent receiver. This technique is based on spectral slicing, allowing a transmitted signal to be received using an array of coherent receivers in a frequency-interleaving configuration. This approach would leverage low-bandwidth, cost-effective, and commodity components (photodiodes, TIAs and ADCs) in a coherent receiver.

This chapter introduces a series of analytical investigations and experimental demonstrations that govern the design, characterization, and optimization of an SSRx for access networks. This can be viewed as one of the key technical contributions of this thesis. Furthermore, the author demonstrates an SSRx operating at 100 Gb/s with a receiver sensitivity of –33 dBm, using front-ends with a reduced 3-dB bandwidth of 6.25 GHz. Lastly, the author discusses several challenges in implementing an SSRx in a PON system. Here, the author used the symbol N to denote the number of slices.

The spectrally coherent sliced receiver is the optical equivalent of the well-known electronic frequency-interleaved sampler [49, 50]. As illustrated in Figure 3.1, the SSRx incorporates a laser source that is capable of generating N coherent LO tones, enabling the wideband signal to be decomposed into N slices. Each slice is then detected by a separate conventional coherent receiver channel, with the critical advantage that each requires a lower (by a factor of $1/N$) optoelectronic and electronic component bandwidth. Subsequently, the signals undergo post-processing to recombine all the slices and reconstruct the original signal in the digital domain via DSP [51, 52].

This approach is similar to the frequency interleaving technique (known as digital bandwidth interleaving) used for high-speed ADCs [53, 54] in high-speed oscilloscopes. For instance, contemporary oscilloscopes boast sampling rates exceeding 100 GSa/s with acquisition bandwidth exceeding 60 GHz [55]. These oscilloscopes utilize a downconverter to set the LO frequency to the mid-band of the analogue front-end bandwidth. This results in one ADC acquiring the upper half of the scope passband signal and another ADC acquiring the lower half. Fi-

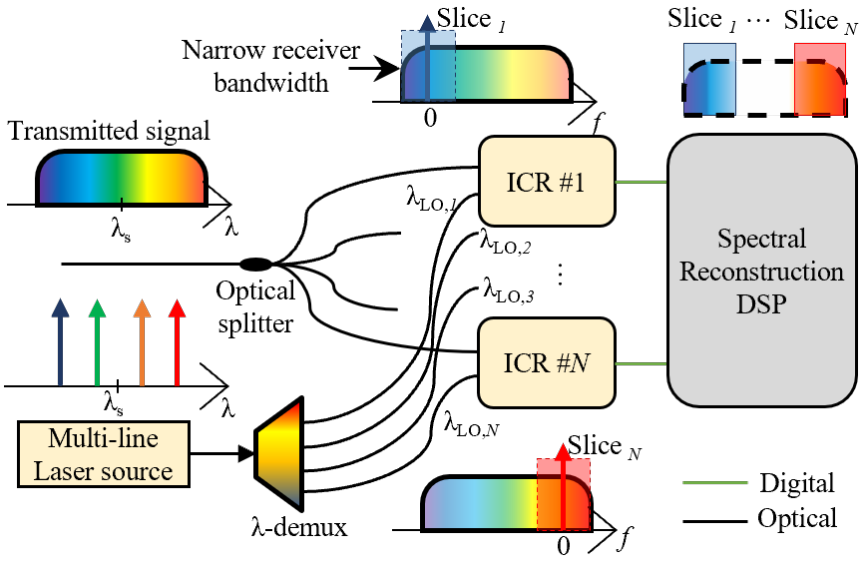


Figure 3.1: Schematic diagram of a spectrally-sliced optical coherent receiver. The received signal is split by a factor of N via an optical splitter and fed into an array of N-integrated coherent receivers. The multi-optical lines are separated by a wavelength de-multiplexer and act as LO that mixes with a portion of signal frequencies. After sub-signal photodetection and ADC readout inside the ICRs, N-complex signal slices are generated. Following the sub-ADC sampling, the whole signal spectrum can be reconstructed by "stitching" together each sampled slice using DSP; thus recovering the received signal.

nally, the complete waveform can be reconstructed by merging both passbands using DSP. Whilst the principle is similar, translating this technique to the optical domain with carrier frequencies in the 200 THz range is of course non-trivial and is still very much a focus of current research.

3.1 Motivations

The concept of spectral slicing, known as an optical arbitrary waveform measurement (OAWM), has been introduced to fully analyze the amplitude and phase of optical waveforms with over 160 GHz bandwidth [49]. It has been researched in various high-speed optical communication contexts [56, 57], such as achieving data transmission rates of up to 1.92 Tb/s [58], in elastic optical networking [59], neurophormic computing [60] and photonic-electronic ADC [61]. However, to the best of author's knowledge, the SSRx has received comparatively less attention as a potential solution for coherent system applications in future PON and this work is the first to propose and carry out a deep and thorough investigation of this potential application.

As the baud rate for the next-generation PON increases, the modulation signal's bandwidth also widens, necessitating high-bandwidth components in the front-end receiver, which can be costly. This work aims to explore whether spectral slicing can enable a continuation of the cost reduction trend in PON by utilizing older 10G class component technologies [14] within the context of coherent PONs.

The main idea is to use spectral slicing to reduce the bandwidth of optoelectronics in the receiver while only modestly increasing DSP complexity and overall power consumption for signal recovery. This may reduce the bandwidth of the RF components, including BPD, TIA and ADC, by a factor of N, potentially enabling the use of less expensive, low-power, and high-commodity components. In particular, using high-bandwidth ADCs significantly contributes to the cost and power consumption of a detector [62, 63]. In addition, anticipated advances in low-cost photonic integration circuit technology might enable the required parallelization of optical components, allowing for exploitation of the reduced requirements of the receiver RF front ends and ADCs. Consequently, these would reduce the cost of the coherent receiver, thus opening up new applications in future PON.

3.2 Theory of Spectrally-Sliced Detection

Slicing and reconstructing the incoming optical waveform involves complex steps relying on precise setup arrangements and parameters. To develop the spectral slicing model, the author starts with the transmitted signal derived from the previous chapter. The transmitted data, represented as a_m, for a single channel transmission, can be expressed in the form of a baseband signal as:

$$s(t) = \sum_{m} a_m h_{Tx}\left(t - mT_s\right). \tag{3.1}$$

Considering that pulse shaping $h_{Tx}(t)$ (representing the overall response of the transmitter system) is applied to the signal with a symbol period of T_s. The data is then applied to an I/Q modulator to modulate a laser beam with a center frequency of f_c. The transmitted single carrier optical signal with phase noise term of φ_s can then be expressed as:

$$E_s(t) = s(t)e^{j2\pi f_c t + \varphi_s}, \tag{3.2}$$

The optical fiber channel may be impaired with signal impairments such as chromatic and polarization mode dispersion, fiber non-linearity, and amplified spontaneous emission from optical amplifiers. However, for the purpose of focusing on the numerical theory of the SSRx detection and reconstruction processes, the author will only consider the ideal case of a back-to-back system and amplifier-free system. In this application, an LO that generates multiple optical lines is required, with frequencies within the signal bandwidth and centered at f_c is required. Therefore, the optical field for these LO lines can be expressed as:

$$\begin{aligned} E_{LO} &= \sum_{n=1}^{N} \sqrt{P_{LO,n}} e^{j2\pi\left(f_{LO,n}t + \varphi_{LO}\right)}, \\ f_{LO,n} &= \left(n-1\right) f_{FSR} + f_{LO}, \end{aligned} \tag{3.3}$$

where $P_{LO,n}$ represents the optical power of the *n*-th line, ϕ_{LO} is the phase term for the comb line assuming that the comb has perfect phase locking. The f_{FSR} and f_{LO} denote the frequency of the free spectral range and the first mode of the comb, respectively. As depicted in Figure 3.1 the LOs beat with the entire signal spectrum in *N* parallel coherent receiver branches to convert the optical signal into *N* sampled slices. The representation of the signal field from Equation 3.2,

and the LO (E_{LO}) from Equation 3.3 for the input of the *n*-th coherent receiver can be rewritten as:

$$\begin{aligned} E_{sig,n}(t) &= \sqrt{\frac{P_s(t)}{N}} e^{j2\pi\left(f_c t + \varphi_s(t)\right)}, \\ E_{LO,n}(t) &= \sqrt{P_{LO,n}} e^{j2\pi\left(f_{LO,n} t + \varphi_{LO}(t)\right)}, \end{aligned} \tag{3.4}$$

where P_s denotes the signal power. Assuming that each split signal and LO are co-polarized and using coherent detection, the complex output photocurrent comprising I and Q components generated from the *n*-th coherent receiver can be reconstructed as:

$$I_c(t) = 2R\sqrt{\frac{P_s(t)}{N} P_{LO,n}} e^{j2\pi\left(\Delta f_n t + \varphi_s(t) + \varphi_{LO}(t)\right)}, \tag{3.5}$$

where R is the PD responsivity, and the offset frequency between the carrier and *n*-th LO comb line is given by $\Delta f_n = f_c - f_{LO,n}$. Each photocurrent is then fed into an ADC, modeled as the combined baseband impulse response of the overall receiver (BPD, TIA and ADC) $H_{Rx,n}$, with the assumption that any skew between the I and Q channels has been calibrated and compensated for. Given that the *N* comb lines are within the signal spectral bandwidth and are equally spaced, $H_{Rx,n}$ can be optimized with the slice bandwidth BW_{Slice} as:

$$BW_{Slice} = B_d/2N, \tag{3.6}$$

where B_d denotes the bandwidth of the transmitted signal. To design a signal reconstruction chain, some assumptions concerning the frequencies and bandwidths of the signal, LO tones, and slices are made as follows:

- All slice bandwidths are identical to each other ($H_{Rx,n}$) and are within the signal spectrum bandwidth.
- If *N* is odd, the [(*N* + 1) / 2] -th tone is centered at f_c, having only a small offset, and constant over transmitted symbols.
- If *N* is even, both $N/2$ and [(*N* / 2) + 1] -th lines are equally spaced from f_c, having only slight offset and constant over transmitted symbols.

Based on the assumptions above, the sampled received signal at the output of each *n*-th coherent receiver can be represented as

$$u_n(t) = \left[\sum_{t=-1/2T_s}^{1/2T_s} s(t) h_{Tx}(t) h_{Rx,n}(t) \right] \times \quad e^{j2\pi\left(\Delta f_n T_s t + \varphi_s(t) + \varphi_{LO}(t)\right)}, \tag{3.7}$$

Then, the overall output signal $\hat{U}(f)$ can be reconstructed by merging all the signal tributaries in the digital domain. This can be achieved by numerically shifting each of the signal slice frequencies by Δf_n before performing a linear superposition and equalization of all these mixing products (see Section 3.3.3 for reconstruction DSP details). Each frequency-shifted slice can be written in the frequency domain as:

$$\hat{U}_n(f - \Delta f_n) = F^{-1}\left\{u_n(t) \cdot (j2\pi\Delta f_n)\right\}, \tag{3.8}$$

where the $F^{-1}\{\cdot\}$ term is the inverse Fourier transform operation. Assuming amplitude and phase matching on all slices, the recovered 'stitched' signal can be written as follows:

$$\hat{U}_n(f) = \sum_{n=1}^{N} \hat{U}_n\left(f - \Delta f_n\right). \tag{3.9}$$

Using the principles outlined above, the parallel coherent detection approach can be implemented by employing *N*-LO lines within the bandwidth of the signal spectrum. As the number of slices *N* increases, the bandwidth requirement for each receiver branch is reduced by a factor of *N*. However, signal splitting introduces a power loss of factor N, leading to degradation of the SNR. While a power splitter may provide significant power loss compared to an arrayed waveguide grating if *N* is large, for the modest degrees of splitting motivated here, $N=2$ or 4, the loss is in principle a maximum of 6 dB (for $N=4$). This is only 1 dB higher than the minimum insertion loss values typically achieved with arrayed waveguide gratings, whilst the splitter is much simpler and compact to implement. The stitching process can be carried out in DSP, with the complexity of this operation scaling linearly with *N*. Based on the modest value of *N* the author motivates in this work ($N=2$ or 4), the number of additional steps is minimal and only minimally adds to the overall complexity of the DSP, which is dominated by the conventional coherent signal recovery steps [64].

3.3 Receiver Architecture

In this section, the author presents the key components required for spectral slicing detection. The proposed receiver is centered around these three main components.

i. an optical frequency comb,

ii. an array of front-end coherent receivers (90° optical hybrid, BPD, TIA, and ADC), and

iii. a slice waveform reconstruction DSP.

3.3.1 Optical Frequency Comb

The optical frequency comb (OFC) is a type of laser that emits light across a wide range of frequencies, creating a series of peaks with uniformly spaced in frequency, resembling the teeth of a comb. Each peak, also known as a line or tone, is phase-correlated with the others. In the context of the SSRx, each of these spectral lines is used as an LO. By mixing these lines with different parts of the modulated optical signal spectrum, narrow bandwidth signals are generated, in line with the bandwidth restrictions of the low-speed components in the coherent receiver's front-end. A common method for generating a comb signal in laboratory settings is by employing an electro-optic (EO) modulator. This approach offers the flexibility to tune properties such as the number of lines and comb spacing which is advantageous for proof-of-concept demonstrations.

The configuration of the OFC based on the EO modulator is illustrated in Figure 3.2(a). In this setup, an ECL with a center wavelength of 1548.13 nm and a linewidth of 60 kHz is used to transmit a CW signal. This lightwave is then modulated by a single-drive MZM using an RF signal generator to create multiple sidebands. Proper adjustment of the RF signal amplitude, frequency, and bias control allow for generating two tones with the desired comb spacing at the center frequency of the ECL. Figure 3.2(c) demonstrates the generation of the comb signal when the MZM is biased at the null point, suppressing the optical carrier frequency and creating even-order sideband lines separated by the free spectral range (FSR) frequency f_{FSR}, equal to two times the RF signal generator frequency f_R. The author employed this bias configuration throughout this work to generate the comb signal. Similarly, biasing the MZM at the maximum point generates comb lines with odd-order sidebands. The number of lines generated

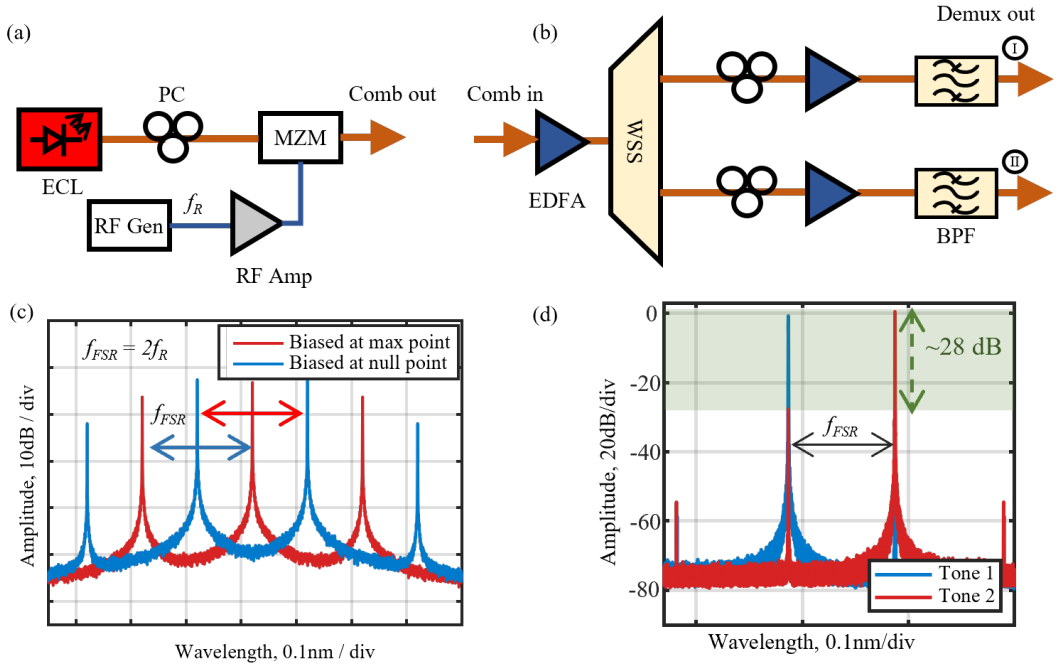


Figure 3.2: (a) Experimental setup of an optical frequency comb based on a single-drive MZM. RF Gen.: RF Source Generator. (b) The experimental setup for comb signal demultiplexing using the wavelength selective switch based on liquid crystal on silicon technology. (c) The optical spectrum of the OFC was captured using an optical spectrum analyzer (OSA) with resolution bandwidth of 20 MHz. The two traces represent two different bias settings of the EO-modulator to generate the frequency comb. (d) The optical spectrum of the comb after demultiplexing. The comb line suppression ratio is measured based on the difference between the peak power of the demultiplexed comb line with the adjacent lines.

corresponds to the amplitude of the RF signal driving the MZM. In this case, only two tones are required for an SSRx with N=2.

After generating the frequency comb, the signal was optically amplified using an EDFA to compensate for the losses from the wavelength selective switch (WSS) which is used for comb demultiplexing as shown in Figure 3.2(b). The WSS, based on a liquid crystal on silicon technology (Waveshaper 4000s), enables channel demultiplexing with a minimum 10 GHz passband bandwidth. However, this limited passband resolution may result in adjacent tone leakage, particularly for dense f_{FSR}. The impact of this effect on the performance of SSRx will be further analyzed in the next chapter 4. Then, each tone is amplified once again to a high output power per peak line. This high-intensity light can greatly aid in achieving high receiver sensitivity when it serves as a LO. Subsequently, an optical bandpass filter (BPF) with a bandwidth of 0.2 nm is used to reduce the

ASE noise in the tone signal. The spectra of both demultiplexed tones are shown in Figure 3.2(d), with the suppression of the adjacent tone measured at around 28 dB.

3.3.2 Array of Coherent Receiver

In this work, the proposed receiver high-level schematic resembles the one in the previous chapter, but with the inclusion of two receiver units for $N=2$ operation. These units were configured in parallel, as depicted in Figure 3.3. Following the signal splitting using an optical power splitter, each signal is directed to a separate ICR to mix with the demultiplexed comb line. The optical splitter was chosen due to its simple design and only involves a moderate number of splits. The limited bandwidth of the front-end receiver means that only a portion of the entire signal can be captured, resulting in sliced signal spectra.

Delays in the split signal may occur due to differing path lengths between the splitter and receivers. Furthermore, there may be path mismatches in the RF cabling between the receiver front ends and the oscilloscopes. To address these issues, a deskew calibration is necessary to compensate for time-delay differences in the sliced signals. The calibration process is detailed in Figure 3.4(a). This deskew can be achieved by using cross-correlation to obtain the time-delay differences in complex signals between the two receivers. Assuming that both oscilloscope channels are time synchronized and capture the same signals, the time delay can be computed by correlating these two waveforms.

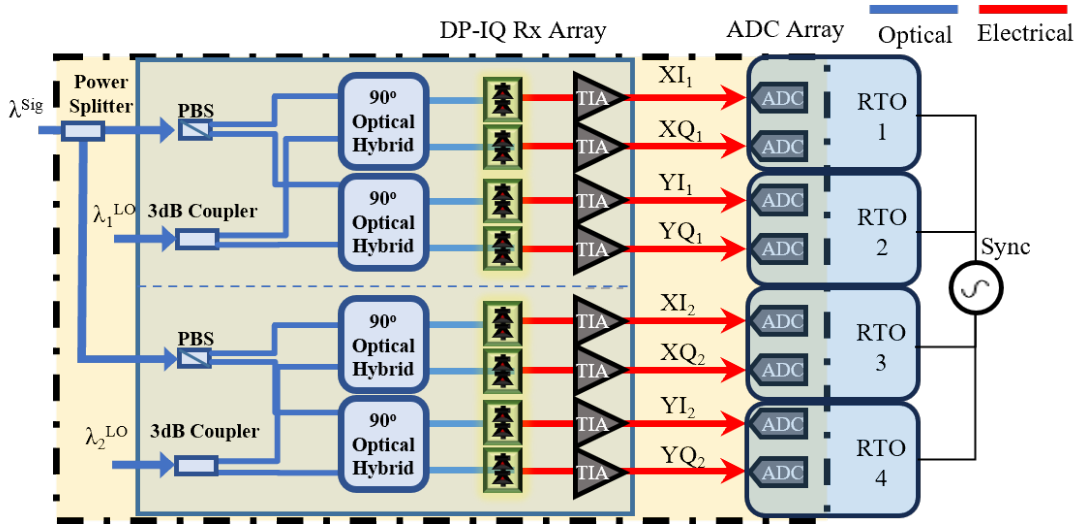


Figure 3.3: Schematic of two DP–I-Q coherent receivers configured in parallel, generating $XI_n(t)$, $XQ_n(t)$, $YI_n(t)$ and $YQ_n(t)$ components to the oscilloscopes.

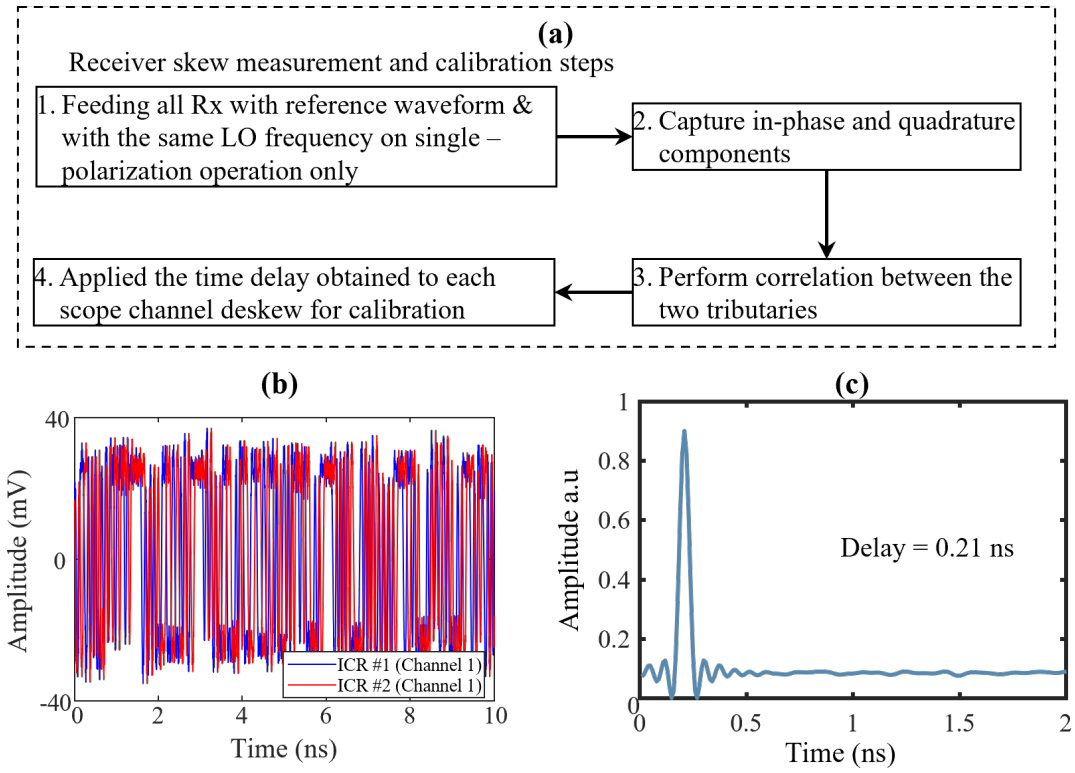


Figure 3.4: (a) Block diagram of processing steps performed to calibrate timing delay between receiver channels. (b) Captured experimental waveforms of channel 1 (in-phase tributary) from the two separate coherent receivers. (c) Cross-correlation response of the captured waveforms between coherent receivers in each lane.

In Figure 3.4(b), the waveforms captured from channel 1 (in-phase) of each coherent receiver in the SSRx (N=2) are depicted. Figure 3.4(c) illustrates the cross-correlation response of these two waveforms, with the correlation peak indicating the time delay value between the two receivers. The same procedure can be applied to channel 2 (quadrature), yielding the same time delay, as the I-Q skew between the two ICR designs is almost similar. These values can then be applied in the skew function in the acquisition (scope) channels to compensate for the time delays between the two complex slices. It is worth noting that this calibration is a one-time process, as the group delay will remain constant throughout the measurements.

3.3.3 Reconstruction Digital Signal Processing

Figure 3.5(a) illustrates the DSP blocks to synthesize slice signals with the scalability of N. For simplicity, the author describes the DSP reconstruction for the case N=2, which consists of two synchronized coherent receivers. Each receiver

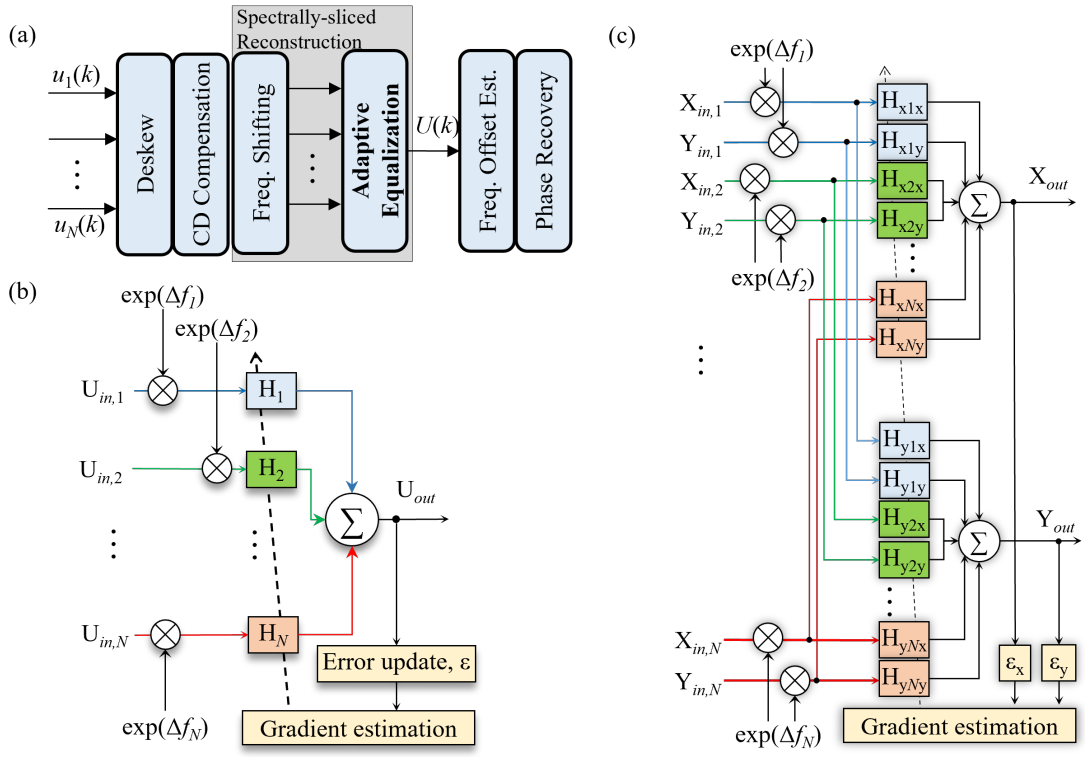


Figure 3.5: (a) Functional blocks in a spectrally sliced receiver DSP. The schematic of reconstruction DSP is based on FIR filters for (b) single-polarization, and (c) dual-polarization modulation.

generates a slice signal which is then sampled by the ADCs.

In order to shift each digitized signal to a frequency Δf_n which derived from Equation 3.8, a precise knowledge of f_{FSR} is crucial to determine this frequency-shifting (Δf_n) value, as it directly affects the reconstruction performance. The precise Δf_n can be obtained using two methods. The first method involves calculating the autocorrelation of the down-converted spectral slices to detect a peak close to the expected f_{FSR}, providing the precise value of f_{FSR}. The second method involves using heterodyne detection of the two separated comb lines, resulting in a beat tone at a frequency value, which also corresponds to the f_{FSR} value of the comb. However, it is important to note that both methods are limited by the resolution of the instrument (e.g. oscilloscope sampling rate or electrical spectral analyzer resolution bandwidth) to obtain the measurement down to the 1 Hz scale. Although this high level of accuracy can be achieved, the receiver sensitivity tolerance to the frequency-shift was investigated and presented in Section 3.5. The resulting frequency shifts can then be implemented in the time domain, where each slice is shifted by f_n.

Finally, the recombined slice output can be generated using the adaptive equalization processing structure with multiple inputs, as shown in Figures 3.5(b) and (c). These reconstruction algorithms are generally similar (in concept) to the conventional adaptive equalization described in Section 2.3.3. The filter output, $U_{out} = [X_{out}; Y_{out}]$ can be calculated as:

$$U_{out}(k) = \sum_{n=1}^{N} H_n^H(k) \left[u_{in,n}(k) exp(\Delta f_n) \right], \tag{3.10}$$

where superscript $(\cdot)^H$ denotes the conjugate transpose, u_{in} is the input slice sequence of the filter with a sampling index k, and H is the FIR filter. Similarly, for the dual-polarization operation, complex outputs X and Y can be generated considering $u_{in} = [X_{in}; Y_{in}]$, while $H_n = \left[H_{xnx} H_{xny}; H_{ynx} H_{yny} \right]$. The filter coefficients can be updated using either the radius-directed algorithm or the least mean square with direct decision, as shown in Equations 2.26 and 2.27, respectively. In the case of N=2, the filter tap weights can be updated as:

$$\begin{aligned}
H_{x1x}(n+1) &= H_{x1x}(n) + \mu \varepsilon_x X_{in,1} X_{out}^*(n), \\
H_{y1x}(n+1) &= H_{y1x}(n) + \mu \varepsilon_x X_{in,1} Y_{out}^*(n), \\
H_{x1y}(n+1) &= H_{x1y}(n) + \mu \varepsilon_y Y_{in,1} X_{out}^*(n), \\
H_{y1y}(n+1) &= H_{y1y}(n) + \mu \varepsilon_y Y_{in,1} Y_{out}^*(n).
\end{aligned} \tag{3.11}$$

$$\begin{aligned}
H_{x2x}(n+1) &= H_{x2x}(n) + \mu \varepsilon_x X_{in,2} X_{out}^*(n), \\
H_{y2x}(n+1) &= H_{y2x}(n) + \mu \varepsilon_x X_{in,2} Y_{out}^*(n), \\
H_{x2y}(n+1) &= H_{x2y}(n) + \mu \varepsilon_y Y_{in,2} X_{out}^*(n), \\
H_{y2y}(n+1) &= H_{y2y}(n) + \mu \varepsilon_y Y_{in,2} Y_{out}^*(n).
\end{aligned}$$

In principle, the entire spectrum of the received signal could be recovered by combining the left side of the spectrum from slice 1 with the right side of the spectrum from slice 2, in the case of N=2. Performing this reconstruction with equalization processing allows the amplitude and phase alignment between the spectral slices to be compensated for. The performance of this reconstruction DSP will be analyzed in the next section. After the reconstruction block, the frequency offset, and phase noise are compensated using the DSP described in Section 2.3.4 before signal decoding assuming that the comb spacing is fixed and has excellent phase correlation.

3.4 Numerical Simulation Model

3.4.1 Simulation Flow

To validate the feasibility of the proposed SSRx, system-level simulations were performed using MATLAB. The modeling blocks and procedures are similar to those used in Chapter 2, with parameters listed in Table 2.1, except for the new detection blocks. Figure 3.6 illustrates the block diagram of the processing steps required to simulate the spectrally sliced receiver system (colored in green) for various number operations N.

First, both QPSK and 16QAM signals operating at 25 Gbaud were pulse-shaped with a 0.1 roll-off factor, resulting in approximately 25 GHz optical signal bandwidth. Subsequently, N-phase correlated tones with frequency spacing obtained from Section 3.2 were generated for N-independent I-Q receptions. These values can be found in Table 3.1 for different N operations. To demonstrate low-bandwidth operation, the bandwidth of each receiver is determined based on N, as specified in Table 3.1.

The DSP chain shown in Figure 3.6 was used to post-process the digitized signals, leading to the recombination of the slices and the recovery of the data. The adaptive reconstruction equalization comprises N and $4N$ complex 15-tap FIR filters for single- and dual-polarization modulations, respectively. The equalizer's FIR filter coefficients were estimated using the radius-directed algorithm before performing the frequency offset estimation and carrier phase recovery. Finally,

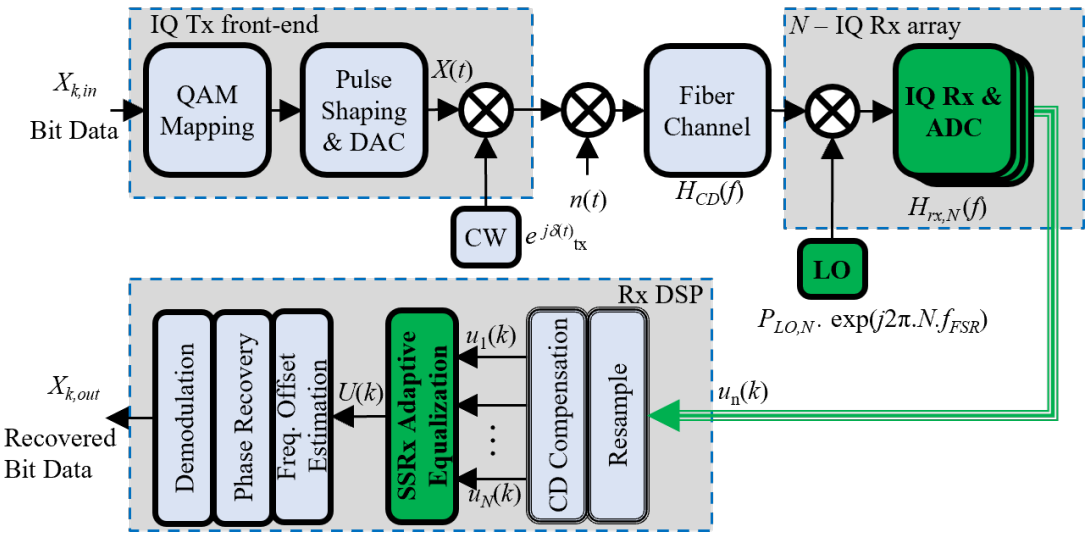


Figure 3.6: Block diagram of an SSRx simulation system setup.

Table 3.1: Simulation of SSRx system parameters

Slicing Number, *N*	**Rx Front-End Bandwidth (*GHz*)**	**f_{FSR} (*GHz*)**
2	*6.25*	12.5
3	*4.167*	8.33
4	*3.125*	6.25
5	*2.5*	5

BERs were measured using direct error counting.

3.4.2 25 Gbaud QPSK performance with the scaling of slicing number

The analysis began with examining the receiver sensitivity performance in a BtB link with high LO power (P_{LO}=+15dBm). In this scenario, each comb line would carry a power of +15 dBm for all N operations. Figure 3.7 shows the sensitivity performance of the proposed receiver. The result shows a minimal sensitivity penalty (at the FEC limit) between the conventional coherent receiver and the proposed SSRx. Note that for conventional coherent case (ICR), the front-end bandwidth is set to 12.5 GHz. Even with an increase in the slicing number to N=5, the impact remains below 0.5 dB for both SP-QPSK and DP-QPSK modulation formats despite the 3-dB bandwidth of front-end receivers is

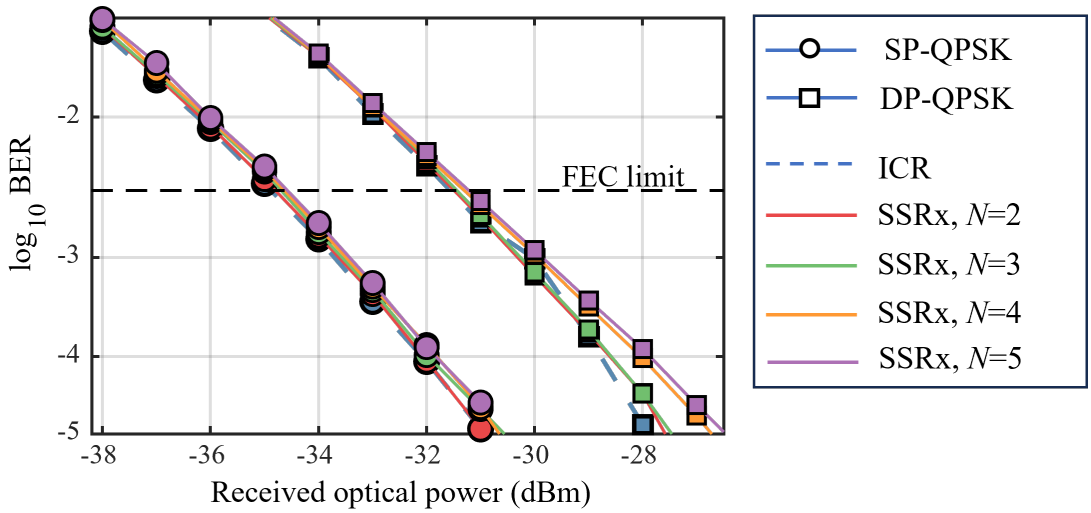


Figure 3.7: Simulated BER versus ROP for 50 Gb/s SP-QPSK and 100 Gb/s DP-QPSK. Solid lines refer to a spectral slicing receiver with different number of slicing operation N, and the dashed lines refer to a conventional coherent receiver, ICR.

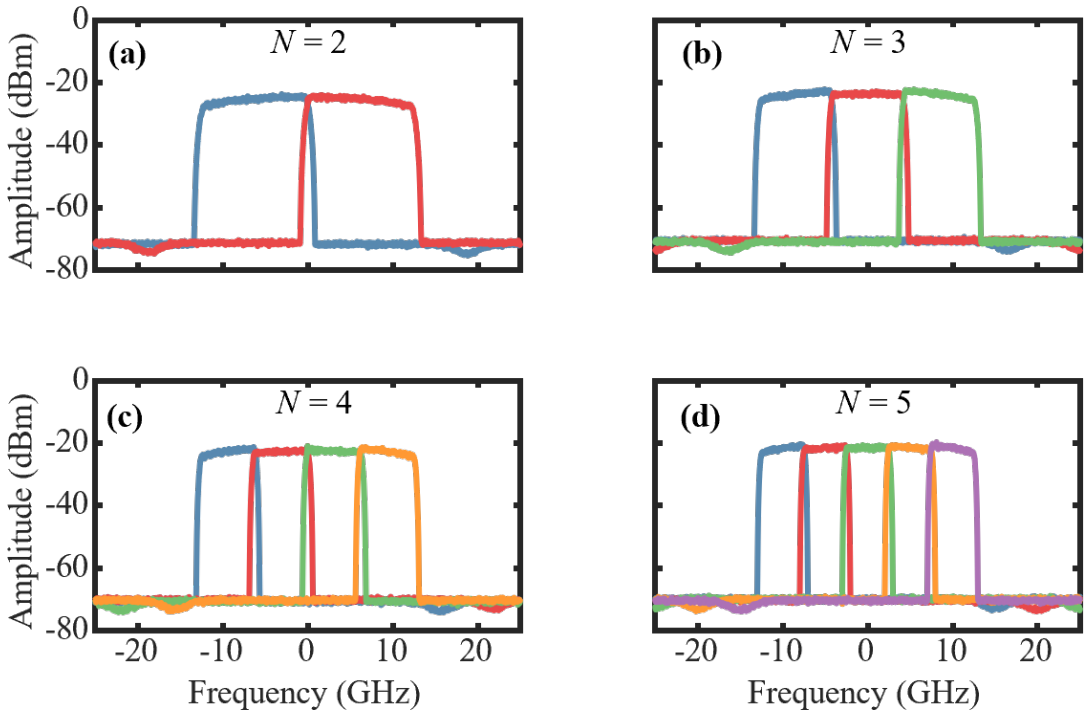


Figure 3.8: Visualisation of the stitching process of the frequency-shifted signal sliced on a 25 Gbaud signal. (a) N=2, (b) N=3, (c) N=4, and (d) N=5.

reduced by a factor of N. This indicates that SSRx detection can achieve high receiver sensitivity without compromising sensitivity performance compared to a conventional coherent receiver when the baud rate of the signal is the same for both detection schemes.

In Figure 3.8, the functional demonstration illustrates the slicing spectra of the tributaries produced by coherent receivers based on the number of slices, denoted as N. As explained in Section 3.3.3, each slice signal undergoes a frequency shift to align with its respective comb line frequency before being coherently combined using reconstruction DSP. It is important to note that an increase in N results in the need for more frequency-shifting operations. However, for an odd number of N operations, the middle slice does not require a shift operation. In the subsequent experimental demonstration in this chapter, only N=2 is performed due to the limited receiver and equipment resources available.

3.4.3 Performance of Reconstruction Equalization

Next, the impact on the receiver's performance of non-ideal slice parameters, such as a phase mismatch, was investigated. When the received signal is split into the receiver array, there may be phase imbalances between the receivers due

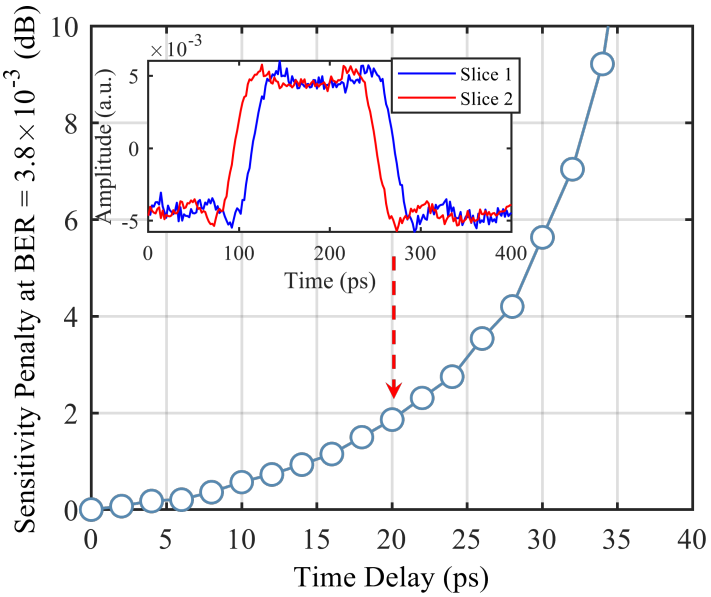


Figure 3.9: Receiver sensitivity measured as a function of phase variance for SSRx with N=2 scheme. Inset: Optical signal waveforms in the time domain where slice 2 was delayed by 20 ps compared to slice 1.

to path mismatches between the slice channels. This requires equalization in the reconstruction DSP to compensate for the phase imbalances in the channel response. The author simulated phase variations in a dual-spectral-slice (N=2) detection, where the delay between the first and second slices was shifted in 2 ps steps.

Figure 3.9 shows the sensitivity penalties induced by the simulated phase variations between the slices with a low equalization filter size (number of taps = 3). The higher sensitivity penalty becomes more pronounced as the skew increases due to the accumulated phase mismatches between the slices. An approximate 2 dB sensitivity penalty was observed at 20 ps of delay mismatch between the slice optical waveforms in the N=2 scheme. The inset in Figure 3.9 shows the optical waveforms that were sent to the first and second receivers with a skew of 20 ps.

Subsequently, an analysis of the adaptive filter size configuration for varied N operation was studied in the same phase mismatch environment between the slices for different equalization filter sizes. This analysis is crucial for optimizing the reconstruction DSP for efficient slice stitching in the SSRx scheme. The receiver sensitivity performances are shown in Figure 3.10 for varied filter sizes at different skews between the slice 1 and slice 2 signals. In this analysis, the adaptive filter size in the reconstruction algorithm varied from 3 to 21 taps. As

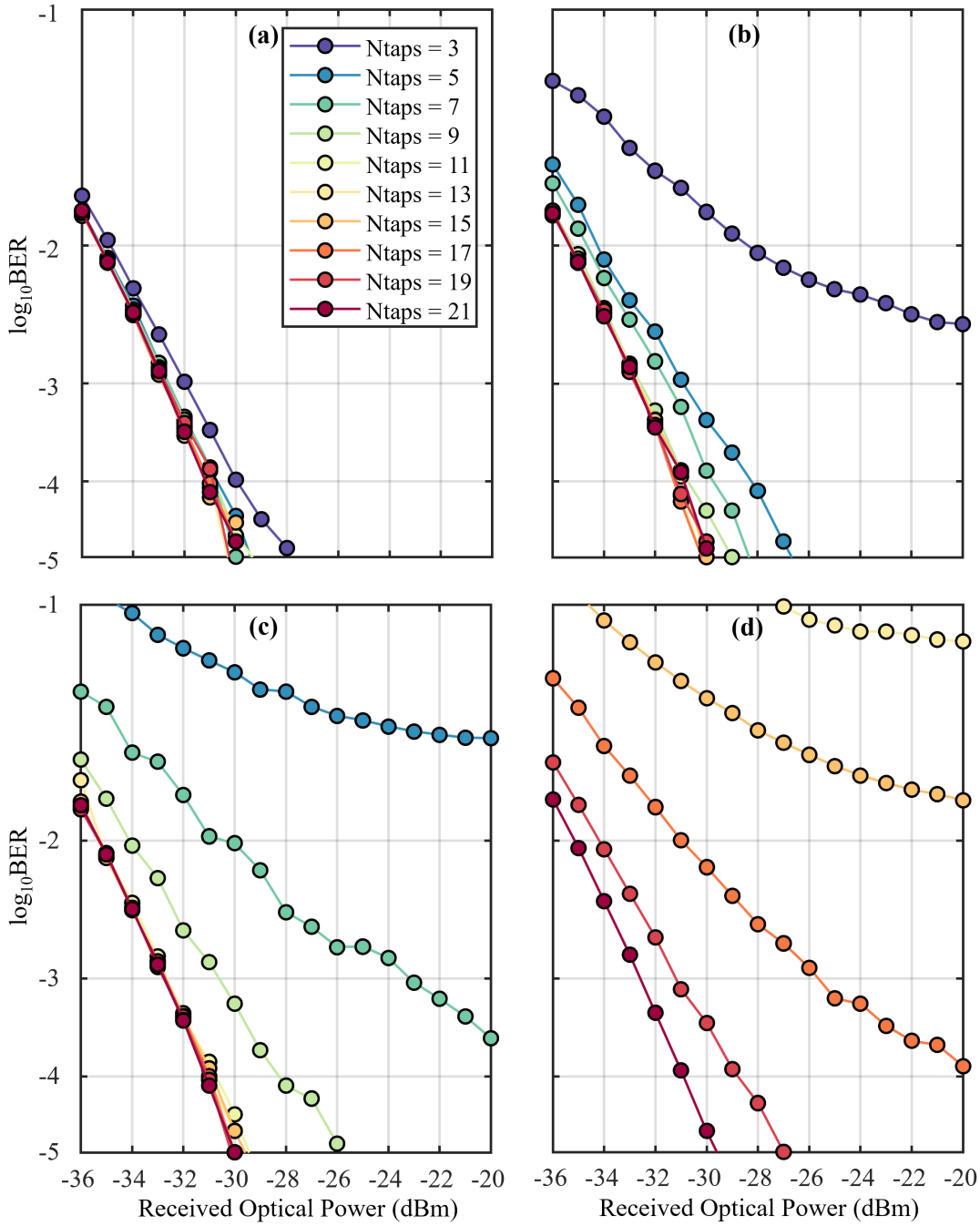


Figure 3.10: The performance of BER versus ROP with (a) 0 ps, (b) 50 ps, (c) 100 ps, and (d) 150 ps delay between slice 1 and slice 2.

the skew between the slices becomes larger, there is an associated degradation in the sensitivity penalty with the same filter size. However, increasing the filter size in the reconstruction DSP can enhance the ability to coherently recombine the slices at large skews, thereby improving the receiver sensitivity.

3.4.4 Bandwidth and Comb Spacing Restrictions

The FSR of an OFC can be directly related to the frequency spacing between the center of slice signals. For instance, in N=2, the frequency spacing between the two slice signals at their center frequency is equal to f_{FSR}. In the ideal scenario, the FSR of the comb should be determined based on the optical signal bandwidth and N. Therefore, it is important to investigate the receiver sensitivity tolerance to FSR for a fixed signal bandwidth.

The sensitivity penalty performance, corresponding to the FSR, is shown in Figure 3.11. In an ideal scenario, if the frequency spacing between the slices is 12.5 GHz, the recovery performance becomes optimal when the receiver bandwidth exceeds 6.25 GHz to ensure that each receiver has sufficient bandwidth to capture the entire slice spectrum, thus minimizing the possibility of a 'gap' between the slice spectra or missing the edge of the signal spectra; which would otherwise lead to a degraded reconstructed signal performance. For example, it can be observed that the sensitivity penalty increases when the receiver bandwidths are reduced below 6.4 GHz. There is no sensitivity penalty when there is extra bandwidth in the receiver and the spectral overlap region between the slices is useful as it conveys phase offset information which is used in the signal reconstruction

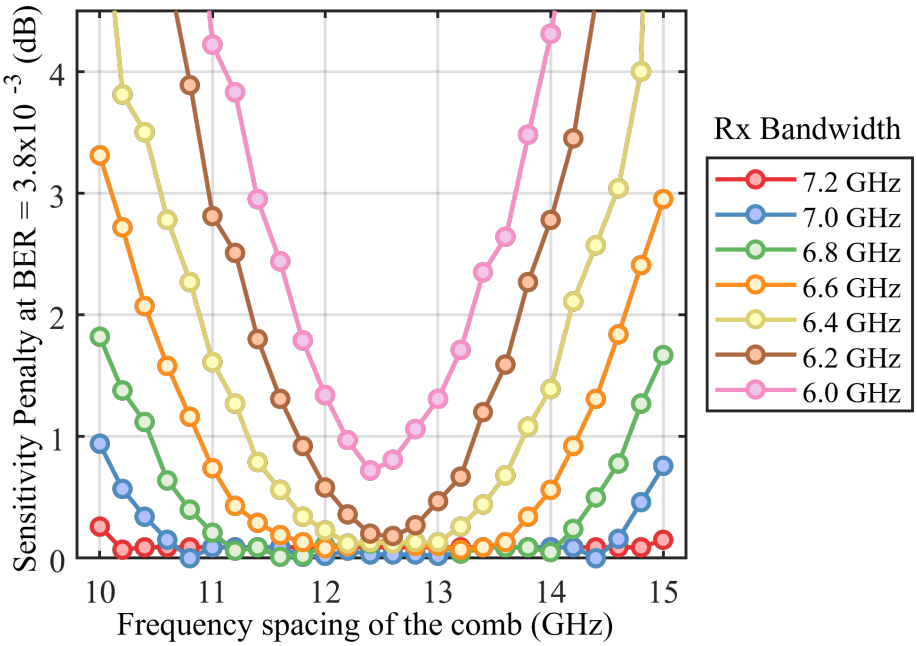


Figure 3.11: Receiver sensitivity penalty performance in 25 Gbaud QPSK signal transmission versus the frequency spacing of the comb with varied receiver's bandwidth.

processing.

Similar observations are made when the FSR is varied. When the frequency spacing deviates from the ideal 12.5 GHz, the receiver bandwidth requirement increases to capture the entire signal spectra of the signal. This is due to inadequate receiver bandwidth, which results in a 'gap' between the combined slices (in the case of frequency spacing >12.5 GHz) or a missed edge of the signal spectra (in the case of frequency spacing <12.5 GHz). Therefore, for N=2 at 25 Gbaud, an optimized FSR of the comb is at 12.5 GHz. Nevertheless, a small increase in Rx bandwidth from the minimum achievable bandwidth is a good practical trade-off to accommodate some variation in comb's FSR. For example, by increasing the bandwidth slightly from 6.25 to 6.4 GHz, $\pm$0.5 GHz variation at 12.5 GHz FSR can be tolerated with negligible penalty, showing that the approach is flexible and can accommodate variations in FSR in real components.

3.4.5 Comments on the Complexity of SSRx

In addition to analyzing receiver performance, it is important to compare the complexity of the conventional coherent receiver with the proposed receiver using relevant cost metrics. Practical considerations on the complexity of the front-end (the number of components required) and the associated DSP for the N scaling are discussed below.

The front-end of a conventional coherent receiver for detecting a single polarization with a phase-diversity signal includes 1 optical hybrid, 2 BPDs, 2 TIAs, and 2 ADCs, For N=2 in the experimental setup, two receiver lanes are required, doubling the number of components, but halving the component bandwidth requirements as shown in Figure 3.12(a). As N increases, the total number of components increases linearly with N, and the bandwidths are reduced by a factor of $1/N$, as shown in Figure 3.12(b).

Regarding DSP complexity, the additional DSP comes in the reconstruction block, which stitches all the slices together through a linear superposition in a tap weight updating operation, and the frequency shifting for each slice can be performed (via multiplication operations) individually in the time domain. Consequently, the complexity scales linearly with N. Interestingly, for the modest number of slicing operations that the author motivates in this work (N=2 or 4), the additional number of operations for reconstruction processing is minimal compared to the overall complexity of conventional coherent DSP [65].

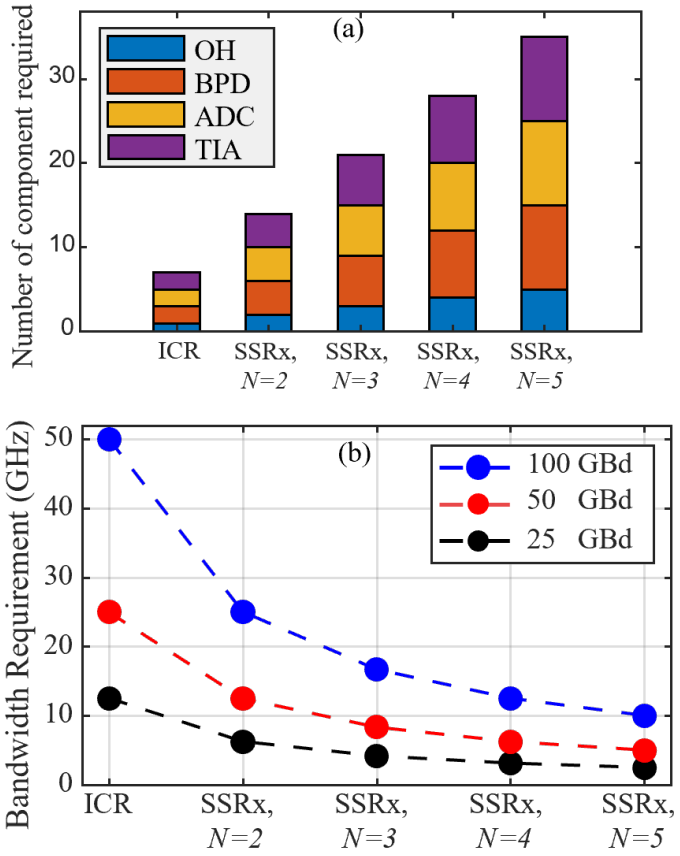


Figure 3.12: (a) The quantity of component required in the front-end receiver. (b) Receiver front-end bandwidth requirement.

For production, the optoelectronic bandwidth and speed requirements are one of the most significant factors contributing to the implementation cost of a PIC [48]. This tends to be supported by the observation that coherent transponders have evolved using the homodyne/intradyne detection configuration, which has (typically) half the bandwidth of comparable heterodyne schemes, despite the fact that the latter are significantly simpler in terms of the type and number of optical and optoelectronic components required for implementation. Similarly, in the proposed receiver scheme presented here, although the SSRx requires more components, due to its unique ability to capture a wideband signal with components whose electrical bandwidth can be reduced by a factor of N, it is therefore well suited for implementation on low-cost PIC platforms.

To assess the feasibility of the proposed detection scheme for achieving higher data rates, Figure 3.12(b) shows the optimal receiver bandwidth requirements for different baud rate operations. It can be seen that, in the context of the access network application the author considers, SSRx with N=2 and 4 would enable

the PON data rates to scale into the 100 Gbit/s and beyond regime using 25 or 50 Gbaud modulation rates, while continuing to leverage low-cost 10G-class components, which are widely deployed today. This philosophy mirrors that used in recent 25G and 50G PON standards development, where more complex modulation formats and DSP have been considered in order to enable the use of older generation, lower bandwidth optoelectronic components that have already been cost reduced through volume manufacture and widespread deployment. As will be highlighted in Section 3.6, some of the unique features of PON upstream channels further motivate this need for bandwidth reduction.

3.5 50 & 100 Gb/s Coherent Link Experiment Utilizing an SSRx

3.5.1 Experimental Setup

An experimental setup was designed to demonstrate the feasibility of an SSRx as shown in Figure 3.13(a). The setup used transmitter and link configurations which are similar to those demonstrated in Chapter 2. The transmitter consisted of an ECL operating at 1549.0 nm and modulated with 25 Gbaud QPSK signals, resulting in an overall 50 and 100 Gb/s for single- and dual-polarization operation. The transmitted signal was captured, and the spectrum is displayed in Figure 3.13(b). This analysis considered receiver sensitivity performance, so a VOA was used to adjust the ROP. The simplest form of SSRx (N=2) was employed which is based on two-nested coherent receiver configurations (2×Fujitsu-FIM24902) for both polarization cases.

At the receiver side, first, the signal was split equally by a 3-dB coupler and the ROP measurements were taken after the optical splitting. The split signals were then mixed with LOs derived from the de-multiplexed comb lines and detected by two separate integrated coherent receivers before being sampled by synchronized oscilloscopes operating at 50 GSa/s. The alignment of the two comb tones was adjusted so that the center frequency of the signal was measured to be in the center between the two comb tones. Figure 3.13(c) shows the signal spectrum with the corresponding comb tone spectra. Here, the comb lines were generated using the EO-comb scheme with 12.5 GHz spacing and demultiplexed by the WSS. As the split signal path can suffer a constant delay between the two receivers due to different optical paths, the timing deskew operations (as

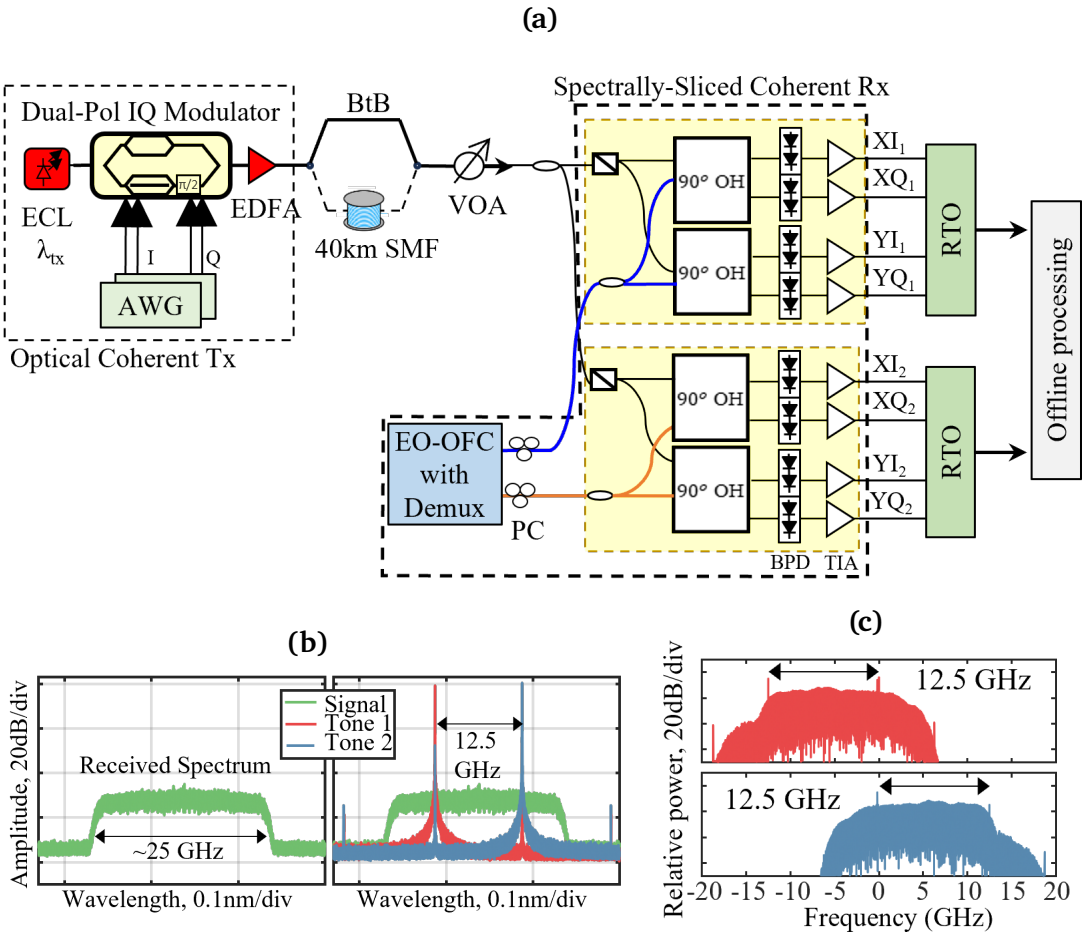


Figure 3.13: (a) Experimental setup for proof-of-concept of 25 Gbaud signal transmission. Spectrally-sliced coherent receiver diagram with two slicing operations (N=2) on two different modulation schemes: SP-QPSK and DP-QPSK. The spectra in (b) illustrate the comb tones aligned to the signal spectrum, subsequently reduced into two smaller spectra, each known as a 'slice', shown in (c).

described in Figure 3.4) were performed on each sampled waveform. Finally, the digitized waveforms were captured and processed offline.

The commercial receivers used in the experiments have wide analogue bandwidth (>40 GHz) specifications designed for 400 Gbit/s operation. To test and demonstrate the potential of the SSRx scheme to enable the use of much lower Rx front-end bandwidths, the author emulates this scenario by applying digital filtering with a 3dB bandwidth of 6.25 GHz in post-processing on the sampled waveforms. The electrical spectra for both slices are shown in Figure 3.13(d). After sampling and low-pass filtering, the dispersion was compensated for by the 7-tap static equalizer employed for each slice signal. Then, both slices were stitched together using a modified MIMO for reconstruction and equalization

described in Section 3.3.3, which consists of four and eight complex 15-tap FIR filters for single- and dual- polarization operations, respectively. These FIR filter coefficients were updated using the radius-directed algorithm, which was initialized by a training sequence and then switched to the blind mode. Next, the frequency offset was estimated and compensated for before carrier phase recovery based on the Viterbi-Viterbi algorithm to eliminate phase noise from the reconstructed signal. Finally, the output signal was demodulated and the BERs were evaluated using direct error counting.

3.5.2 Receiver Performance with Comb Power

The first step in analyzing the experimental demonstration of SSRx involved studying the receiver sensitivity performance in both BtB and over the 40 km fiber link, which are the main test cases used in this thesis. The author compared the ROP curves for different comb tone powers using the SP-QPSK modulation format, as depicted in Figure 3.14(a). The measurements revealed that the received power at the FEC limit is nearly identical for BtB and 40 km of fiber transmission, indicating that chromatic dispersion impairments can be compensated for in each subchannel before the stitching processes. By operating the OFC to generate high comb line power (approximately +10 dBm), the proposed SSRx has the potential to recover signals at a high receiver sensitivity of −36.4 dBm over a 40 km fiber link.

To investigate the effectiveness of the proposed SSRx architecture, the author compared the BER performance of the SSRx with the conventional intradyne (ICR) detection scheme. Both receiver schemes were compared with similar parameters, such as using dual-polarization operation and similar LO power. Figure 3.14(b), shows that the proposed SSRx has achieved a receiver sensitivity performance similar to the ICR scheme. The comparison of different LO power operations from 0 to 10 dBm also demonstrated the similarity in sensitivity trends. It is worth noting that the ICR utilizes a front-end bandwidth of 12.5 GHz while the SSRx only uses a 6.25 GHz bandwidth (for each front-end). This directly confirms and demonstrates the SSRx scheme's capability to reduce the front-end Rx bandwidth requirement for detecting a wideband optical signal without compromising the sensitivity compared to the conventional coherent receiver.

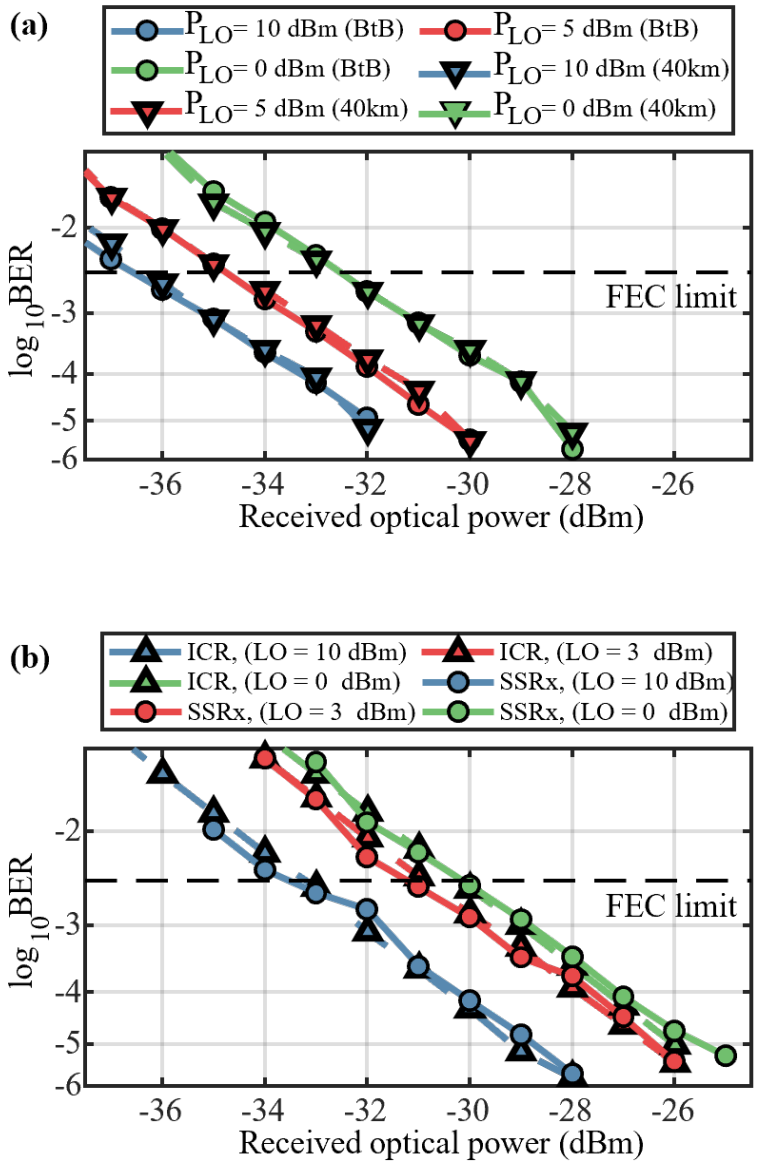


Figure 3.14: (a) Experimental results of BER performance versus ROP for the different optical power per comb line. (a) 50 Gb/s SP-QPSK comparing the SSRx performance over BtB and 40 km fiber link. (b) 100 Gb/s DP-QPSK over 40 km fiber comparing the ICR with SSRx detection scheme.

3.5.3 Estimation of the Free Spectral Range of the LO Comb

As shown by Equation 3.8, knowledge of the comb's FSR is required in post-processing, as the signal slices must be frequency-shifted back to their respective frequency position before the stitching process. This section investigates the extent of frequency-shifting tolerance in the reconstruction DSP performance when the slice is shifted away from the ideal frequencies based on the comb's FSR. The resulting receiver sensitivity penalty, relative to the optimal frequency

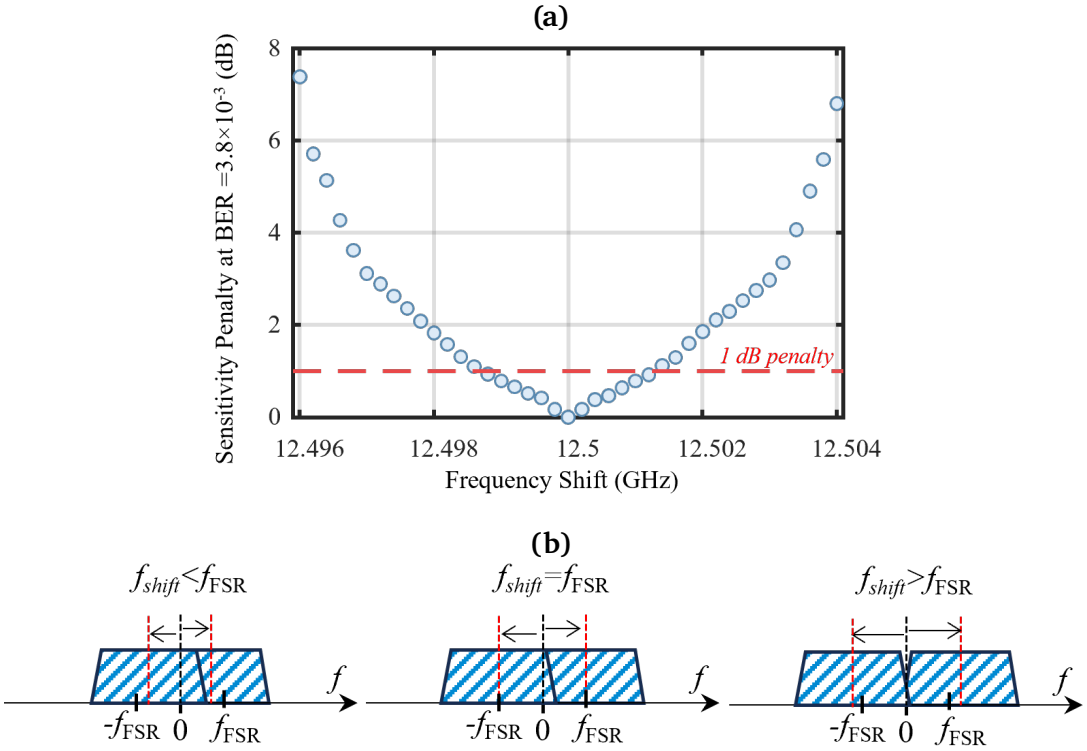


Figure 3.15: (a) Receiver sensitivity measured as a function of frequency shift for signal reconstruction. (b) Illustration of the impacts of frequency shift on the reconstructed spectra.

shift of 12.5 GHz, is shown in Figure 3.15(a). The quality of the recovered signal degraded to almost 8 dB at ±4 MHz offsets from the ideal 12.5 GHz frequency. A minimum frequency offset of around 1.2 MHz is required relative to 12.5 GHz to achieve a <1-dB penalty. This margin can then be used to define the analyzer's resolution bandwidth requirement to measure the FSR's precise value.

In principle, the FSR of an optical frequency comb can be measured directly using an OSA; however, the finest resolution of a commercial OSA is 0.1 nm. This may underestimate the exact FSR value. An ESA can be used to estimate the FSR accurately as it can have an excellent spectral resolution of up to 1 Hz. The measurement setup is illustrated in Figure 3.16(a). This measurement technique is based on self-heterodyne, where the two comb lines are demultiplexed by a WSS and mixed together through a coupler, then detected by a high-bandwidth photodetector (∼40 GHz). The power spectral density of the beat signal is measured, where the peak corresponds to the frequency difference between the two comb lines, which is equivalent to the FSR of the comb. Figure 3.16(b) shows an example of the electrical spectrum captured using an ESA with a resolution bandwidth of 3 Hz. The measured FSR is approximately 10.2 kHz offset away

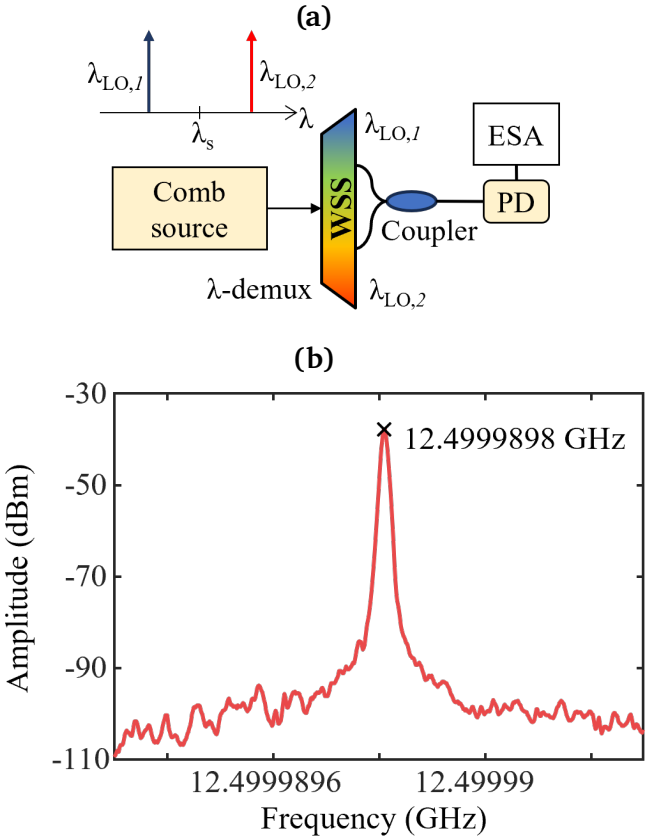


Figure 3.16: (a) Setup for measuring the free spectral range of the comb. (b) The spectra of the beating tone captured by an ESA operating at the resolution bandwidth of 3 Hz.

from the ideal 12.5 GHz, resulting in an almost negligible sensitivity penalty when the slices are frequency-shifted by approximately 6.25 GHz. This small offset measured is due to uncalibrated frequency signal generator to drive the modulator to generate a frequency comb signal. Similarly, this measurement can be performed using a coherent receiver for the mixing of the two comb lines, and the FSR can be estimated using the frequency offset estimation in DSP.

3.5.4 Optimization of Reconstruction Equalizer

In the previous simulation work, the author focused on studying the impact of the equalizer size on SSRx performance. In this experimental work, the reconstruction equalizer was trained for a long training sequence (2^{13} symbols) to avoid any penalty due to insufficient training. The adaptive filter size was configured with 21 taps to achieve optimal signal reconstruction and recovery.

Figure 3.17 shows the measured receiver sensitivity penalty with varying adap-

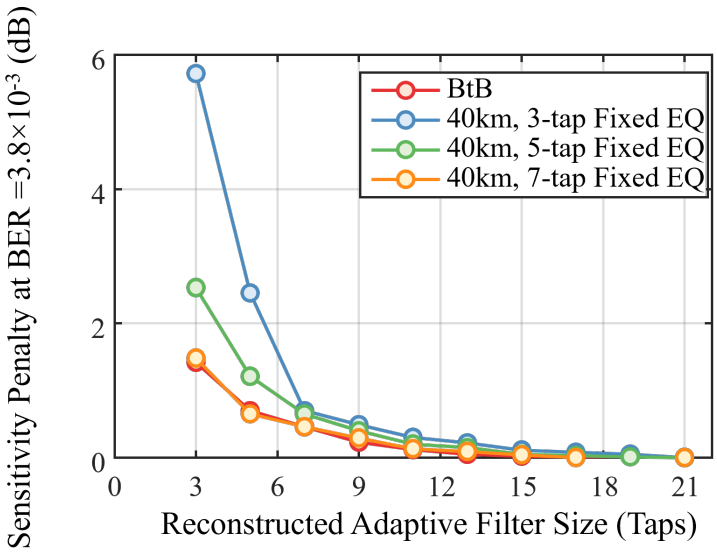


Figure 3.17: Receiver sensitivity penalty as a function of the number of taps required for the reconstruction adaptive equalizer in BtB and over 40km fiber link.

tive filter sizes in DSP reconstruction. When transmitting the signal through a BtB link and using 3 or 5 taps in the reconstruction DSP, the receiver sensitivity penalty was found to be greater than 0.5 dB. However, as the filter size increased, the penalty was reduced and became negligible with a tap size of more than 15 taps. In the 40 km fiber transmission case, the receiver sensitivity performance degraded with a smaller tap size in static equalization due to incomplete compensation for chromatic dispersion. However, using a larger tap size ($\geq$7) in the adaptive filter, the receiver sensitivity penalty was negligible for both the BtB and the 40 km link. This indicates that the optimization settings for DSP reconstruction were effective in fully compensating for chromatic dispersion in the 40 km fiber while recovering the signal.

3.6 Performance Assessment of SSRx in PON

3.6.1 Addressing Burst-Mode PON Challenges

The previous experiments were conducted in continuous transmission mode, which is analogous to the downstream link in a PON scenario, which is the communication from the OLT at the central office to the ONU at the subscriber premises. However, it is widely accepted that the most challenging aspect of PON technology development comes from the upstream link, which operates in burst mode using a Time Division Multiple Access (TDMA) protocol to share the available bandwidth between the subscribers and which must support a high

variability in the burst-to-burst signal powers at the receiver (dynamic range of approximately 20 dB) due to branch-to-branch variations in splitter and fiber loss and ONU launch powers.

This necessitates a burst-mode receiver (BMRx) in the OLT that can quickly adjust its gain within a few hundred nanoseconds at the beginning of each signal on a burst-by-burst basis. This becomes increasingly difficult as the bandwidth and linearity requirements increase, making the spectral slicing approach potentially particularly valuable in this context. For example, 10Gb/s BMRx technology exists and is commercially used in standardized solutions such as XGS-PON, which is currently being widely deployed in Ireland under the National Broadband Ireland (NBI) initiative [66]. In contrast, 25Gbaud class BMRx prototypes have only recently begun to appear in the research literature [67] and it has been shown that it is extremely challenging to simultaneously maintain the required bandwidths, dynamic range, and linearity at these and higher bit rates. If the low-cost PIC technology required to enable spectral slicing solutions can be developed, the resulting receiver bandwidth reduction can be very valuable in a burst-mode context, as it potentially enables the use of older generations 10G-class BMRx technology that is already in low-cost volume production. For example, as experimentally demonstrated in the previous section, the scheme can support dual-polarization 100 Gb/s operation, with 6.25GHz receiver bandwidth which is compatible in principle with 10G BMRx technology, albeit this would need to be further adapted for coherent system operation. Furthermore, a 200 Gb/s dual-polarization 50 Gbaud QPSK system with N=4 slices could be achieved with the same front-end bandwidth, and so on for higher baud rates by further increasing N, providing a potentially scalable burst-mode-compatible coherent solution for future PON generations.

Similarly, each transmitter at the ONU may transmit the signals at different operating wavelengths to the receiver at the OLT, as illustrated in Figure 3.18 [47]. In a coherent system, to minimize these frequency offset impairments in the received signal, it is crucial for the burst LO (or comb source in SSRx context) laser's wavelength to be quickly locked to the transmitted signal. Although DSP can compensate for this frequency offset, the receiver's restricted bandwidth may limit the effectiveness of this compensation as the received signal suffered from frequency offset is severely filtered. Therefore, the performance tolerance to frequency offsets was analyzed using the SSRx with restricted receiver bandwidth. Figure 3.19 presents the receiver's sensitivity performance over a frequency offset range spanning nominally from 0 to 3 GHz.

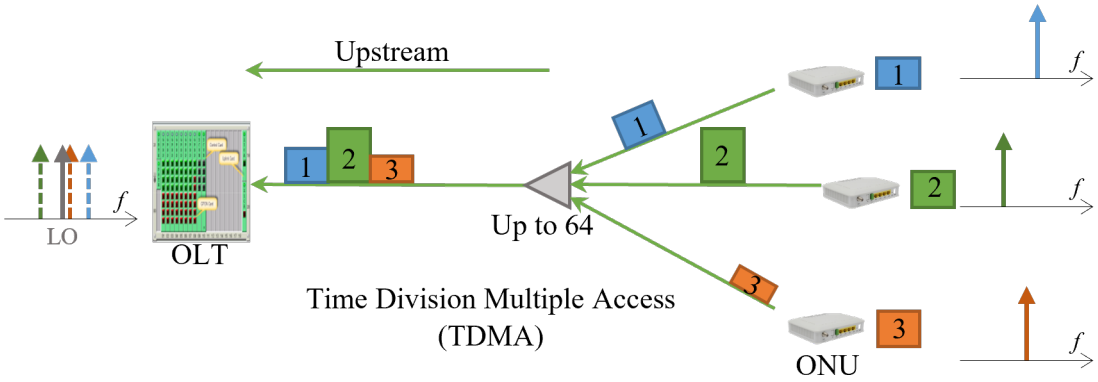


Figure 3.18: Implementation diagram of multipoint-to-point link transmission of PON according to ITU-T standard.

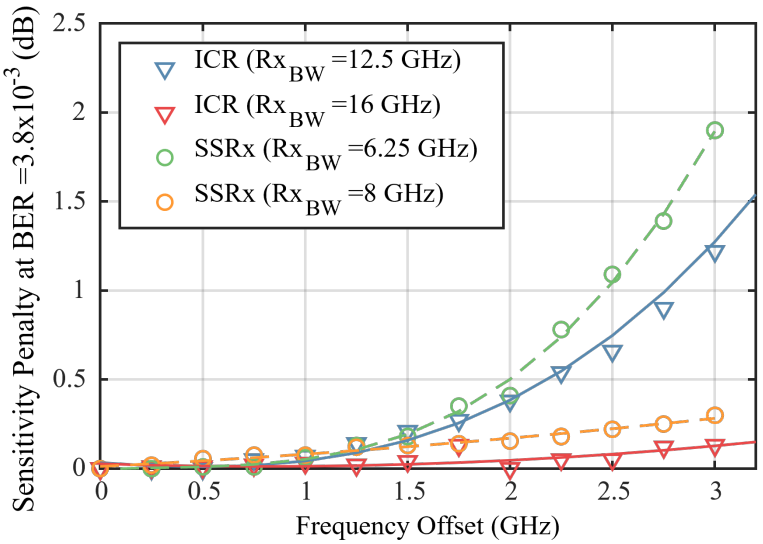


Figure 3.19: Tolerances to frequency offsets with varied bandwidth of the receiver.

It can be seen that the SSRx exhibits good tolerance to frequency offsets, similar to the ICR scheme. However, as expected, the performance of the frequency offset compensation algorithm deteriorates for both schemes due to signal information being lost when part of the spectrum falls outside of the Rx filter bandwidth. This effect can be mitigated by increasing the Rx bandwidth, as demonstrated by the red (ICR) and orange (SSRx) curves in Figure 3.19. In conclusion, the total combined receiver bandwidth of the SSRx system has almost the same frequency offset tolerance performance as a conventional coherent receiver, but the former has the advantage of utilizing lower-bandwidth components in the receiver.

Finally, burst-mode DSP presents another challenge for a coherent PON. Unlike downstream, which operates in continuous mode, DSP algorithms designed for

upstream must quickly react, equalize, and recover the burst signal in order to maintain data payload efficiency and not waste too much bandwidth, as illustrated in Figure 3.20(a). Since there is no accepted standard for the required preamble time for coherent PON, recent work suggested that burst signal preamble times at 72 ns are achieved [68]. Therefore, it is important to address this crucial aspect in the proposed SSRx reconstruction DSP by evaluating the preamble time requirement. Note that, in this analysis, the author only considers the preamble length for the slice reconstruction processing excluding burst clock recovery, frequency offset estimation, and carrier phase recovery. To identify the

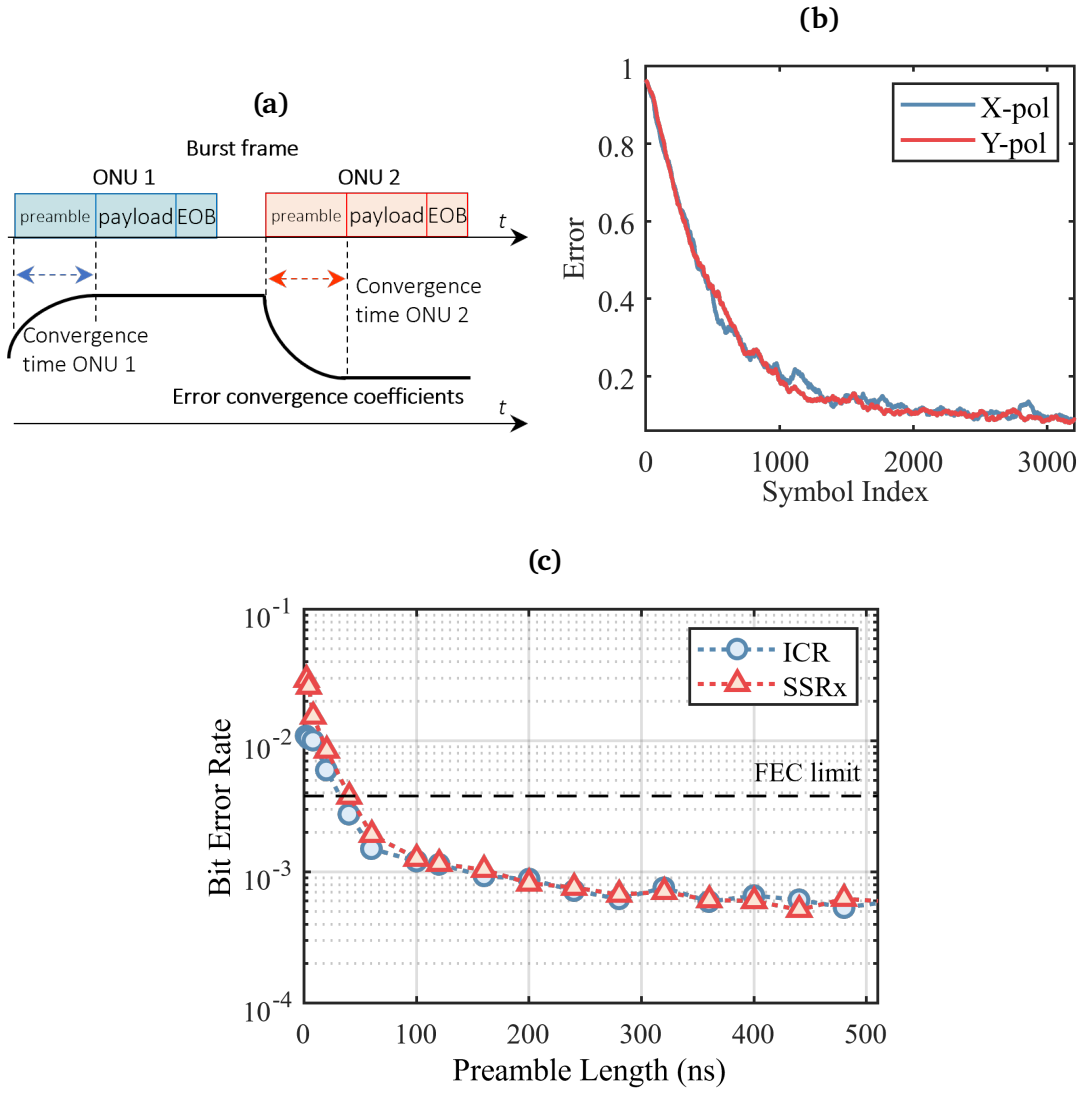


Figure 3.20: (a) Illustrative signal frame design operating in burst mode. EOB: End of burst. (b) Error convergence versus the symbol length in the equalization training in SSRx (N=2). (c) BER performance of 100 Gb/s DP-QPSK using the SSRx scheme versus the preamble length at a received power of −29 dBm.

optimal number of training symbols required, BER measurements were taken for different values of preamble length.

Figure 3.20(b) shows the error convergence of the reconstruction equalization for $N=2$. It can be seen that 1000 symbols are required for the preamble length to demultiplex and estimate the channel response. This is sufficient to be within the 2048 symbols allocated for pilot-aided equalization, as suggested in [69]. The author then tested the required preamble time taken to achieve channel reconstruction at the receiver sensitivity threshold, and the results are shown in Figure 3.20(c). Here, BER measurements were taken after 40 km fiber transmission and at a signal power received of -29 dBm. For comparison, the performance of burst-mode equalization in a conventional coherent receiver is also shown for the dual-polarization scheme. The DSP adaptive reconstruction equalizer successfully achieved BER below the FEC threshold when the preamble time is set to 40 ns. In principle, this equalizer process incorporates the recombination of the two slices while performing amplitude and phase equalization and restoring the polarization signals.

3.6.2 Comparison of SSRx with Coherent PON Candidates

In this section, the author summarizes the distinctions between the spectral slicing approach and other potential coherent PON technologies that offer cost-reduction opportunities (namely, digital subcarrier multiplexing and 'Lite' coherent receiver).

Subcarrier Multiplexing

As described in Chapter 1, the digital subcarrier multiplexing technology (DSCM) [70] is one of the potential candidates for coherent PON. The authors use the example of a 64 Gbaud single-wavelength carrier signal and demonstrate how it can be replaced by 16 non-overlapping subcarriers (SC) at 4 Gbaud with DSCM. In a point-to-multipoint link in a PON scenario, a coherent receiver with the appropriate bandwidth can select all or a subset of these SCs at a given PON terminal. In an extreme case where only one-sixteenth of the total data rate is required at the terminal, a single SC can be selected, reducing the receiver's bandwidth by a factor of sixteen compared to the single carrier case. However, this is the maximum data rate available at the terminal, and any increase requires an equipment upgrade by either increasing the single receiver bandwidth or increasing the number of narrow-bandwidth receivers proportionate to the

Table 3.2: Polarization and phase diversity coherent receivers. AEQ: Adaptive Equalization. CFO: Carrier Frequency Offset estimation. CPR: Carrier Phase Recovery.

	ICR	**DSCM**	**SSRx**
Baud Rate	*64 Gbaud*	*16 × 4 Gbaud*	*64 Gbaud*
Transmitter	*1×ECL + 2×I-Q Mod.*	*1×ECL + 2×I-Q Mod. + DSC DSP*	*1×ECL + 2×I-Q Mod.*
Front-end Components	*4×Class 40*	*8×Class 20* (No. of SC, M=4)	*8×Class 20* (N=*2)*
Rx DSP	*AEQ + CFO + CPR*	*DSC De-mux + AEQ + CFO + CPR*	*Reconstruction + AEQ + CFO + CPR*

number of SCs desired for detection.

Due to the larger symbol period in DSCM, narrower linewidth lasers are required compared to the single-channel case, and in the case of upstream communications, the uncorrelated phase noise from different transmitters will accumulate. In contrast, in spectral slicing, conventional time division multiplexing/multiple access (TDM/TDMA) is employed with a single carrier transmitter and a highly correlated comb source at the receiver, preserving laser linewidth tolerance, as only one transmitter laser is transmitting at any given instant in time for both upstream and downstream cases. The impact of phase correlation and laser linewidth in SSRx is discussed in Chapter 4 (see Section 4.2). The TDM/TDMA protocol also allows for fine-granularity bandwidth sharing and statistical multiplexing, which is important for mixed service provision and efficient and dynamic bandwidth use. The latter would be challenging for DSCM as low symbol rates and narrow SCs translate to the need for very high laser stability.

The spectral slicing approach reduces the front-end receiver bandwidth by a factor of N compared to the conventional receiver scheme, which, as mentioned, may be particularly advantageous for simplifying the burst-mode receiver design in the upstream channel case. In summary, these approaches have different merits, which the author summarizes from the coherent receiver aspect in Table 3.2 (using the system specification in [70]), also compared to the conventional coherent receiver case. For spectral slicing, the full signal bandwidth is received and reconstructed from N slices, so, for fairness, the author compares the equivalent performance case for DSCM where all SCs are detected by M coherent receivers, with bandwidth $1/M$ times the full signal bandwidth.

Alamouti-coding & Coherent Lite

In recent literature, "Coherent Lite" technology has been extensively studied to simplify the receiver architecture. The technology combines heterodyne detection with space-time block code (Alamouti coding) to create a minimal front-end coherent receiver design proposed for coherent PON [12]. However, this receiver introduces receiver sensitivity penalties of at least 6 dB due to redundant information transmission in both polarizations, using a single port of a 3-dB coupler, and doubling the front-end bandwidth requirement.

A comparison of the optical and electrical components in the front-end receiver to capture a 200 Gb/s signal using the 16QAM modulation format is presented in Table 3.3. Although the Coherent Lite receiver reduces component counts, it requires a high-bandwidth requirement in the front-end components (BPD, TIA,

Table 3.3: Comparison of component requirements of the front-end receivers. The number in the bracket indicates bandwidth requirement for 200 Gb/s.

	Optical	Electrical	Rx Sensitivity
Coherent Lite [71]	1×3-dB Coupler 1×PD (50 GHz)	1×TIA (50 GHz) 1×ADC (50 GHz)	>6 dB penalty compared to ICR
SSRx (N=2)	4× PBS 4×90 Hybrids 8×BPDs (6.25 GHz)	8×TIAs (6.25 GHz) 8×ADCs (6.25 GHz)	Similar to ICR

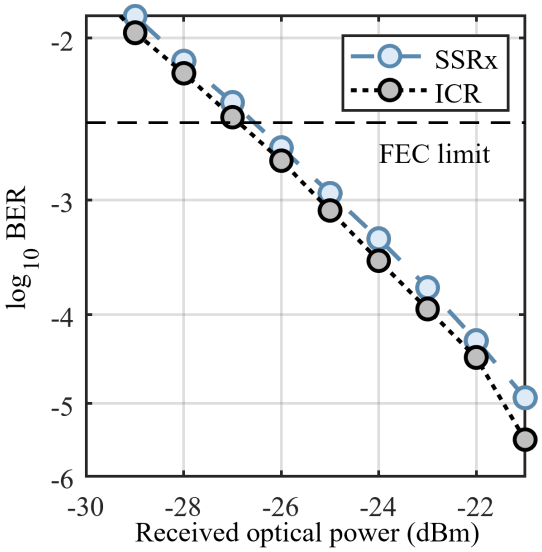


Figure 3.21: Sensitivity for 200 Gb/s DP-16QAM employing SSRx (N=2) over 40 km.

and ADC). The work in [12] has shown that this receiver (using 50 GHz front-end bandwidth) has a sensitivity of -18.5 dBm (at BER$=10^{-2}$) after 40 km fiber transmission. In contrast, the SSRx would only require 6.25 GHz bandwidth of the front-end components despite doubling the component count compared to a conventional coherent receiver. The simulation of receiver sensitivity performance indicates that the SSRx, which detects 200 Gb/s DP-16QAM, is comparable to that of the conventional coherent receiver (-26.5 dBm at the HD-FEC limit), as shown in Figure 3.21.

Contributions

The proposal and analysis of spectral-slicing for coherent PON, and proof-of-concept demonstration were presented and published as the following contributions:

- H. Othman, X. Ouyang, C. Anthony, P.D. Townsend, "Development of a Spectral-Slice Coherent Receiver," in *2021 Photonics Ireland Conference*, Ireland, 2021
- H. Othman, X. Ouyang, C. Anthony, F. Smyth, P.D. Townsend, "Spectrally-Sliced Coherent Receiver Utilizing Gain-Switched Optical Frequency Comb,' in *Journal of Lightwave Technology*, vol. 41, no. 16, pp. 5262—5274, 2023

3.7 Summary

In this chapter, the focus is on the concept and functionality of a spectrally sliced coherent receiver in the context of the potential application as a coherent technology in PON. Section 3.1 provides an overview of spectral-slicing-based technology, which offers a reduced overall cost of the receiver for the PON application. Section 3.2 includes the mathematical derivations governing the coherent detection of SSRx, starting from a wideband transmitted signal that mixes with different frequencies of LO lines, and moving towards the reconstruction principle that can be implemented in the DSP. Section 3.3 describes the essential components required to achieve spectrally sliced detection, including an array of coherent receivers, an optical frequency comb, and a DSP reconstruction algorithm.

Section 3.4 presents several investigations of the transmission performance of the spectrally sliced scheme at the system simulation level. This receiver modeling and simulation are designed to study the transmission performance in terms of different numbers of slicing operations. The impacts of receiver bandwidth, equalizer filter size, and complexity (devices and DSP) for optimal SSRx operation were discussed. In Section 3.5, 50 and 100 Gb/s transmission demonstrations over a fiber distance of 40 km which show the viability of SSRx were presented. The author further explores SSRx receiver sensitivity performance by employing different DSP reconstruction parameters to understand the most effective DSP configuration and the device calibration required for optimum receiver sensitivity performance.

Finally, Section 3.6 addresses the applicability of the SSRx scheme for the future optical access network in terms of burst mode operation and comparison with other coherent optical system candidates. Some of the key differences between alternative coherent receiver technologies and the SSRx were highlighted, highlighting the advantages of utilizing low-bandwidth components in the receiver front end not only to address cost reduction, but also to enable the required support for burst-mode operation, which is becoming challenging to realize as PONs evolve into the 100Gbit/s and beyond regime.

Chapter 4

SSRx with Enabling Photonic Integrated Circuit (PIC) Technologies

Coherent optics technology based on PICs is a critical requirement to realize cost-effective solutions for coherent PON applications, since optical and electrical components in a transceiver can be integrated in a single chip, thus reducing footprint, fabrication processes, and associated costs in assembling, packaging, and testing. The previous chapter emphasized the important role of the optical frequency comb in the context of spectral slicing, as it is used to serve as a multi-LO that covers the entire signal bandwidth for coherent detection. Therefore, implementing a compact on-chip OFC to support the spectrally sliced scheme is a key need for cost-efficient solutions and mass production.

In this chapter, the impact of OFC and the associated de-multiplexer properties on the receiver sensitivity performance was investigated. Based on these studies, the author demonstrates an SSRx utilizing a commercially available semiconductor-based gain-switched comb source and a commercial prototype monolithically integrated comb laser with an active de-multiplexer in PICs platform. This led to successful signal detection of a high-bandwidth, single-carrier 100 Gb/s DP-QPSK signal using two parallel integrated coherent receivers with reduced front-end bandwidths as low as 6.4 GHz. Importantly, these comb laser and de-multiplexer PIC solutions are key building blocks required for a future fully integrated SSRx for coherent PON.

The research work detailed in this chapter was also the subject of two peer-reviewed publications [72] and [73] and was carried out in collaboration with Pilot Photonics.

4.1 Introduction & Motivation

The optical frequency comb has proven to be essential in various applications, including mm-wave and THz signal generation [74, 75], optical spectroscopy, analogue radio-over-fiber systems [76], and flexible and spectrally efficient optical transceivers [77]. These applications leverage the high mutual coherence and precisely spaced comb of frequencies to achieve system benefits not possible with independent lasers.

For the spectral slicing application, the comb source should be adaptable for on-chip photonic integration to enable low-cost, robust, and compact transceiver fabrication. Previous spectrally sliced demonstrations utilized traditional discrete components for comb generation and demultiplexing in a laboratory environment. The optical frequency comb should ideally provide sufficient power per comb line for the receiver to operate in the shot-noise-limited regime for high sensitivity [78]. In a coherent communication system, a comb source must offer a low linewidth on each comb line. It is also important to consider the demultiplexer module that separates the comb lines into parallel receiver channels, which should have a minimal loss, footprint, and complexity.

When applying these considerations to 100 Gbit/s QPSK systems; expected to be the first coherent system deployed in future access networks [79], a relatively modest number of comb lines (e.g., N=4 or fewer) with a comb spacing of around 10 GHz (depending on the signal spectral width) could provide a suitable solution. Commercially available silicon photonic integrated circuit (PIC-based transceivers for the IEEE 400GBASE-DR4 standard and 4WDM Multi-Source Agreement utilize 4×100G or 4×25G wavelengths to achieve aggregate 400G or 100G data rates, respectively, indicating that high PIC yields can be achieved with this level of parallelization. This would allow the use of 10G class optoelectronic components such as photodetectors, TIA, and ADC, and as will be shown later in this chapter, can be realized with practical and achievable OFC and de-multiplexer parameters.

4.1.1 Optical Frequency Comb Candidate for Spectral Slicing

There are several techniques for generating OFCs, such as mode-locked lasers (MLL) [80]; microring resonators [81], electro-optic modulator-based comb sources (EO-OFC) [82], and gain-switched comb lasers [83]. Each method has its own advantages and disadvantages, depending on the specific application. For example, the ability to adjust the frequency separation between the comb lines is crucial in flexible optical network applications [84, 85]. In the context of SSRx, this ability is required for aligning the LOs with the signal spectrum. The previous chapter (see Section 3.4) demonstrated that increasing sensitivity penalties arise when the FSR is mismatched from the ideal frequencies.

To be applicable in the SSRx system, OFC must deliver certain spectral specifications to achieve optimal detection performance and system requirements. Comparisons of OFC attributes are listed in Table 4.1, which compares different comb source techniques. FSR is a crucial requirement in SSRx design, as it determines the allowable baud rate operation and the number of slices. Figure 4.1 shows the FSR requirement of a comb source as a function of the number of slices, N, for different operating baud rates. This analysis assumes that the transmitted optical signal has a bandwidth similar to the baud rate value. At all the baud rates considered, it is possible to reach the 10—20 GHz FSR range and utilizing the 10G class components bandwidth range, which was motivated in the previous chapter as important from a burst-mode operation perspective, with relatively modest numbers of slices in the range 2 to 5. As discussed further below, this gives important pointers to the optimum choice of OFC technology for this particular application.

Gain-switching (GS) OFCs have several advantages, especially regarding their potential for photonic integration and flexibility in comb spacing tuning. Similarly, EO-OFCs, demonstrated with the SSRx in the previous chapter, can provide the same tuning flexibility as GS-based OFCs. However, EO-OFCs are typically based

Table 4.1: Comb generation techniques comparison

Comb	**FSR**	**Linewidth**	**Spectral bandwidth**	**PIC Complexity**
EO-based	*Flexible*	*Low*	*Limited to few nm*	*Difficult*
GS-based	*Flexible*	*Low*	*Limited to few nm*	*Ease of integration*
Microring	*Fixed*	*Low*	*Hundreds of nm*	*Ease of integration*
MLL	*Fixed*	*Noisy*	*Tens of nm*	*Ease of integration*

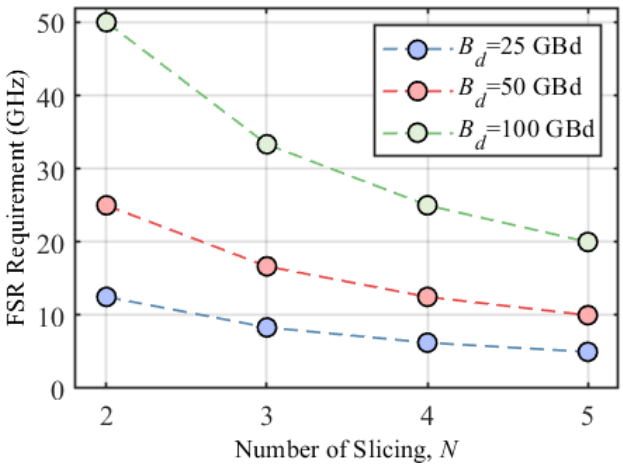


Figure 4.1: Free spectral range requirement of a comb source in spectral slicing.

on discrete, large footprint modulators (e.g. Lithium Niobate MZMs) which require large drive voltages and hence are power-hungry. Other techniques, such as MLL and microring-based comb generation, have the advantage of generating very large numbers of comb lines; however, this is not necessary for spectral slicing applications. Instead, the comb is required to generate a small number, but high power per line, which matches the GS OFC specifications well. The comb spectral bandwidth feature listed in Table 4.1 refers to the overall bandwidth that can be occupied by all lines generated. While microring-based OFCs are currently mature for chip integration, they are generally designed to generate a much larger number of lines than this application requires. Similarly, MLL-based combs are more difficult to integrate due to the typically used cleaved cavity. Moreover, the comb signal generated by MLL typically has a linewidth that is too large for a coherent communication system.

The number of comb lines that a GS-based OFC can generate is limited by the spectral bandwidth of the laser gain medium and its comb spacing configuration. However, the injection locking technique has played a key role in improving the number of usable lines with sufficient power and excellent phase coherence [86]. The effectiveness of injection locking depends on several factors, such as primary-secondary laser power ratio and frequency offset de-tuning [87]. Several IL-GS comb source experiments have demonstrated the generation of up to 24 sub-channel transmission with 12.5 GHz line spacing [85]. However, for this SSRx application, only a modest number of comb lines, such as N=2 or 4, are needed. Nevertheless, the excellent phase coherence and low linewidth attributes enabled by injection locking are valuable in the spectral slicing context, as the comb signal

will be utilized as a LO. Based on these considerations, the chapter will focus on the use of gain-switched laser-based OFCs for the SSRx application.

4.1.2 Comb De-multiplexer Candidate for Spectral Slicing

OFCs play a critical role in high-capacity DWDM optical communication as each comb line corresponds to CW light, which can be used as a signal carrier at different wavelengths [88]. Before signal modulation, it is essential to select and manipulate the comb channels to ensure that each individual line is separated from the other adjacent comb lines. Therefore, an optical filter with channel selectivity and high-finesse channel isolation capabilities is crucial for OFC-based signal transmission [74, 89]. In a spectral slicing context, an individual line from the comb signal generated by the OFC is needed to serve as an LO in each receiver channel, thereby requiring a comb de-multiplexer.

The desired properties of a de-multiplexer in the proposed SSRx include low insertion losses, large channel isolation, cost-effectiveness, and ease of integration with an OFC. By leveraging monolithic and photonic integration technologies, the complexity, footprint, and cost associated with deploying an OFC with a de-multiplexer can be reduced [90].

Various types of optical filters have been demonstrated for comb demultiplexing in optical communication systems, with one commonly used type being the ar-

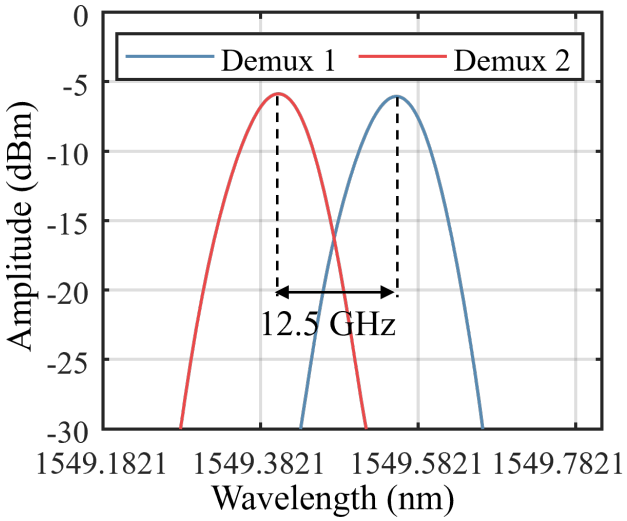


Figure 4.2: Measured intensity transfer function of bandpass filters generated from WSS. The filter bandwidth was configured at the narrowest setting, which was measured to be around 10 GHz.

rayed waveguide grating. However, arrayed waveguide gratings may introduce relatively large insertion losses and exhibit temperature dependence, leading to potential wavelength shifts in the filter bands.

Another type of de-multiplexer commonly used in WDM-based optical transmission systems is the wavelength selective switch (WSS), which is typically based on a liquid crystal on silicon (LCoS) technology [91]. This de-multiplexer was used in the previous chapter as a comb de-multiplexer in an SSRx. The intensity responses of the narrowest bandpass filter configured by a WSS (Finisar Waveshaper4000S [92]) are depicted in Figure 4.2. Although the WSS offers high precision and flexibility to generate multiple passband filters, it comes with limitations such as large insertion losses (>5dB) and restricted filter bandwidth settings (minimum bandwidth of 10 GHz).

To address these drawbacks, an effective demultiplexing technique is required. The optical injection locking technique, as utilized in a gain-switched OFC, can be employed to achieve high-quality demultiplexing of the comb [93]. Section 4.4 presents the concept and operation of such a de-multiplexer.

4.2 Investigation of Comb & De-multiplexer Properties on SSRx Performance

The performance of the proposed SSRx is compared with that of a conventional integrated coherent receiver (N=1). In this section, the author investigates how the properties of both the OFC and comb de-multiplexer affect the quality of the reconstructed signal on a transmission link. VPITransmissionMaker® was used to simulate the optical transmission, and the OFC generation setup is shown in Figure 4.3(a).

The transmission building blocks and flows are similar to the simulation work in Section 3.4.1, where 25 Gbaud data with a single polarization signal was transmitted. The author analyzed the simplest case of N=2 spectral slices for consistency with subsequent experiments. However, the conclusions are valid for a larger number of slices. An MZM was used to generate the frequency comb from a single laser to emulate the ideal, highly correlated case. Unless otherwise stated, the power per LO comb line was set at +10 dBm for consistency with the later experiments. After detection, the signal was sampled at 50 GSa/s and 25 GSa/s for the conventional and SSRx schemes, respectively, before being sent

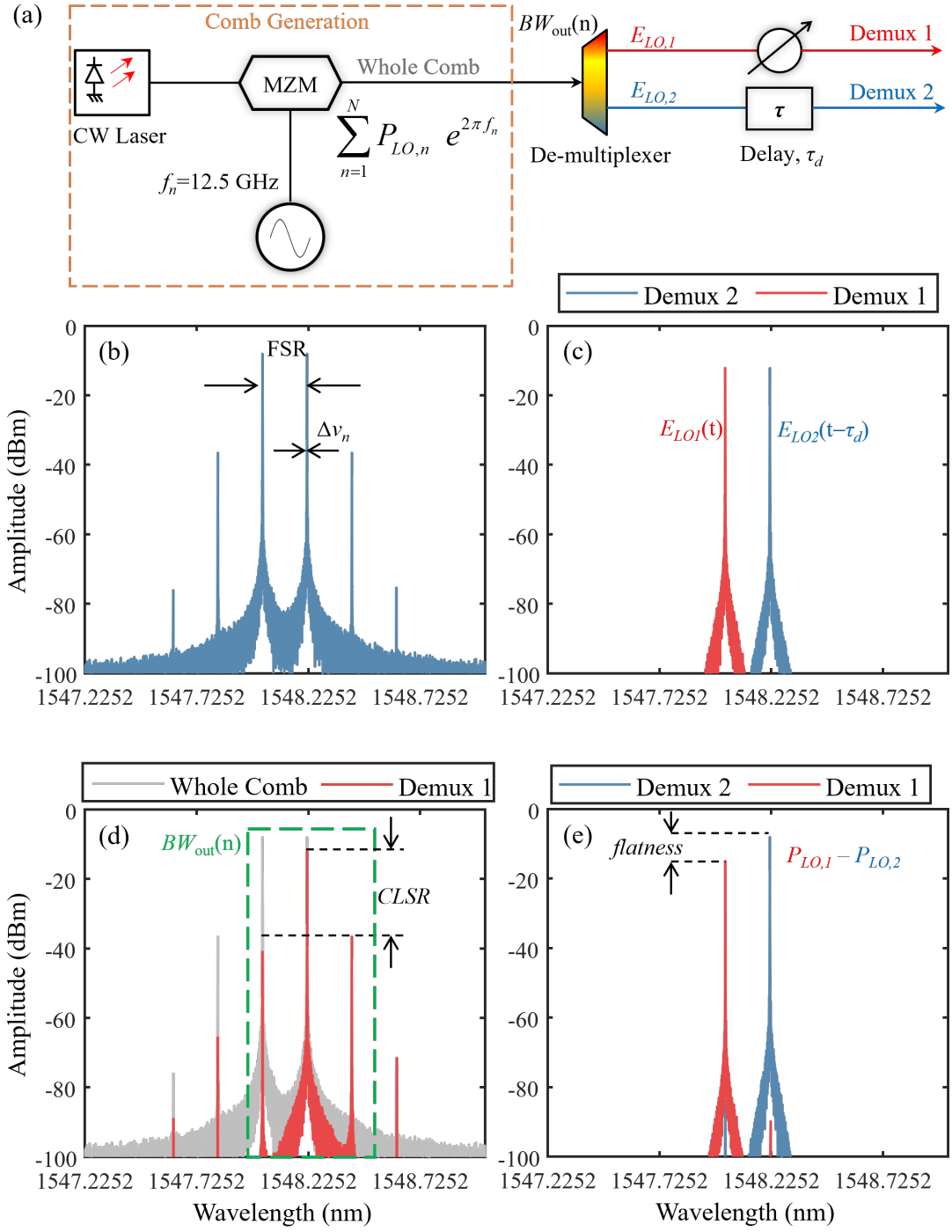


Figure 4.3: (a) Simulation system model of optical frequency comb signal generation (brown blocks) and comb de-multiplexing for a spectrally-sliced coherent system using N=2 slices. Schematic comb spectra at various points in the simulation illustrating key parameters for consideration: (b) comb linewidth; (c) phase coherence of comb line; (d) comb line side-mode suppression ratio (CLSR) after demultiplexing; (e) comb amplitude flatness.

Table 4.2: Simulation parameters

Device Parameter		Laser Parameter	
LO power, $P_{LO,n}$	+10 dBm	Central wavelength,	1559.0 nm
PD responsitivity, *R*	0.7 A/W	Linewidth	100 kHz
Tx pulse shaping roll-off	0.1	Comb spacing	12.5 GHz
Thermal noise	19 $pA/\sqrt{Hz}$	General Parameter	
Slice bandwidth, BW_{slice}	6.25 GHz	Symbol rate, B_d	25 Gbaud
Conventional bandwidth, BW_{ICR}	12.5 GHz	Num. of Pol	1
ADC effective number of bit	8 bits	Num. of slicing, *N*	2

to the DSP for signal reconstruction and recovery. The DSP blocks that perform these functions are similar to the previous work in Sections 2.4.1 and 3.4.1 for the conventional coherent receiver and SSRx detection schemes, respectively. Finally, after remapping, the signal quality was calculated based on bit error counting. The rest of the simulation parameters are listed in Table 4.2.

To establish a baseline for the SSRx system's ideal performance, the sensitivity power penalty was simulated for a range of LO comb powers (per line), as shown in Figure 4.4 evaluated at the FEC limit relative to +15 dBm LO power of each scheme. There is an almost negligible performance penalty between the two receiver schemes throughout the simulated LO power range. It would be difficult to achieve a high output power peak per line (for high receiver sensitivity) from the OFC since the power generated from a laser is distributed amongst the comb tones. However, it is possible to compensate for the losses by employing optical amplification after comb demultiplexing or by using an active de-multiplexer that is co-integrated with the comb source. This approach has been exploited in a PIC platform and has been shown to simultaneously increase the power of the comb line and the suppression ratio [94], which, as demonstrated in Section 4.4, improves the performance of the spectrally sliced system.

Having established the SSRx baseline performance, the author now proceeds to simulate how some of the key parameters that characterize a practical OFC source affect this performance.

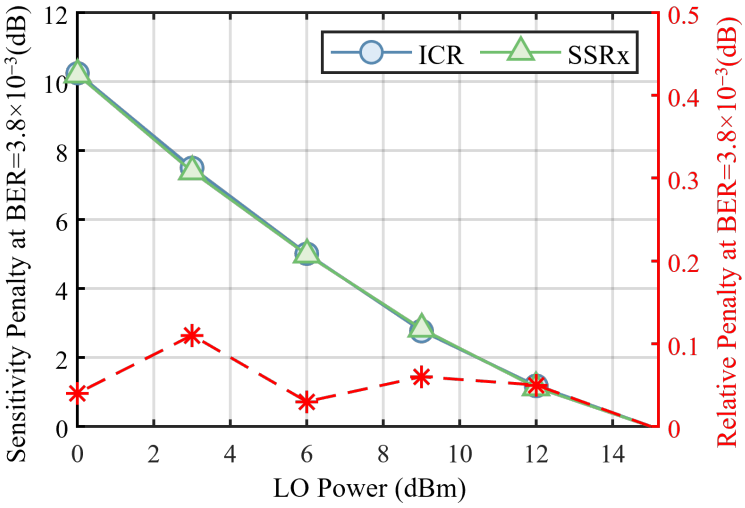


Figure 4.4: Simulated receiver sensitivity penalty as a function of local oscillator power. The red curve indicates the relative sensitivity penalty between the ICR and SSRx detection schemes.

4.2.1 Spectral Flatness

The difference in amplitude between OFC comb lines, termed spectral flatness, is one of the key parameters that affect OFC performance in an optical communication system. In the SSRx application, the spectral flatness and channel-to-channel insertion loss variations in the associated de-multiplexer lead to variations in the LO power P_{LO} across the N slices. After signal mixing and detection, this variation leads to amplitude imbalances between slices that can degrade the quality of the reconstructed signal. This effect was emulated in the simulations for the $N=2$ case by attenuating the optical power of one comb line with respect to the other. Specifically, one of the LO powers was varied from +3 to +10 dBm, while the other was fixed at +10 dBm, giving a spectral flatness ranging from 7 to 0 dB.

The sensitivity penalty was measured at different values of spectral flatness relative to 0 dB ($P_{LO,1}=P_{LO,2}=+10$ dBm). The impact of adaptive equalization on reconstruction processing was also analyzed by varying the tap size. As shown in Figure 4.5, the performance of the SSRx system degrades as the spectral flatness parameter increases. This is an easily understood consequence of the thermal noise contribution in the low-LO power receiver branch, which degrades the total SNR of the reconstructed signal. Furthermore, as the amplitude mismatch between the two slices increases, a larger number of equalizer taps are required to compensate for the mismatch to achieve optimum reconstruction performance.

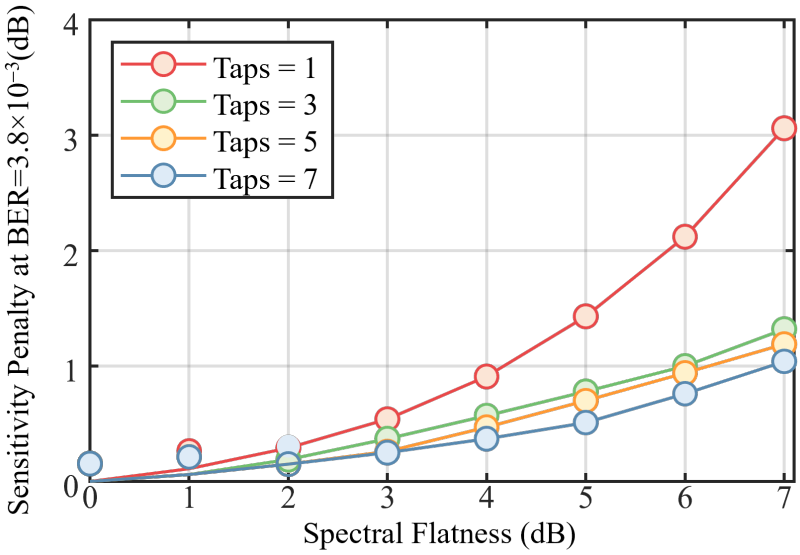


Figure 4.5: Simulated sensitivity penalty versus the spectral flatness generated by comb source relative to the spectral flatness of 0 dB.

As PIC-based combs can readily achieve spectral flatness values of less than 3 dB, with optimized equalization taps, the impact of this factor can be of the order of 0.3 dB or less in terms of sensitivity penalty.

4.2.2 Optical Linewidth

The optical linewidth of the local oscillator laser is one of the most crucial factors for coherent system performance in optical fiber communications, especially when higher-order modulation formats are used. For the comb source, the seed laser that generates the optical carrier for the RF signal applied to the modulator will have phase noise that is quantified by the laser linewidth Δv. The phase noise of the comb is contained within the term φ_{LO} of Equation 3.4 and can be expressed as:

$$\varphi_{LO}(t) = \varphi(t-1) + \Delta\phi(t), \tag{4.1}$$

where $\Delta\phi$ is the zero-mean Gaussian random variable with variance defined by $2\pi\Delta v$ / B_d where B_d is the symbol rate. This distortion can be estimated and compensated using the phase estimation DSP based feedforward scheme.

The impact of linewidth and symbol duration product ($\Delta v/B_d$) on the performance of an SSRx and the conventional coherent receiver was simulated for two different modulation formats, QPSK and 16QAM. To ensure that the phase

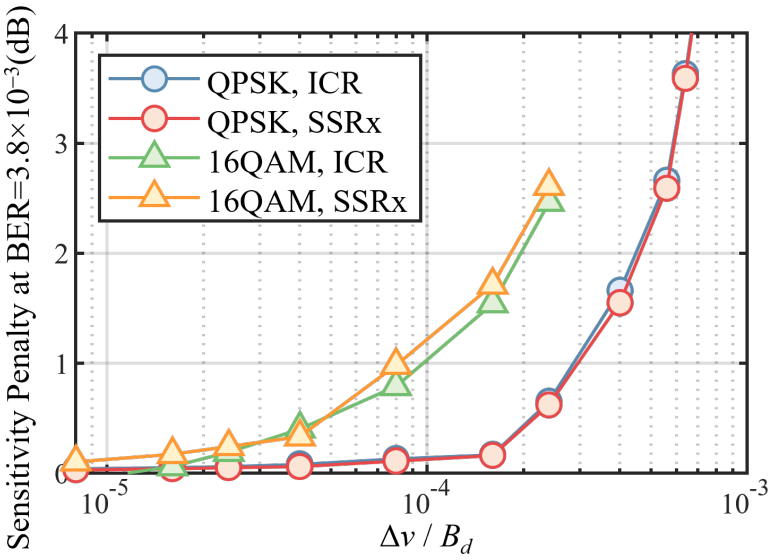


Figure 4.6: Simulated sensitivity penalty as a function of the product of the laser linewidth Δv and symbol duration $1/B_d$ for two different modulation formats.

noise from the OFC (as LO) was dominant in the system, the transmitter laser linewidth was set to 0 Hz. Phase estimation was carried out using symbol block averagings of 20, and the sensitivity penalty was calculated with respect to transmission performance without LO phase noise (Δv=0). The results are shown in Figure 4.6. The same tolerance trends for both receiver schemes were observed, and as expected, 16QAM is less tolerant to phase noise than QPSK since more discrete phases need to be discriminated for correct symbol detection. For a penalty of 1 dB, the maximum tolerable linewidth and symbol duration product are around 3×10^{-4} and 0.8×10^{-4} for QPSK and 16QAM, respectively, for both receiver schemes. This result shows that the SSRx has the same phase noise tolerance as a conventional coherent receiver. As will be shown in Section 4.3.2, the IL-GS OFC used in the experiments has a linewidth of approximately 300 kHz, giving a linewidth and symbol duration product of 1.2×10^{-4} at 25 Gbaud. Therefore, the results shown in Figure 4.6 confirm the feasibility of using this OFC in the SSRx to achieve low phase noise penalties.

4.2.3 Comb Coherence

Finally, the impact of one of the key properties of the OFC, namely the degree of phase correlation between the comb lines, was investigated. In practical OFCs, phase correlation is affected by the fundamentals of the comb generation process in the OFC laser cavity and the injection locking process when an external,

narrow-linewidth primary laser is used, as in the IL-GS OFC case. In addition, where external RF modulation is employed, noise from the driver electronics could, in principle, also generate decorrelation in the generated comb lines.

In simulation modeling, phase decorrelation was emulated by adding a relative time delay, τ_d to one of the comb line paths following demultiplexing. This is carried out by circularly shifting the numerical array that represents the optical field of the LO comb line by the number of sample points corresponding to τ_d. Hence, the phase difference of the two comb lines can be written as:

$$\varphi_{LO,1}(t) - \varphi_{LO,1}(t - \tau_d), \tag{4.2}$$

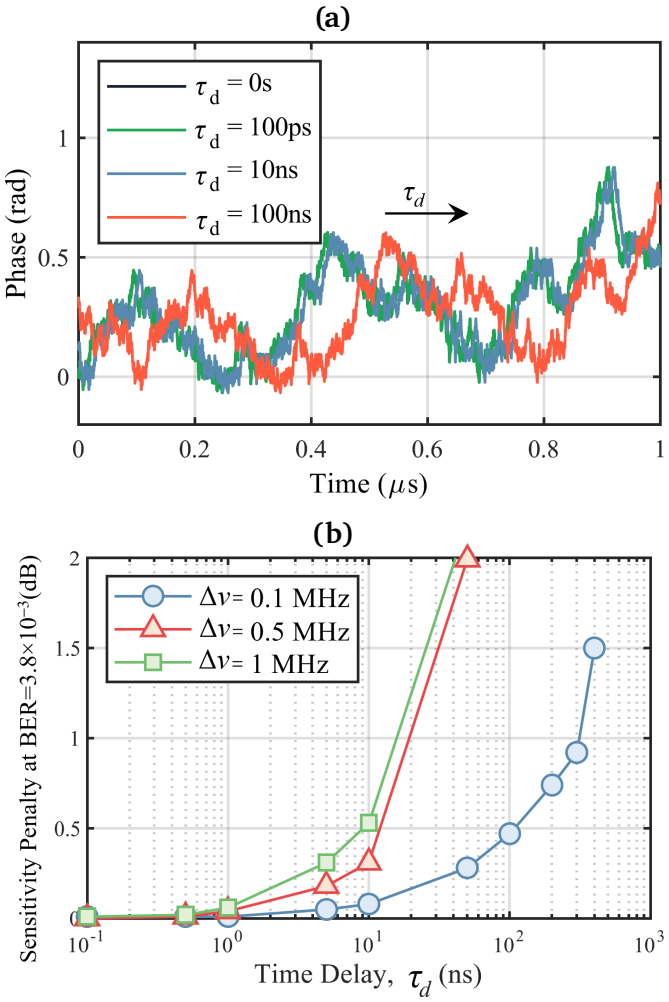


Figure 4.7: (a) Phase noise traces of comb line (Δv=100 kHz) with delayed versions of itself. (b) Simulated sensitivity penalty versus applied time delay for three different linewidth.

Figure 4.7(a) shows an example of a simulated phase trajectory for one of the LO lines and the impact of the applied time shift for various values of τ_d. When τ_d is zero, both LO lines will have identical phase trajectories. However, an instantaneous phase decorrelation between the two LO lines is generated as τ_d increases. The impact of this decorrelation on the performance of the SSRx system is presented in Figure 4.7(b) for different values of linewidth, Δv. The performance penalty is negligible as long as the time delay is small compared to the inverse linewidth. For the IL-GS OFC which has 300 kHz linewidth used in the experiments, this translates into a relative time delay of around 12 ns for a sensitivity penalty of less than 1 dB, which is easily satisfied in a PIC implementation. However, as discussed above, practical OFCs suffer from other sources of phase decorrelation, even when the receiver channel path lengths are well-matched, so this is an important factor to study in the following experiments.

4.2.4 Comb-Line Suppression Ratio

As mentioned in the previous section, the OFC de-multiplexer is essential in the SSRx to select the desired comb tone as the LO for each sliced receiver channel. A practical de-multiplexer has non-zero inter-channel crosstalk which, in the SSRx context, results in some leakage of adjacent LO tones into a given receiver channel. This leads to additional beat products in the reconstructed signal that may impair the performance of the SSRx.

Simulations were carried out to investigate the impact of this effect on the varying levels of CLSR, calculated as P_{LO}–P_{SM} (dB), where the first term corresponds to the power of the desired tone and the latter term is the power of the dominant side tone. To vary the CLSR in the simulations, the filter bandwidth of the comb de-multiplexer was varied. The spectrum of the filtered comb lines is shown in 4.8(a). As the filter bandwidth broadens, the adjacent tone's power increases, thus reducing the CLSR. Figure 4.8(b) shows the simulated sensitivity penalty as a function of CLSR for the SSRx scheme. For a higher CLSR (>20 dB), the sensitivity penalties induced are below 0.5 dB, highlighting the importance of CLSR for the high-quality signal reconstruction performance of the SSRx system. Note that research on the InP-based active comb de-multiplexer has shown that CLSR values of this magnitude can be achieved in OFC PICs [90].

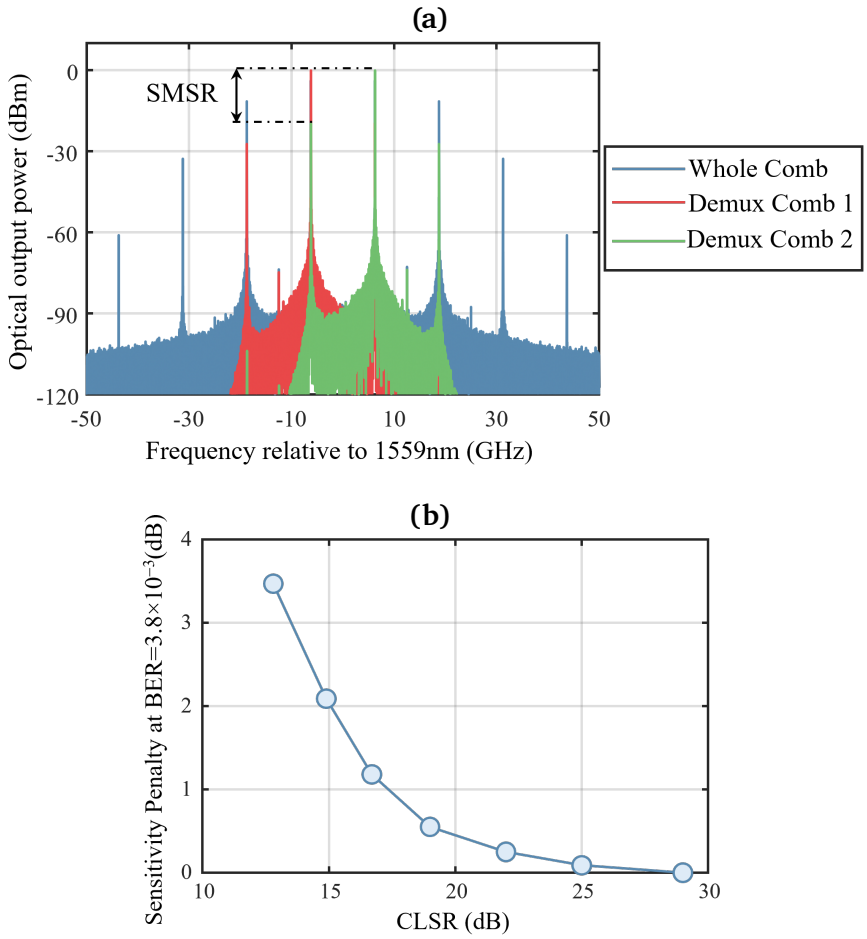


Figure 4.8: (a) Spectra were captured for the whole frequency comb (blue) and two isolated combs filtered by de-multiplexer with finite bandwidth (red and green traces). (b) Simulated sensitivity penalty versus CLSR for SSRx detection.

4.3 Gain-Switched Comb with Injection Locking (IL-GS OFC)

4.3.1 Key Concept

In this section, the author generated a frequency comb using a commercial discrete DFB laser packaged in a 7-pin butterfly module. Here, a DFB module is used where the built-in diffraction grating structure is within the laser structure, and acts as Bragg reflector to allow only a single longitudinal mode in the lasing emission.

Gain-switching based OFC can be designed by driving a single-mode semiconductor laser with an amplified RF signal, where the laser operates in a non-linear regime, oscillating between below and above the laser-stimulated threshold. Dur-

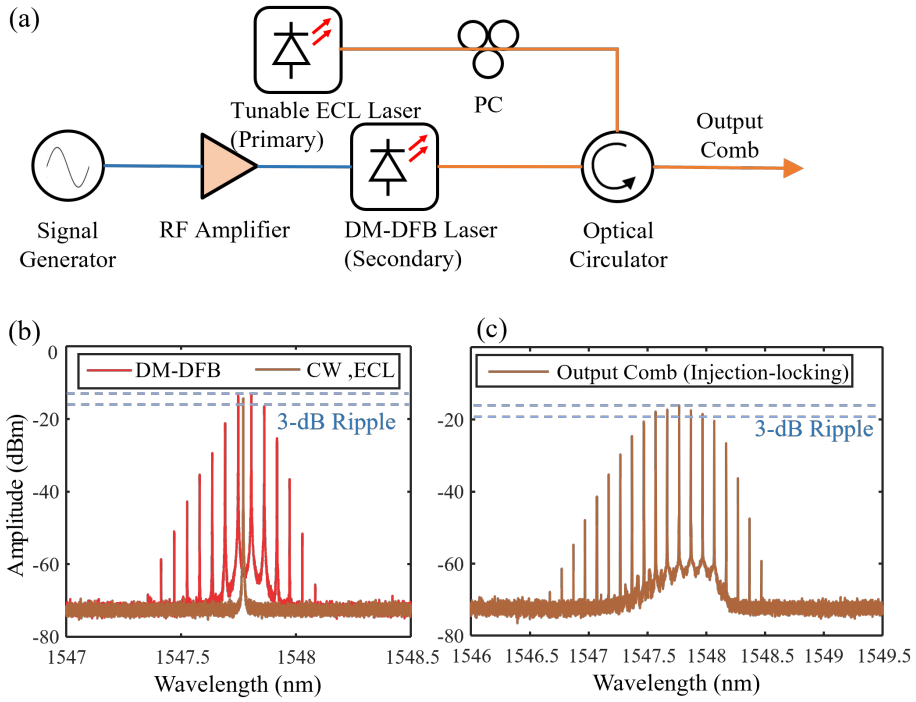


Figure 4.9: (a) Schematic diagram of an injection-locking gain-switched frequency comb. (b) Optical spectrum captured with 20 MHz spectral resolution of: (Left) Comb signal from gain-switched DFB laser and tunable ECL laser. (Right) Injection locking with gain-switched comb signal.

ing the first oscillation spike process, the injection current initially builds-up the carrier density until it reaches the stimulated threshold value, causing the photon density to increase rapidly, where the lasing emission is generated. Then, when the bias current swings to below its threshold value, the carrier starts to deplete, which reduces the photon density. Consequently, only the first spike of the relaxation oscillation is excited, generating an optical pulse train with a repetition frequency (f_{rep}) equivalent to the frequency of the RF signal.

Gain-switching with injection locking is a process that generates a high-coherence train of optical pulses based on the gain-switching principle [95]. In injection locking, the performance of the comb signal is improved, typically in terms of modulation bandwidth response and phase properties [96]. An externally isolated laser source (referred to as the primary laser) is coupled with the cavity of a directly modulated (DM) laser (referred to as the secondary laser), as illustrated in Figure 4.9(a). This allows light from the primary laser to inject unidirectionally into a secondary laser, overcoming spontaneous emission inside the cavity. As a result, the secondary laser behaves as a copy of the primary laser. Figures 4.9(b) and 4.9(c) show the optical spectrum of the comb signal before and after injection locking, respectively, highlighting the improved quality in terms of the

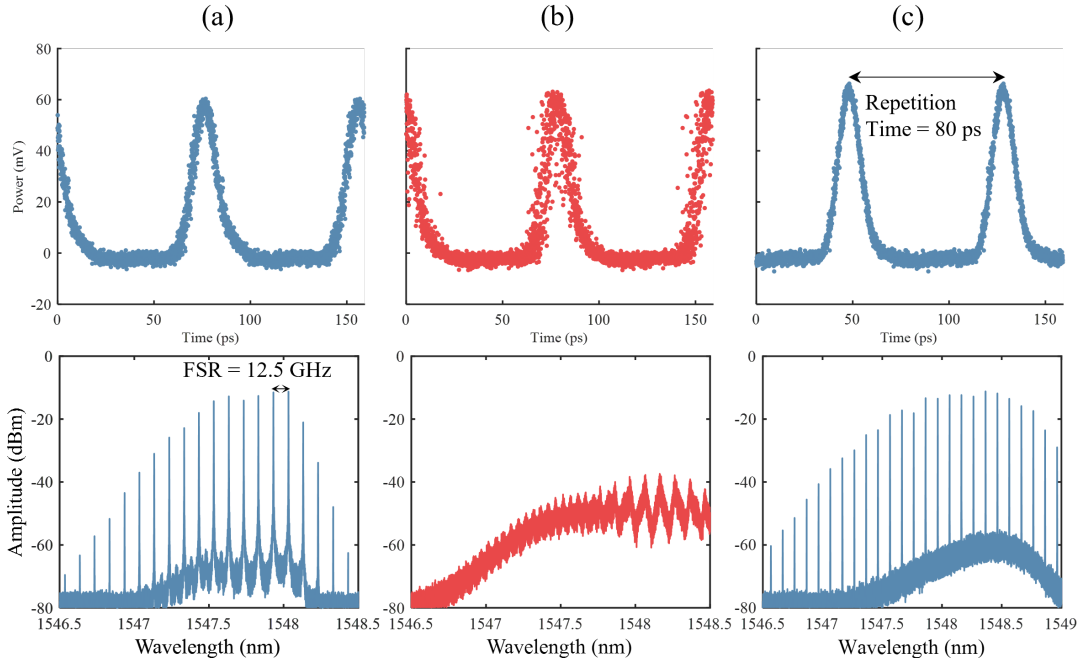


Figure 4.10: Top: The pulse sampling of the optical frequency comb in the time-domain, bottom: Optical spectrum captured with the spectral resolution of 20 MHz for different gain-switching configurations. (a) DFB laser driven at 12.5 GHz sinusoidal RF signal with +5 dBm amplitude, (b) DFB laser driven by +20 dBm RF signal, and (c) DFB laser driven at +20 dBm RF signal with applied injection locking from an ECL laser.

number of lines generated within the 3-dB spectral flatness.

When a laser is driven by an RF signal with sufficient power to oscillate from below to above the stimulated threshold, it generates a pulse repetition train with a frequency similar to that of the driving RF signal, resulting in a comb spectrum, as shown in Figure 4.10(a). Further amplifying the RF driving power increases the amplitude swings in the non-linear regime, switching between well below and above the threshold. This creates a phase decorrelation between pulses caused by random spontaneous emissions. This leads to high temporal jitter and phase noise in the generated comb lines, as shown in Figure 4.10(b). However, by applying injection locking with optimized mode matching, frequency de-tuning, and power ratio of the primary to secondary laser, the primary laser forces the secondary laser to oscillate at its phase and frequency, thus transferring low optical linewidth properties onto the comb signal [97, 98]. Figure 4.10(c) demonstrates low-jitter pulses and much narrower comb lines (low linewidth) generated. In this example, injection locking was achieved by applying the primary laser's power at −5 dBm to the secondary laser and operating wavelength of 1547.8 nm.

4.3.2 Module Characterization

The OFC used in the following demonstration is based on the gain-switching of an optically injected semiconductor laser in a packaged module (Pilot Photonics - LYRA-OCS-1000) [99] and is schematically represented in Figure 4.11(a). The module consists of two integrated Fabry-Perot lasers in a primary-to-secondary configuration. Here, the primary section is formed with two reflector sections at each side to provide wavelength-selective feedback, thereby ensuring that single-mode emission is injected into the secondary laser. The need to suppress the multimode emission before injection-locking is required so as to force the secondary laser to oscillate at the primary laser frequency and phase and inheriting its noise properties [87]. An RF signal of 12.5 GHz was generated to gain-switch the laser, producing a frequency comb signal, as shown in Figure 4.11(b). Five tones were generated with power per comb tone of more than −10 dBm within 6-dB spectral flatness.

The FM noise spectrum of the IL-GS OFC was characterized using a method similar to the one discussed in [100] This involved analyzing the phase noise of the beat signals captured by a coherent receiver. To characterize the OFC, a 30 kHz linewidth tunable ECL was used as a reference to mix with each comb line in a coherent receiver. The captured waveforms were post-processed using MATLAB to generate the FM-noise of the comb signal. The same process was also applied to characterize the phase noise of the EO-OFC for comparison.

As shown in Figure 4.12(a), the IL-GS OFC exhibits similar FM noise spectra for each of the five main tones, with a measured linewidth of approximately 300 kHz.

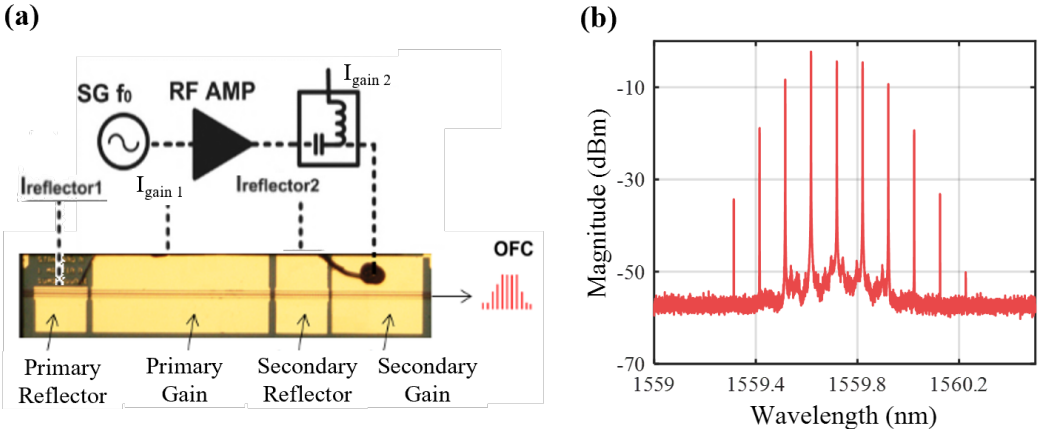


Figure 4.11: (a) Schematic diagram of an injection-locking gain-switched Fabry–Pérot (FP) laser-based frequency comb. (b) The output optical spectrum of the comb source with 12.5 GHz frequency spacing.

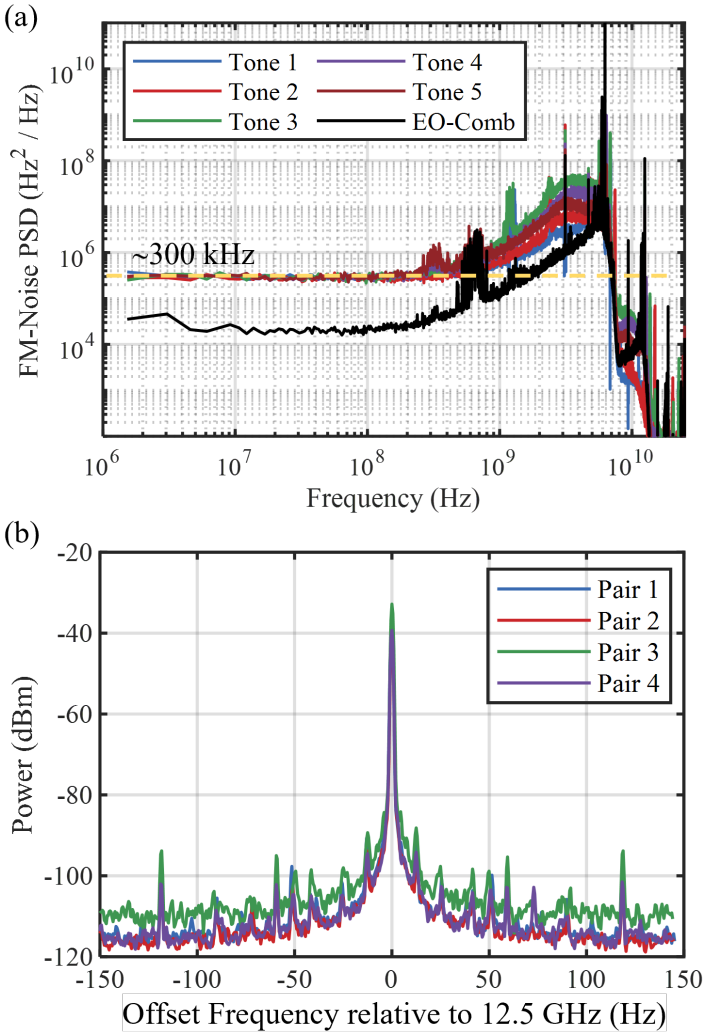


Figure 4.12: (a) Calculated FM-noise spectrums for both EO-OFC tones and for IL-GS OFC (all five main tones). (b) RF beat tones generated between the pair of comb lines for all four IL-GS OFC pairs captured at 12.5 GHz offset frequency.

For the EO-OFC case used in the previous experiment works in Chapter 3, the observed linewidth for the two filtered comb lines is around 30 kHz, presenting a negligible deviation from the source laser (ECL). It might be thought that the higher linewidth of the IL-GS OFC is responsible for the slightly higher penalty measured in the transmission experiments which is presented in the next section. However, as shown by the previous simulation results in Figure 4.6, a negligible penalty is expected for the 25 Gbaud QPSK modulation with 300 kHz comb linewidth.

Further investigation was performed to assess the phase correlation measurement of the IL-GS OFC across the four comb line pairs. The beat signal was captured by an ESA with a high-resolution bandwidth (RBW=3 Hz) after the two consecutive

comb lines, with a separation frequency of 12.5 GHz, were filtered and detected by a PD for each pair. Figure 4.12(b) shows the consistent and very narrow full width at half maximum of the beating tones, which was measured to be around a few Hz, indicating a high degree of phase correlation between all pairs of comb lines. This suggests that the relative phase coherence times between comb line pairs are on the order of tenths of seconds, much longer than the record lengths of 20 μs used for data acquisition in transmission experiments. Therefore, the phase correlation properties of the OFC here are good enough to have a negligible penalty impact on the slice reconstruction process.

4.3.3 Demonstration of an SSRx Utilizing an IL-GS OFC

Experimental Setup

To demonstrate the feasibility of the proposed SSRx detection scheme (N=2) with an IL-GS OFC (presented in the previous section), an experimental coherent system testbed was built and illustrated in Figure 4.13(a). The carrier signal was generated by a tunable ECL with a 30 kHz linewidth and a wavelength of 1559.53 nm. The lightwave was then modulated by an I-Q modulator driven by 25 Gbaud QPSK signals generated from the 50 GSa/s AWG. The optical signal from the transmitter (launch power=+4 dBm) propagates over a 40 km optical fiber link (Corning SMF28E+) before the signal is attenuated by a VOA that is used to vary the ROP.

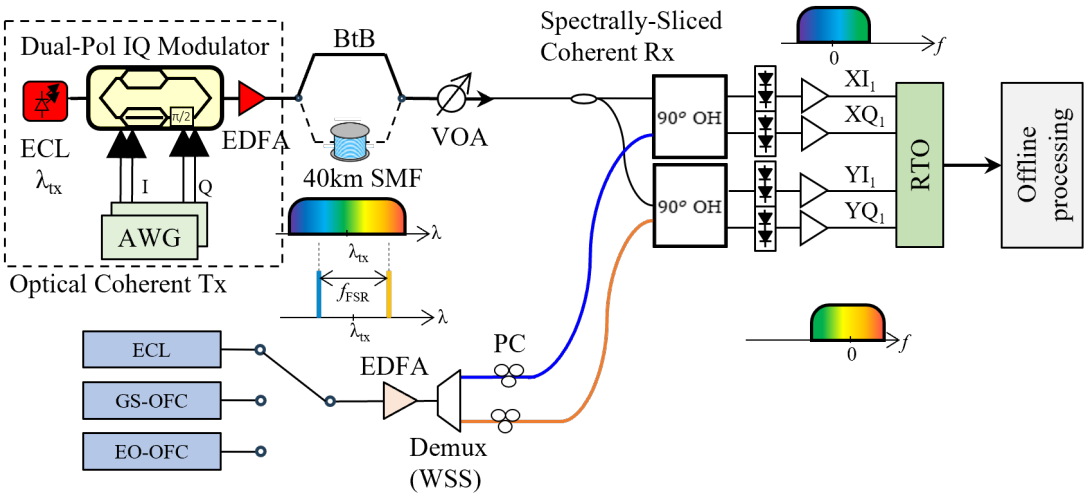


Figure 4.13: (a) Experimental setup for 50 Gb/s SP-QPSK with (N=2) SSRx over 40 km of SMF. The GS-OFC used in this experiment is based on Pilot Photonics LYRA-OCS-1000, while the Finisar Waveshaper (WSS) is used as the comb demultiplexer.

At the receiver, the SSRx was constructed from two single-polarization coherent receiver modules (u^2t photonics CPRV1010A) with front-end bandwidths of 25 GHz, which employ two neighbouring comb lines (separated by a WSS and amplified to +10 dBm each) as LOs. The FSR of the comb was set to 12.5 GHz. The PC ensures that the LOs and the signal are co-polarized with each other. Finally, the electrical signals from the receivers were sampled by two synchronized RTOs operating at 100 GSa/s before the sampled waveforms were stored for offline signal processing.

The DSP to recover and measure the system performance by BER counting was performed in MATLAB. First, a deskew calibration operation was performed to compensate for the path delay introduced by cable length mismatches. Then, the two parallel complex inputs, corresponding to the slice 1 and slice 2 signals, were filtered in the digital domain with a 6.25 GHz low-pass filter to demonstrate the potential for bandwidth reduction. In the signal reconstruction step, both complex slices were resampled and then frequency-shifted to the original center frequencies of the slice ($\pm$6.25 GHz).

In reconstruction, the phase and amplitude mismatches between the slices were adaptively equalized with the optimized complex-valued weight through the radius-directed algorithm. This was followed by the frequency offset estimation and feedforward phase recovery to compensate for frequency offset and phase noise, respectively, prior to the BER measurement. To estimate the performance of the SSRx scheme, the author analyzes the sensitivity performance obtained with the LOs generated by the EO-OFC and the IL-GS OFC, respectively, and compares them with a conventional coherent receiver (LO, Δv=30 kHz).

Finally, the impact of CLSR variations on the SSRx performance was analyzed. In these and other reported experiments, the WSS passband was configured to a minimum width of approximately 10 GHz. To validate the impact of CLSR on a wider range of values, the author used the EO-OFC, where the CLSR can be easily varied by adjusting the RF amplitude driving the modulator and the passband frequency of the WSS filter.

Experimental Results: Receiver Sensitivity Performance

First, the receiver sensitivity performance results are discussed where the BER performance versus ROP for both detection schemes; conventional intradyne coherent receiver and SSRx that utilize both OFC variants are shown in Figure

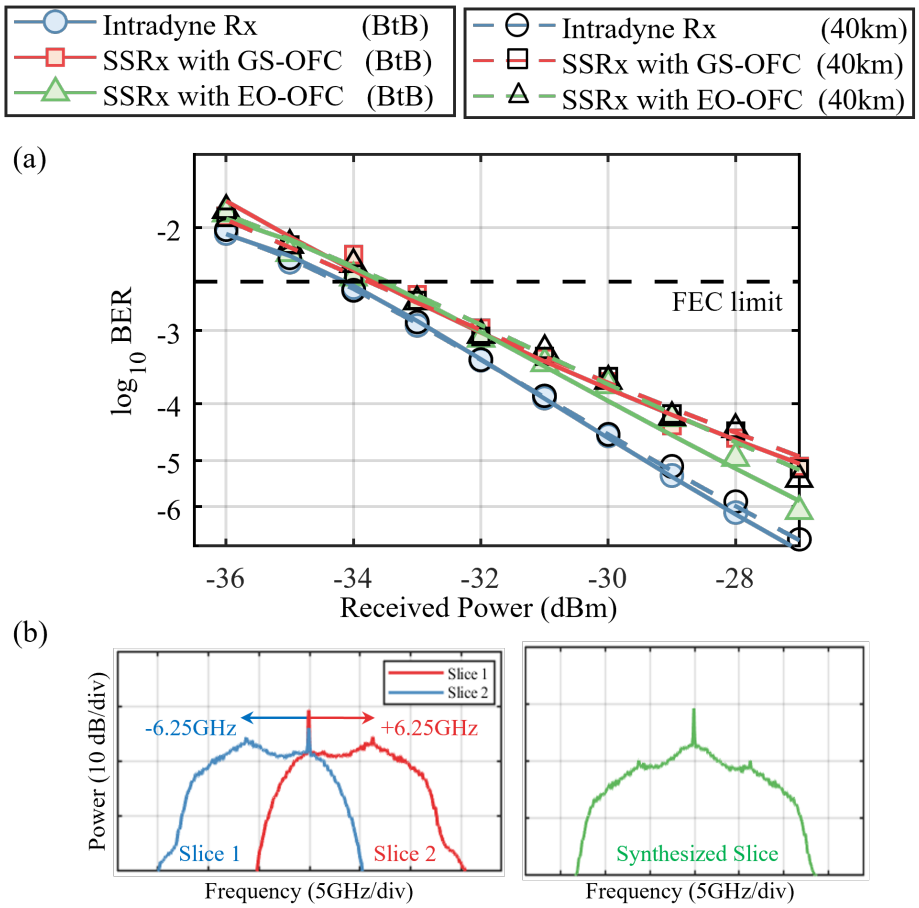


Figure 4.14: (a) Receiver power sensitivity performance of the conventional and proposed SSRx for 25 Gbaud QPSK signals. (b) Digitized and frequency-shifted by $\pm$ 6.25 GHz spectral slices (red, blue) and synthesized 25 Gbaud data signal (green) spectra.

4.14(a); for BtB and over the 40 km fiber link. For a fair comparison, the output power per comb line in the SSRx scheme is matched with the LO output power in the conventional receiver case. BER performance is very similar in all cases, although the SSRx cases show small sensitivity penalties of 0.5 dB (EO-OFC) and 0.9 dB (IL-GS OFC) at the FEC limit, compared to the conventional receiver.

The small additional 0.4 dB penalty in the IL-GS OFC case, compared to the EO-OFC scheme, is due to the lower CLSR of each demultiplexed comb line. The results for 40 km fiber and BtB transmissions are very similar, indicating that the sliced signal reconstruction does not significantly affect the performance of the dispersion equalizers. The spectra in Figure 4.14(b) illustrate the signal reconstruction process, showing the digitized frequency-shifted sliced signals corresponding to the spacing of the comb lines (left) and the reconstructed spectrum after the stitching process (right).

Experimental Results: CLSR Performance

To gain further insight into the effectiveness of signal reconstruction with varying CLSR, the SSRx sensitivity with different pairs of IL-GS comb lines was evaluated. For a fair comparison, the LO power per comb line was fixed at the same power in each case using EDFA and VOA in the experiment. However, since the IL-GS OFC has non-zero comb flatness, this leads to CLSR after demultiplexing that varies from line to line. The results are shown in Figure 4.15(a). The measured SSRx sensitivity varies from −33 to −31 dBm across the four sets of pair combs,

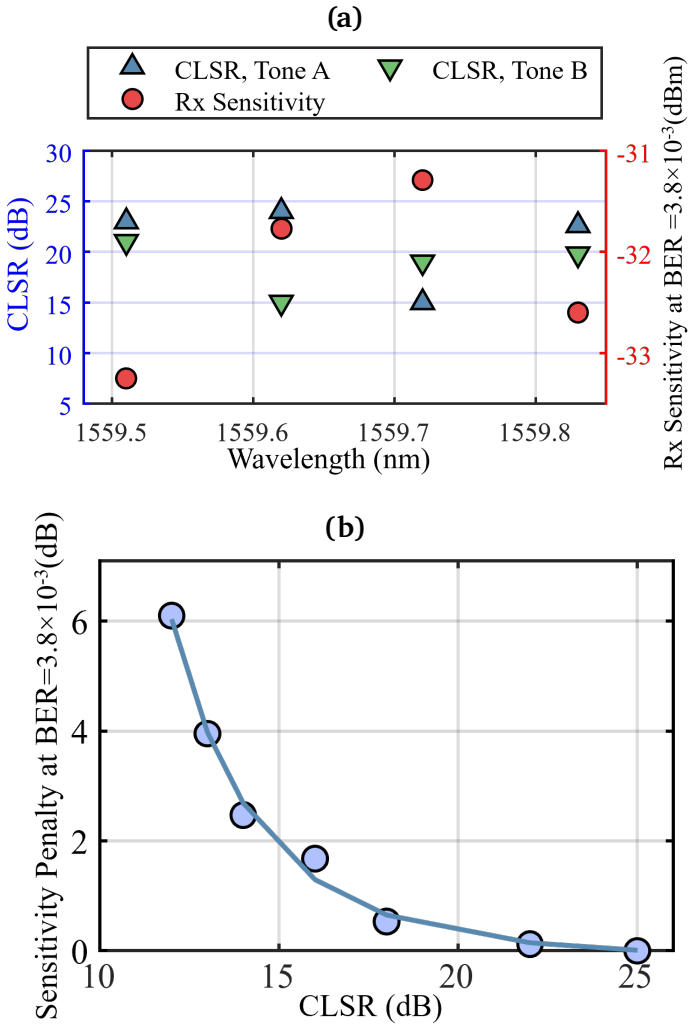


Figure 4.15: (a) Measured receiver sensitivity performance of the SSRx obtained with the IL-GS OFC. The red marker (right y-axis) represents the measured receiver sensitivity of the SSRx for four sets of comb pairs, while the CLSR measured for the demultiplexed comb tones in each pair is represented by the blue and green markers (left y-axis). (b) Sensitivity penalty measured versus CLSR of SSRx obtained with EO-OFC.

as shown by the red points. The CLSR values for each comb tone are also shown, and it can be seen that when the CLSR of one or both tones are low, the receiver sensitivity is correspondingly low.

To further quantify and explain this effect, the sensitivities of the SSRx were evaluated using the EO-OFC with different values of CLSR obtained by adjusting the modulator drive conditions. The EO-OFC was used for this experiment, as higher maximum CLSR values could be obtained compared to the IL-GS OFC, allowing a sweep from the zero- to large-sensitivity penalty limits. As shown by the results in Figure 4.15(b), for a penalty of less than 0.5 dB, the allowed CLSR for both demultiplexed lines should be 20 dB or higher, in good agreement with the modeling results shown in Figure 4.8(a). This explains the variation in the SSRx sensitivity measured with different pairs of IL-GS OFC comb lines shown in Figure 4.15(a). In particular, the pairs of the 2nd and 3rd comb lines degrade the sensitivity of SSRx by approximately 2 dB compared to the best sensitivity case obtained for the pair of the 1st comb line. The performance of the SSRx utilizing the IL-GS OFC in Figure 4.14(a) was obtained using this best-case pair, for which the minimum CLSR was approximately 21 dB(tone B).

In comparison, the CLSR of the EO-OFC was 25 dB for this experiment. As mentioned in the previous Section 4.3.2,the linewidths of the EO-OFC and IL-GS combs are both sufficiently narrow so as not to cause any significant degradation of the transmitted signal for this modulation format and baud rate range. Therefore, the additional 0.4 dB penalty observed for IL-GS OFC-based SSRx can be explained by the poorer CLSR compared to EO-OFC. This CLSR was limited by the minimum filter width of the WSS used in the experiments and can be easily improved by using alternative de-multiplexers, such as active solutions, presented in the next section, which not only improves the side tone rejection ratio, but also provides amplification, noise reduction, and gain flattening [94].

4.4 Integrated Comb Laser Assembly (iCLA)

4.4.1 PIC System Design

The use of PIC technology has driven massive savings in cost, form factor, and power consumption for optical transceivers to the point that it is now feasible to consider the potential use of PICs to enable future coherent PONs. Hence, this work also explores some of the key sub-components and integration approaches that would be needed to achieve this goal. Specifically, in partnership with Pilot Photonics, we have researched integrated optical frequency comb and comb de-multiplexer PIC designs and assessed their performance in the SSRx context. Such PIC-based transceiver solutions have the potential to drive down costs to the levels required for PON applications. To the best of our knowledge, this is the first investigation of this type in the context of spectrally sliced communications aimed at future PON applications.

The integrated comb laser assembly (iCLA) is a fully packaged, monolithically integrated comb laser and de-multiplexer capable of generating four mutually coherent lines and routing them to the LO ports of different coherent receivers, which is shown in Figure 4.16. In this version, the iCLA consists of an expanded optical frequency comb PIC (e-comb) and an all-active 4-channel de-multiplexer PIC. The e-comb PIC is based on the gain-switching of two wavelength-shifted secondary lasers that are simultaneously externally injected by a single-mode primary laser. This creates two mutually locked and phase-correlated combs. When these are combined, an expanded comb result is produced by the overlap and combination of the independent combs. The e-comb PIC has an on-chip low-linewidth internal primary laser. However, due to the mismatch of the lasing

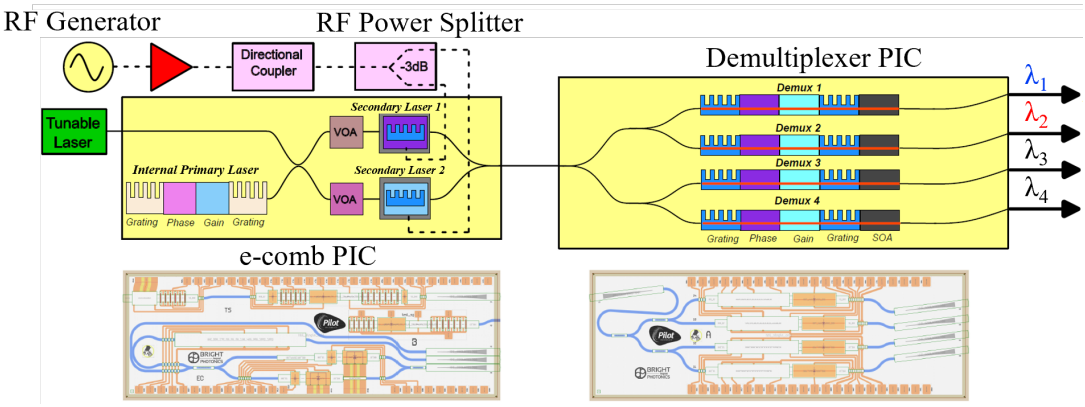


Figure 4.16: The schematic and fabricated PIC layout of both comb source and de-multiplexer respectively.

wavelengths of the internal primary laser and the secondary lasers, an external low linewidth (<30 kHz) C-band tunable laser is used as the primary laser.

The ability to use the OFC as an LO for the coherent receiver is based on the availability of the de-multiplexer capable of separating closely spaced lines while introducing low insertion losses. In the context of an integrated platform, conventional de-multiplexers, such as AWGs, are generally difficult to fabricate with low footprint and sufficient spectral accuracy and adjacent channel crosstalk suppression in the narrow comb line spacing limit required for the PON application that this thesis targets. As mentioned above, a more suitable solution to this problem involves using filters based on InP or Si_4N_3. An InP-based active de-multiplexer was chosen because it provides the required selectivity and ultra-low noise amplification [94]. In this iCLA, the expanded-comb PIC is followed by a de-multiplexer PIC.

The design of the de-multiplexer PIC is a cascade of multimode interferometers (MMI) that split an input signal and couple it to an array of four single-mode injection-locked lasers to demultiplex the desired comb tones. The tones are then amplified and routed to four independent PIC outputs. As a result, it overcomes one of the main drawbacks of an OFC, namely low comb-line power. As shown in Figure 4.17(b), despite the power losses introduced by the 1×4 splitting waveguide, the power measured from the demultiplexed comb lines is approximately 0 dBm. Furthermore, the ability of the de-multiplexer to suppress closely spaced adjacent lines is desirable in the context of an SSRx for efficient reconstruction performance as highlighted in the previous demonstration. As shown in Figure 4.17(b), the two demultiplexed lines have a CLSR of more than 30 dB, which is sufficient for negligible penalty impact on the slice reconstruction process.

4.4.2 Module Characterization

Apart from its integration-enabled, cost-effectiveness, and stability, one of the main advantages of this comb architecture is its ability to achieve a low effective linewidth per tone, only restricted by the primary laser used in the comb source. Therefore, phase noise measurements are performed based on a modified delayed self-heterodyne technique presented in the Chapter 2 to characterize the FM-noise spectrum of each tone. Figure 4.17(a) shows the FM noise spectrum of the output tone generated from the proposed comb source, which appears to give an effective linewidth measurement of approximately 30 kHz, similar to the linewidth measurement of the internal primary laser. Subsequently, the two de-

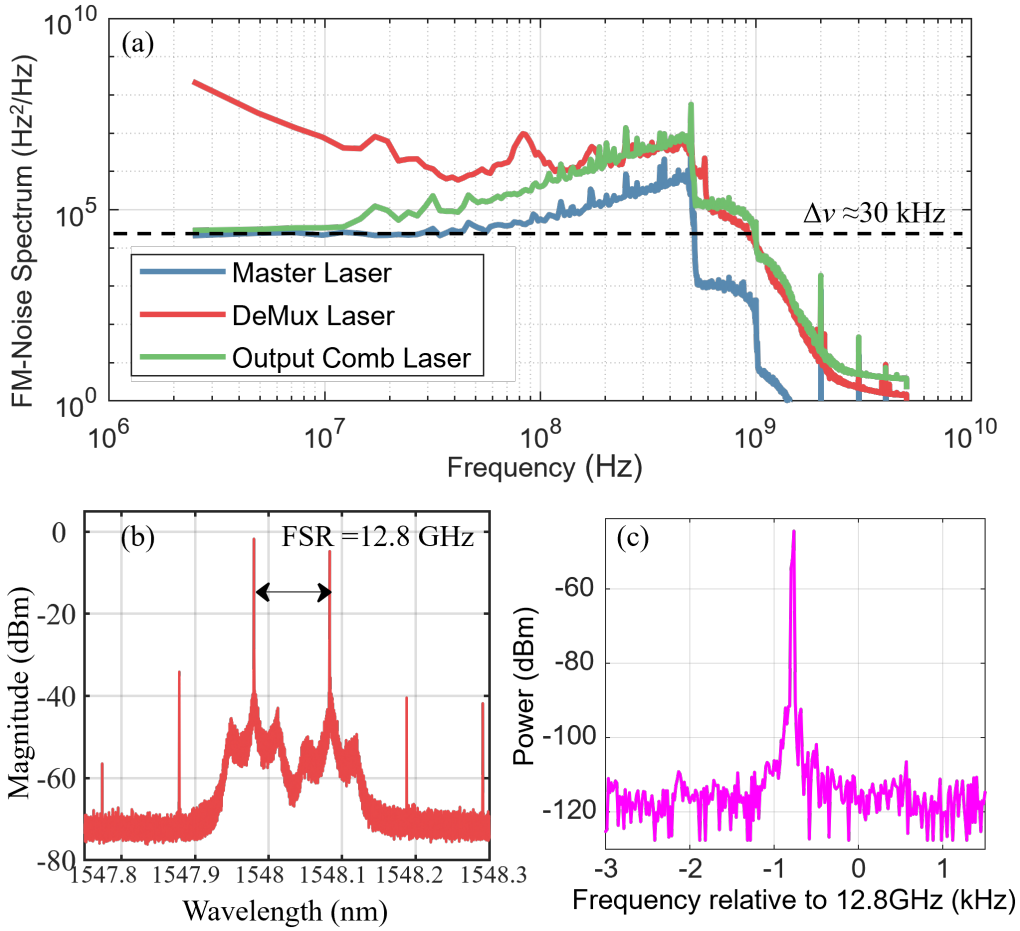


Figure 4.17: (a) Phase noise measurements comparing the comb signal with the primary laser, (b) optical spectrum of the output comb signals with frequency spacing of 12.8 GHz and each having CLSR of more than 30 dB, (c) resultant beating tone between the two output tones generated at a frequency of 12.8 GHz.

multiplexed tones, separated by a 12.8 GHz spacing, as shown in Figure 4.17(b), were mixed to measure the phase correlation properties between the comb tones. The result is plotted in Figure 4.17(c), showing the 3-dB beat linewidth of <1kHz, indicating the strong phase correlation between OFC tones even when demultiplexed. These low linewidths and high degrees of phase coherence properties across the comb tones make them highly suitable for optimized signal reconstruction in an SSRx including enabling the use of higher-order modulation formats for high-bit-rate transmission. Such as studied in the previous Section 4.2.2, 16QAM modulation format can be employed with 30 kHz linewidth to achieve 4 bits per symbol in the transmission system.

4.4.3 Demonstration of an SSRx Utilizing an iCLA

Experimental Setup

The experimental setup is illustrated in Figure 4.18(a). The 25 Gbaud signal, spectrally shaped with a raised cosine filter with a roll-off factor of 0.1 was generated by four channels of DAC driven at 50 GSa/s and amplified by RF amplifiers. These analog and electrical signals drive an optical coherent transmitter module comprised of a dual I-Q modulator that has a specified 6-dB bandwidth of 30 GHz, thus resulting in a dual polarization of 100 Gb/s signal. The transmitted carrier was derived from an ECL with a linewidth of 30 kHz operating at a wavelength of 1548.035 nm. The resulting optical spectrum of the transmitted signal is shown

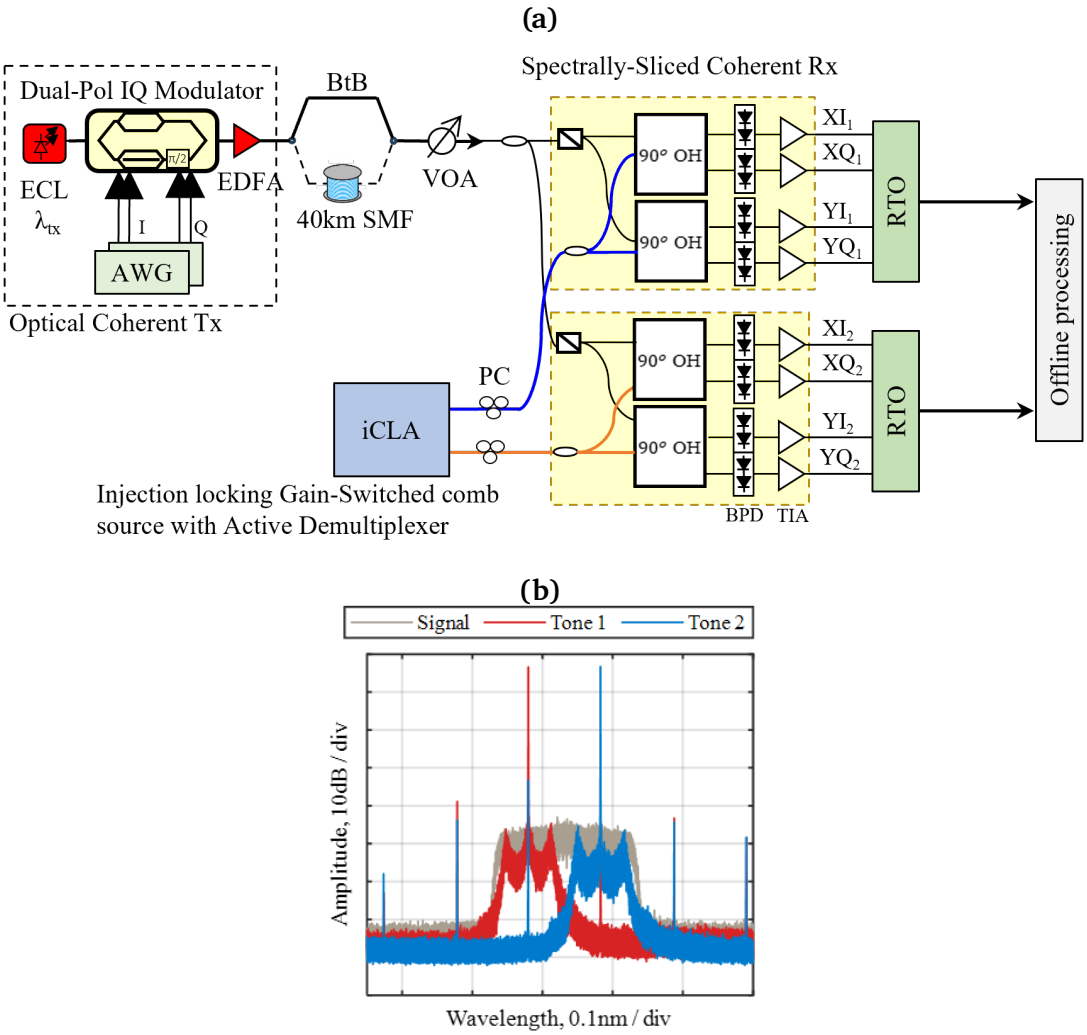


Figure 4.18: (a) Experimental setup for 100 Gb/s DP-QPSK with (N=2) SSRx utilizing iCLA. (b) optical spectrum of the transmitted 100 Gb/s signal with two demultiplexed comb lines which each directly mixing with portion spectrum of the received signal.

in Figure 4.18(b). The modulated optical signal was boosted by an EDFA before being launched either directly to the coherent receiver or to a 40 km SMF fiber spool. The ROP can be swept by adjusting the VOA.

For the conventional coherent detection scheme using a single integrated coherent receiver, another ECL with a wavelength close to that of the transmitter source was used as the LO. It was launched into a micro-integrated phase and polarization diversity coherent optical receiver (Fujitsu FIM24902) to mix with the signal. For the SSRx detection case, the associated LO tones were derived from the mutually injection-locked gain-switched laser with a line spacing of 12.8 GHz and a four-channel PIC-based active de-multiplexer, as described in the previous section. The optical receiver is configured with a parallel structure of two integrated phase- and polarization-diverse coherent receivers (FIM24902); each consists of two optical 90^o hybrids and two pairs of BPD and TIA. However, due to limited experimental resources, the author was only able to demonstrate $N=2$ spectral slicing, despite the iCLA being capable of generating four comb lines. Figure 4.18(b) shows the spectra of the generated filtered comb tones; each is then superimposed on the corresponding signal frequencies in the coherent receiver. The received waveforms are then captured using eight time-synchronous oscilloscope channels (Tektronix DPO77002SX) operating at 50 GSa/s for offline DSP. Before post-processing, each channel was deskewed based on pre-calibrated values to compensate for the timing delay between the acquisition channels.

The two complex inputs, corresponding to the slice 1 and slice 2 signals, were filtered by using a 4^{th} order low-pass Bessel filter with a 3-dB bandwidth of 6.4 GHz. This value was carefully chosen to ensure that the slices collectively captured the entire spectrum of the transmitted signal with minimal spectral gaps or overlaps. Following this, each slice was frequency-shifted by $\pm$6.4 GHz before the signal underwent reconstruction using a 4$\times$2 MIMO equalization, as detailed in Section 3.3.3; which compensated for the amplitude and phase mismatches between the two slices and demultiplexed the polarization of the X and Y tributaries. The filter coefficients were updated using a blind radius-directed equalization algorithm. After estimating and removing the frequency offset, a phase averaging based on the Viterbi-Viterbi algorithm was implemented to compensate for phase noise in the recovered signal. Finally, BER measurements were obtained through error counting after symbol decoding.

Experimental Result

The BER performance versus received optical power comparing the two receiver schemes, ICR and SSRx, utilizing the proposed comb (iCLA), are shown in Figure 4.19(a) for the 40 km SMF transmission cases. Since coherent sensitivity performance depends on the LO intensity, the LO output power is set to 0 dBm in the ICR scheme and is matched to the output power per comb line in the SSRx case. The 40 km fiber transmission constellation diagrams of the SSRx with iCLA signals are shown in Figure 4.19(b). There is a minimal difference (0.8 dB) penalty in receiver sensitivity between the SSRx and ICR case; this is important, as it shows that the requirements on receiver bandwidth can be relaxed for an SSRx that is utilized on PIC technology.

The receiver sensitivity is reduced by >3 dB compared to previous work pre-

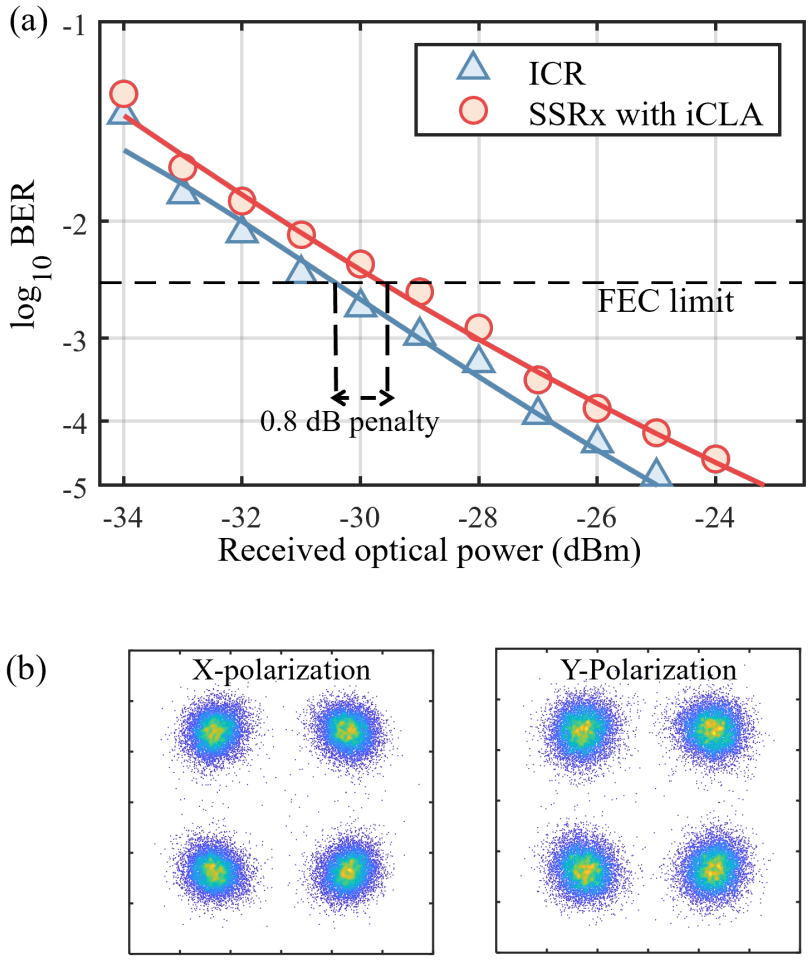


Figure 4.19: (a) 100 Gb/s DP-QPSK BER versus ROP performance over 40 km transmission distance. (b) Constellation diagram of SSRx captured at receive power of −20 dBm.

sented in Section 4.3.3. This reduction was mainly due to the reduced LO power, which is limited by the iCLA's capability. However, the iCLA is currently in an advanced prototype stage of development, so current performance is not necessarily representative of what is ultimately achievable with this technology. Nevertheless, it is worth mentioning that even at the currently achieved sensitivity level, 100G coherent PON operation would be possible with very modest and practical signal launch powers of +4dBm assuming a typical Class C 50G-PON link budget requirement (33 dB) [9].

Contributions

The impact of comb and de-multiplexer investigations and the demonstrations of SSRx with comb and de-mutiplexer PICs were presented and published as the following contributions:

- H. Othman, X. Ouyang, C. Anthony, F. Smyth, P.D. Townsend, 'Spectrally-Sliced Coherent Receiver Utilizing Gain-Switched Optical Frequency Comb,' in *Journal of Lightwave Technology*, vol. 41, no. 16, pp. 5262—5274, 2023
- H. Othman, X. Ouyang, G. Jain, D. Gutierrez-Pascual, C. Anthony, F. Smyth, P.D. Townsend, "Integrated Comb Laser with Active De-multiplexer for Spectrally Sliced Coherent Receiver," in *IEEE Photonics Technology Letters*, vol. 36, no. 12, pp. 787—790, 2024.
- H. Othman, X. Ouyang, C. Anthony, G.Jain, F. Smyth, P.D. Townsend, "Spectrally-Sliced Coherent Receivers for Cost-effective Coherent Access Network," in *2023 Photonics Ireland Conference*, Ireland, 2023.

4.5 Summary

In this chapter, the author discusses different types of OFCs with de-multiplexers, and their requirements for potential integration and optimized SSRx detection performance. The study presented in Section 4.2 presents the investigation of the impact of comb line power, phase noise, phase correlations, and comb line suppression ratio on the detection performance of an SSRx.

Section 4.3 explores the use of the IL-GS OFC for SSRx through an experimental demonstration of 25 Gbaud single polarization QPSK (50 Gb/s) signal transmission over 40 km of optical fiber. Due to the slightly low comb line suppression ratio (21 dB), the proposed receiver exhibits a small (less than 1 dB) sensitivity penalty compared to the conventional coherent receiver.

Section 4.4 demonstrates the potential for SSRx incorporating a comb source PIC and an active de-multiplexer PIC. After 40 km of fiber transmission, a close to theoretically-expected receiver sensitivity of -29 dBm was achieved, highlighting the excellent PIC performance (CLSR, linewidth, and output power) and the potential for PIC-based spectral slicing solutions enabling cost-saving bandwidth reduction for future coherent PON systems. Future work will focus on integrating the receiver's front-end with an OFC and a de-multiplexer, leading to a fully integrated SSRx.

Chapter 5

Conclusion & Future Work

5.1 Summary of Research

The advancement of DSP technology has led to the widespread adoption of digital coherent optics in modern telecommunications networks. This technology offers high receiver sensitivity and enables advanced modulation formats, benefiting high-speed optical communication systems. However, implementing coherent detection in future access networks, which emphasizes the cost, requires re-designing the conventional coherent receiver architecture.

Throughout the dissertation, the author proposed and investigated the potential of the spectral slicing technique to significantly reduce the bandwidths of the analog front-end components in a coherent receiver compared to a conventional receiver. The concept and method of the proposed receiver are outlined in Chapter 3. The potential for bandwidth reduction as low as 6.25 GHz was experimentally demonstrated through 50 Gb/s and 100 Gb/s signal transmission experiments over 40 km of optical fiber.

In Chapter 4, the author explored the potential of a comb source and a de-multiplexer for integration with an SSRx. The properties of these devices, such as spectral flatness, phase coherence, optical power per tone, and optical linewidth, as well as de-multiplexer imperfections such as the comb line suppression ratio and insertion losses, were analyzed in the context of spectrally sliced receiver system performance. An SSRx utilizing monolithically integrated gain-switched comb source and active de-multiplexer PICs was demonstrated to achieve 100 Gb/s signal transmission over 40 km fiber at a high receiver sensitivity of -29 dBm. To the best of the author's knowledge, this work represents the first spectral-

slicing demonstration utilizing a comb laser PIC and a novel active de-multiplexer PIC with specifications suitable for future PON applications.

Finally, the following section will discuss potential future research that could build upon the work described in this thesis and lead to further advances in the development of low-cost coherent optics based on the spectral-slicing technique for future coherent access networks.

5.2 Outlook & Future Work

5.2.1 Spectral Reconstruction based on the Channel Estimation

In the post-processing DSP, the author utilizes structured FIR filters with a MIMO configuration to equalize the amplitude and phase mismatches of the slices during the stitching process. The complexity of the filter increases in proportion to the discrepancies of the slice attributes, such as amplitude, phase, and polarization, particularly when dealing with a large number of slices. Therefore, it is crucial to consider the possibility of designing a channel estimation algorithm that is optimized and compatible with the reconstruction of the spectral slice. One potential algorithm involves the use of an orthogonal chirp division multiplexing (OCDM) signal, which allows chirped signals to overlap in both time and frequency domains to be used as a preamble frame to estimate the channel response (by extracting the channel impulse response of the received pilot) [101]. After recombining, the stitched chirped signals can be leveraged to equalize the stitched payload signal in the frequency domain. This algorithm has the potential to outperform the conventional equalization schemes when dealing with significant discrepancies between the slice signals and targeting a higher number of slices, all while maintaining the relatively low complexity of DSP design.

5.2.2 Burst-Mode SSRx

In addition to cost, upstream burst detection is yet another major challenge for the deployment of coherent PON. As discussed in Chapter 3, the spectral slicing approach is potentially valuable in the context of burst-mode detection as high-commodity 10G-class burst-mode receiver component (BM-TIA) can be utilized and further adapted for coherent detection. However, the demonstration of such

a system would require further significant work from the design and development of the receiver circuit, in addition to appropriate burst mode experimental testbeds. As for the frequency offset tolerance due to wavelength distinction between LO with different source signals, it is also crucial to address the offset tracking speed and explore novel methods to tune the LO (comb source) laser fast enough within the burst preamble time.

5.2.3 Higher Scalability of SSRx, $N=4$

Throughout this thesis, the author demonstrates the parallelization in the SSRx based on a two-slice operation. With access to a larger number of receiver channels, facilitated by photonic integration to reduce the testbed complexity, the scheme can be extended to a four-spectral slice operation. Furthermore, in this case the required bandwidth of the optical and electrical components in the receiver front-end (such as BPD, TIA, ADC) can be reduced by a factor of four. For example, a 200 Gb/s optical transmission system with $N=4$ slices could be realized with an integrated comb laser assembly similar to the one demonstrated in Chapter 4). The experimental setup can be built and tested at the Tyndall National Institute with access to eight-channel synchronized oscilloscopes operating at 100 GSa/s. This receiver architecture is visualized in Figure 5.1, for the case of $N=4$.

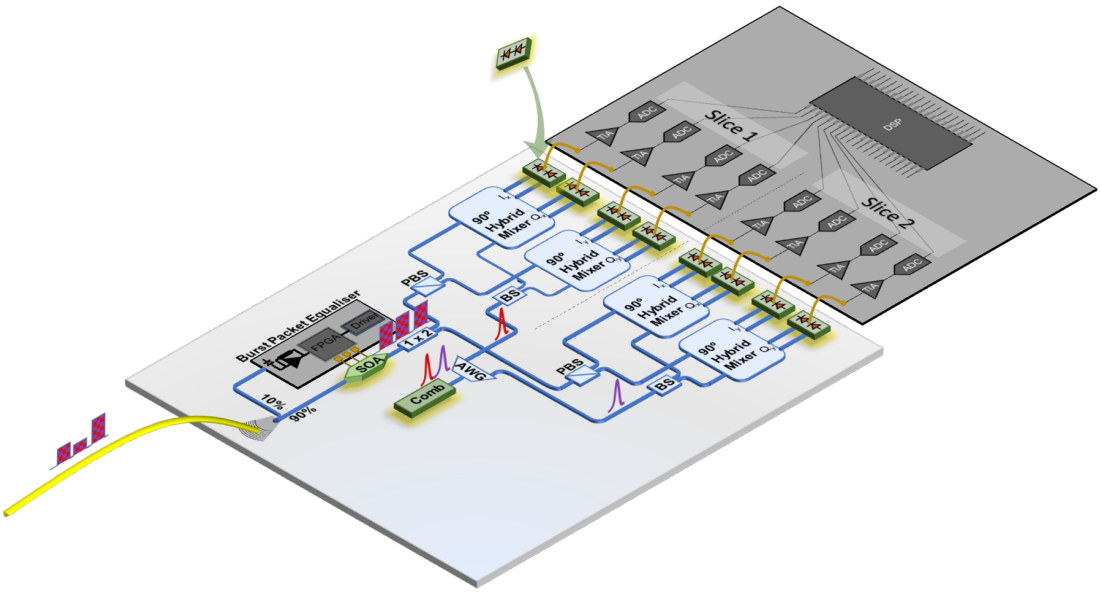


Figure 5.1: Schematic of an integrated spectrally sliced coherent receiver ($N=4$) envisioned for PON upstream transmission.

5.2.4 Fully-PIC SSRx Demonstration

Chapter 4 demonstrates an SSRx incorporating an optical frequency comb and active de-multiplexer PICs. Looking at the later stage of spectrally sliced development for a low-cost solution in coherent PON, it would be ideal to demonstrate the whole optical receiver circuit, including the comb source, in a hybrid chip-scale module or assemblies. The device, along with the comb source, is targeted for development at the Tyndall National Institute within the Science Foundation Ireland-funded IPIC Research Centre program.

Recent research on the spectral slicing scheme have demonstrated four slicing front-ends on a compact silicon photonic chip [58]. Although this work aims towards THz signal acquisition, it does give further evidence of the feasibility of parallelization on this scale using PIC technology. Additionally, as discussed earlier, it should also be noted that the dominant cost of an integrated circuit is mainly limited by the electrical bandwidth of the constituent components [48]. In other words, in terms of overall cost, the lower bandwidth requirements can more than compensate for having doubled or more the component count in the PIC platform. From a practical perspective, the integration of the SSRx would also reduce the number of optic/optic and optic/electronic interfaces, hence reducing experimental testbed complexities and enabling new experimental research avenues to be pursued, as well as addressing cost-effective solutions for optical transceivers.

5.2.5 Spectrally Sliced System, Tx with Rx

So far in this thesis work, the author has shown the feasibility of a spectrally sliced approach on the receiver side. The same principle can also be applied to the transmitter, where the low bandwidth of the DAC array and the I-Q modulators can be employed to transmit a single broad bandwidth optical signal. The initial design of this proposed approach can be illustrated in Figure 5.2, where a four-slice operation, $N=4$ is implemented, which includes four I-Q modulators structured in a parallel configuration.

Four generated tones from an OFC are separated and the power equalized by using ring resonators, which can be efficiently implemented in a silicon photonics platform. Each comb tone (having excellent phase-matched properties) is then modulated individually by the I-Q modulator, driven by a low-bandwidth DAC. This results in four tributary signals (slices) merged by a signal-combining

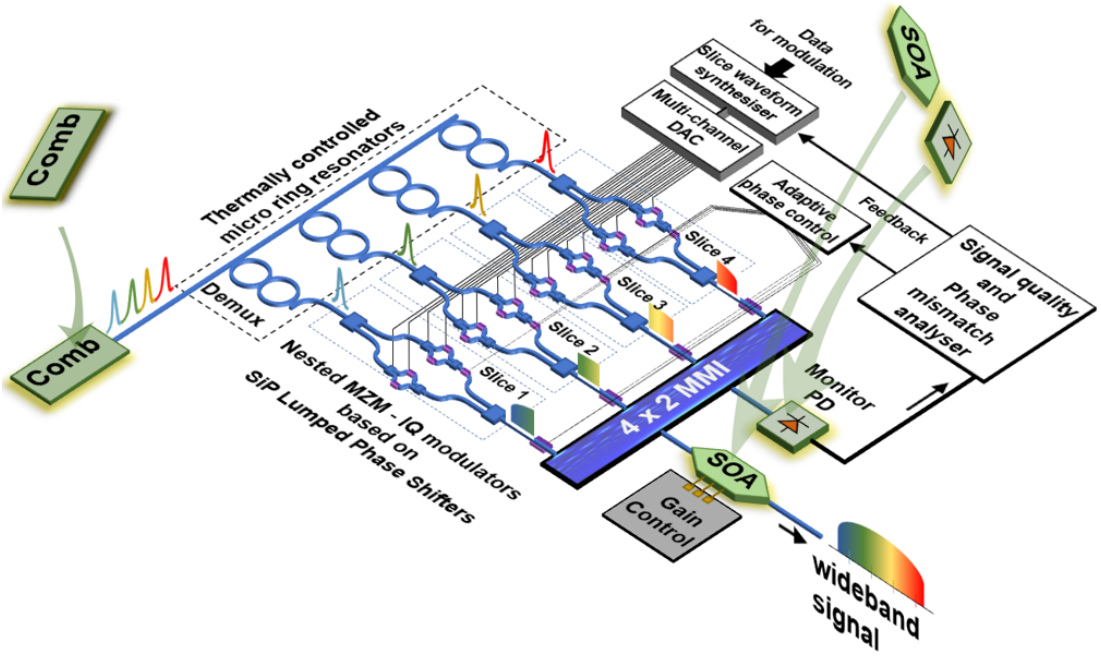


Figure 5.2: Proposed schematic design of a photonic integrated spectrally sliced coherent transmitter (N=4). SiP: silicon photonic; SOA: semiconductor optical amplifier.

element, in this example, via a multimode interferometer. For stabilizing the amplitude and phase of each slice prior to combining, the MMI output is routed to a photodiode to detect the amplitude or phase error signal generated by the interference of the overlapping spectral component of the slices. An adaptive feedback control can be implemented using DSP to compensate for waveform distortions, thus enabling the transmission of a stable and coherent wideband signal.

Although wideband waveform generation and detection based on the spectral slicing technique has been demonstrated in several institutions aiming at THz transmission systems [102–104], the proposed work here focuses on highlighting the spectral slicing technique specifically as a potentially cost-effective solution for coherent PON, which is currently targeting line rates of 100 Gb/s and beyond. In general, the spectral slicing system provides a potentially cost-effective solution for implementing a coherent system if appropriate PIC technology leveraging high-volume and low-bandwidth commodity components can be realized.

References

[1] "Data Never Sleeps 6.0," 2018. [Online]. Available: https://www.domo.com/learn/infographic/data-never-sleeps-6.

[2] S. Morgan and S. Arcserve, "The 2020 Data Attack Surface Report," Nov. 2020. [Online]. Available: https://cybersecurityventures.com/wp-content/uploads/2020/12/ArcserveDataReport2020.pdf.

[3] "Telegeography Global Internet Map 2021," 2021. [Online]. Available: https://global-internet-map-2021.telegeography.com/.

[4] J. M. Senior, *Optical Fiber Communications Principles and Practice*. Pearson Education, 3rd ed., 2009.

[5] C. Żukowski, A. Mukhopadhyay, D. B. Payne, and M. Ruffini, "Cost Analysis of Rural Roll-Out Using a Long-Reach Passive Optical Network: Trading Off the Upfront Cost under Uncertainty of the User Take-up Rate," *Journal of Optical Communications and Networking*, vol. 13, pp. 69–84, May 2021.

[6] E. Gronvall, *A Comprehensive Guide to Next Gen PON Decisions*. CommScope, Dec. 2021.

[7] J. Zhang and Z. Jia, "Coherent Passive Optical Networks for 100G/λ-and-Beyond Fiber Access: Recent Progress and Outlook," *IEEE Network*, vol. 36, pp. 116–123, Mar. 2022.

[8] J. Keaney, "Why 10 Gigabits, Why Now?," Oct. 2022. [Online]. Available: https://siro.ie/news-and-insights/why-10-gigabits-why-now/.

[9] ITU-T Recommendation G.9804.3, "50-Gigabit-capable passive optical networks (50G-PON): Physical media dependent (PMD) layer specification," 2021. [Online]. Available: https://www.itu.int/rec/T-REC-G.9804.3-202109-I.

[10] P. Torres-Ferrera, F. Effenberger, M. S. Faruk, S. J. Savory, and R. Gaudino, "Overview of High-Speed TDM-PON Beyond 50 Gbps per Wavelength using Digital Signal Processing [Invited Tutorial]," *Journal of Optical Communications and Networking*, vol. 14, no. 12, pp. 982–996, 2022.

[11] "PON Transmission Technologies above 50 Gb/s per Wavelength," 2023. [Online]. Available: https://www.itu.int/ITU-T/workprog/wp-item.aspx?isn=18554.

[12] I. B. Kovacs, M. S. Faruk, P. Torres-Ferrera, and S. J. Savory, "Simplified Coherent Optical Network Units for Very-High-Speed Passive Optical Networks," *Journal of Optical Communications and Networking*, vol. 16, pp. C1–C10, July 2024.

[13] G. Rizzelli, M. Casasco, A. Pagano, V. Ferrero, and R. Gaudino, "Experimental Demonstration of In-Field 400G Coherent Metro-Access Convergence," in *2024 Optical Fiber Communications Conference and Exhibition (OFC)*, pp. 1–3, Mar. 2024.

[14] H. Sun, K.-T. Wu, and K. Roberts, "Real-Time Measurements of a 40 Gb/s Coherent System," *Optics Express*, vol. 16, pp. 873–879, Jan. 2008.

[15] P. J. Winzer, "Beyond 100G Ethernet," *IEEE Communications Magazine*, vol. 48, pp. 26–30, July 2010.

[16] "Verizon Deploys Commercial 100G Ultra-Long-Haul Optical System on Portion of Its Core European Network," Dec. 2009. [Online]. Available: https://www.verizon.com/about/news/press-releases/verizon-deploys-commercial-100g-ultralonghaul-optical-system-portion-its-core-european-network.

[17] "Optical Connections Magazine Autumn 2023," Nov. 2023. [Online]. Available: https://online.flippingbook.com/view/1013493939/24/.

[18] "Optical Internetworking Forum Implementation Agreement 400ZR," Mar. 2020. [Online]. Available: https://www.oiforum.com/wp-content/uploads/OIF-400ZR-01.pdf.

[19] Luis Alberto Campos and J. Zhensheng, *Coherent Optics for Access Networks*. CRC Press, 1st ed., 2019.

[20] "OFC 2024: Coherent PON, Multicore Fibre and Quantum Networking Amongst Hottest Topics." [Online]. Available: https://www.fibre-

systems.com/article/coherent-pon-multicore-fibre-quantum-networking-amongst-ofc-hot-topics.

[21] D. Lavery, T. Gerard, S. Erkılınç, Z. Liu, L. Galdino, P. Bayvel, and R. I. Killey, "Opportunities for optical access network transceivers beyond OOK," *Journal of Optical Communications and Networking*, vol. 11, no. 2, pp. A186–A195, 2018.

[22] V. Houtsma, A. Mahadevan, N. Kaneda, and D. van Veen, "Transceiver technologies for passive optical networks: past, present, and future [invited tutorial]," *Journal of Optical Communications and Networking*, vol. 13, no. 1, pp. A44–A55, 2020.

[23] X. Li, M. S. Faruk, and S. J. Savory, "Bidirectional Symmetrical 100 Gb/s/λ Coherent PON Using a Simplified ONU Transceiver," *IEEE Photonics Technology Letters*, vol. 34, pp. 838–841, Aug. 2022.

[24] J. Zhang, Z. Dong, J. Yu, N. Chi, L. Tao, X. Li, and Y. Shao, "Simplified Coherent Receiver with Heterodyne Detection of Eight-channel 50 Gb/s PDM-QPSK WDM Signal After 1040 km SMF-28 Transmission," *Optics Letters*, vol. 37, pp. 4050–4052, Oct. 2012.

[25] S. Arafin and L. A. Coldren, "Advanced InP Photonic Integrated Circuits for Communication and Sensing," *IEEE Journal of Selected Topics in Quantum Electronics*, vol. 24, pp. 1–12, Jan. 2018.

[26] C. Doerr and L. Chen, "Silicon Photonics in Optical Coherent Systems," *Proceedings of the IEEE*, vol. 106, pp. 2291–2301, Dec. 2018.

[27] Infinera, "Solution Brief, XR Optics: Innovative Point-to-Multipoint Coherent that Slashes Aggregation Network TCO," 2022. [Online]. Available: https://www.infinera.com/innovation/xr-optics/.

[28] D. Welch, A. Napoli, J. Back, S. Buggaveeti, C. Castro, A. Chase, X. Chen, V. Dominic, T. Duthel, T. A. Eriksson, S. Erkilinc, P. Evans, C. R. S. Fludger, B. Foo, T. Frost, P. Gavrilovic, S. J. Hand, A. Kakkar, A. Kumpera, V. Lal, R. Maher, F. Marques, F. Masoud, A. Mathurmember, R. Milano, M. I. Olmedo, M. Olson, D. Pavinski, J. Pedro, A. Rashidinejad, P. Samra, W. Sande, A. Somani, H. Sun, N. Swenson, H.-S. Tsai, A. Yekani, J. Zhang, and M. Ziari, "Digital Subcarrier Multiplexing: Enabling Software-Configurable Optical Networks," *Journal of Lightwave Technology*, pp. 1–18, 2022.

[29] M. S. Professor and J. Proakis, *Digital Communications*. McGraw-Hill Education, 5th ed., Nov. 2007.

[30] Optical InternetWorking Forum, OIF, "Implementation Agreement for Integrated Coherent Transmit-Receive Optical Sub Assembly," Aug. 2019. [Online]. Available: https://www.oiforum.com/wp-content/uploads/OIF-HB-CDM-02.0.pdf.

[31] Optical InternetWorking Forum, OIF, "Implementation Agreement for Micro Intradyne Coherent Receivers," June 2017. [Online]. Available: https://www.oiforum.com/wp-content/uploads/2019/01/OIF-DPC-MRX-02.0.pdf.

[32] ITU-T Recommendation G.652, "Characteristics of a Single-Mode Optical Fibre and Cable," Nov. 2016. [Online]. Available: https://www.itu.int/rec/T-REC-G.652-201611-I/en.

[33] G. P. Agrawal, *Nonlinear Fiber Optics*. Academic Press, Oct. 2012.

[34] G. P. Agrawal, *Fiber-Optic Communication Systems*. Wiley & Sons, 2010.

[35] K. Kikuchi, "Fundamentals of Coherent Optical Fiber Communications," *Journal of Lightwave Technology*, vol. 34, pp. 157–179, Jan. 2016.

[36] S. Camatel and V. Ferrero, "Narrow Linewidth CW Laser Phase Noise Characterization Methods for Coherent Transmission System Applications," *Journal of Lightwave Technology*, vol. 26, pp. 3048–3055, Sept. 2008.

[37] T. N. Huynh, L. Nguyen, and L. P. Barry, "Phase noise characterization of SGDBR lasers using phase modulation detection method with delayed self-heterodyne measurements," *Journal of Lightwave Technology*, vol. 31, pp. 1300–1308, Apr. 2013.

[38] M. G. Taylor, "Phase estimation methods for optical coherent detection using digital signal processing," *Journal of Lightwave Technology*, vol. 27, no. 7, pp. 901–914, 2009.

[39] A. Kakkar, J. Rodrigo Navarro, R. Schatz, X. Pang, O. Ozolins, A. Udalcovs, H. Louchet, S. Popov, and G. Jacobsen, "Laser Frequency Noise in Coherent Optical Systems: Spectral Regimes and Impairments," *Scientific Reports*, vol. 7, p. 844, Apr. 2017.

[40] M. Kuschnerov, K. Piyawanno, M. S. Alfiad, B. Spinnler, A. Napoli, and B. Lankl, "Impact of Mechanical Vibrations on Laser Stability and Car-

rier Phase Estimation in Coherent Receivers," *IEEE Photonics Technology Letters*, vol. 22, pp. 1114–1116, Aug. 2010.

[41] H. Kiwata, M. Kikuta, M. Shigihara, and K. Igarashi, "Ultra-long-time (0.8 s) characterization of laser phase noise with high temporal resolution (800 ps) based on heterodyne reception with FPGA data acquisition," in *2020 European Conference on Optical Communications (ECOC)*, pp. 1–4, Dec. 2020.

[42] I. Fatadin, S. J. Savory, and D. Ives, "Compensation of Quadrature Imbalance in an Optical QPSK Coherent Receiver," *IEEE Photonics Technology Letters*, vol. 20, pp. 1733–1735, Oct. 2008.

[43] A. Leven, N. Kaneda, U.-V. Koc, and Y.-K. Chen, "Frequency Estimation in Intradyne Reception," *IEEE Photonics Technology Letters*, vol. 19, pp. 366–368, Mar. 2007.

[44] A. J. Viterbi and A. M. Viterbi, "Nonlinear Estimation of PSK-Modulated Carrier Phase with Application to Burst Digital Transmission," *IEEE Transactions on Information Theory*, vol. 29, pp. 543–551, July 1983.

[45] F. Chang, K. Onohara, and T. Mizuochi, "Forward Error Correction for 100G Transport Networks," *IEEE Communications Magazine*, vol. 48, pp. S48–S55, Mar. 2010.

[46] Y. Zhu, L. Yi, B. Yang, X. Huang, J. S. Wey, Z. Ma, and W. Hu, "Comparative Study of Cost-Effective Coherent and Direct Detection Schemes for 100 Gb/s/λ PON," *Journal of Optical Communications and Networking*, vol. 12, no. 9, pp. D36–D47, 2020.

[47] ITU-T Recommendation G.984.1, "Gigabit-capable Passive Optical Networks (GPON): General Characteristics," March 2008. [Online]. Available: https://www.itu.int/rec/T-REC-G.984.1-200803-I/.

[48] W. Shieh, C. Sun, and H. Ji, "Carrier-assisted differential detection," *Light Science & Application*, vol. 9, p. 18, Feb. 2020.

[49] N. K. Fontaine, R. P. Scott, L. Zhou, F. M. Soares, J. P. Heritage, and S. J. B. Yoo, "Real-time Full-Field Arbitrary Optical Waveform Measurement," *Nature Photonics*, vol. 4, no. 4, pp. 248–254, 2010.

[50] C. Zhang, Y. Mori, K. Igarashi, K. Katoh, and K. Kikuchi, "Ultrafast Digital Coherent Receiver Based on Parallel Processing of Decomposed Frequency

Subbands," in *36th European Conference and Exhibition on Optical Communication (ECOC)*, pp. 1–3, 2010.

[51] J. C. M. Diniz, F. D. Simoes, V. N. Rozental, S. M. Rossi, A. Chiuchiarelli, J. R. F. Oliveira, A. C. Bordonalli, and J. D. Reis, "Digital Signal Processing for Spectrally-Sliced Coherent Optical Receivers," in *41st European Conference and Exhibition on Optical Communication (ECOC)*, pp. 1–3, 2015.

[52] L. L. G. Gao, "Photonics-based broadband RF spectrum measurement with sliced coherent detection and spectrum stiching technique," *IEEE Photonics Journal*, vol. 9, no. 5, pp. 1–11, 2017.

[53] A. B. Stein and S. P. Volfbeyn, "Interleaved analog to digital converter with digital equalization," Sept. 2013. US8537044B2.

[54] J. Harris, "The ABCs of Interleaved ADCs," 2019. [Online]. Available: https://www.tek.com/en/documents/whitepaper/techniques-extending-real-time-oscilloscope-bandwidth.

[55] Tektronix, "Techniques for Extending Real-Time Oscilloscope Bandwidth," 2016. [Online]. Available: https://www.analog.com/media/en/technical-documentation/tech-articles/The-ABCs-of-Interleaved-ADCs.pdf.

[56] D. Fang, A. Zazzi, J. Müller, D. Drayss, C. Füllner, P. Marin-Palomo, A. Tabatabaei Mashayekh, A. Dipta Das, M. Weizel, S. Gudyriev, W. Freude, S. Randel, J. C. Scheytt, J. Witzens, and C. Koos, "Optical Arbitrary Waveform Measurement (OAWM) Using Silicon Photonic Slicing Filters," *Journal of Lightwave Technology*, vol. 40, pp. 1705–1717, Mar. 2022.

[57] N. K. Fontaine, T. Sakamoto, D. J. Geisler, R. P. Scott, B. Guan, and S. J. B. Yoo, "Coherent Reception of 80 GBd QPSK using Integrated Spectral Slice Optical Arbitrary Waveform Measurement," in *2012 Conference on Lasers and Electro-Optics (CLEO)*, pp. 1–2, Optica Publishing Group, May 2012.

[58] D. Drayss, D. Fang, C. Füllner, G. Lihachev, T. Henauer, Y. Chen, H. Peng, P. Marin-Palomo, T. Zwick, W. Freude, T. J. Kippenberg, S. Randel, and C. Koos, "Non-sliced optical arbitrary waveform measurement (OAWM) using soliton microcombs," *Optica*, vol. 10, pp. 888–896, July 2023.

[59] R. Proietti, C. Qin, B. Guan, N. K. Fontaine, S. Feng, A. Castro, R. P. Scott, and S. J. B. Yoo, "Elastic optical networking by dynamic optical arbitrary waveform generation and measurement," *Journal of Optical Communications and Networking*, vol. 8, pp. A171–A179, July 2016.

[60] K. Sozos, A. Bogris, P. Bienstman, G. Sarantoglou, S. Deligiannidis, and C. Mesaritakis, "High-Speed Photonic Neuromorphic Computing using Recurrent Optical Spectrum Slicing Neural Networks," *Communications Engineering*, vol. 1, pp. 1–10, Oct. 2022.

[61] A. Zazzi, J. Müller, S. Gudyriev, P. Marin-Palomo, D. Fang, J. C. Scheytt, C. Koos, and J. Witzens, "Fundamental limitations of spectrally-sliced optically enabled data converters arising from MLL timing jitter," *Optics Express*, vol. 28, pp. 18790–18813, June 2020.

[62] J. Sevenhans and Z.-Y. Chang, "A/D and D/A conversion for telecommunication," *IEEE Circuits and Devices Magazine*, vol. 14, pp. 32–42, Jan. 1998.

[63] I. Tomkos, A. Tolmachev, A. Agmon, M. Meltsin, T. Nikas, and M. Nazarathy, "Low-Cost/Power Coherent Transceivers for Intra-Datacenter Interconnections and 5G Fronthaul Links," in *21st International Conference on Transparent Optical Networks (ICTON)*, pp. 1–5, July 2019.

[64] B. S. G. Pillai, B. Sedighi, K. Guan, N. P. Anthapadmanabhan, W. Shieh, K. J. Hinton, and R. S. Tucker, "End-to-end energy modeling and analysis of long-haul coherent transmission systems," *Journal of Lightwave Technology*, vol. 32, no. 18, pp. 3093–3111, 2014.

[65] S.-Y. Kim, T. Suzuki, J.-I. Kani, and A. Otaka, "Coherent Receiver DSP Implemented on a General-Purpose Server for a Full Software-Defined Access System," *Journal of Optical Communications and Networking*, vol. 11, pp. A96–A102, Jan. 2019.

[66] P. Ossieur, N. A. Quadir, S. Porto, C. Antony, W. Han, M. Rensing, P. O'Brien, and P. D. Townsend, "A 10 Gb/s Linear Burst-Mode Receiver in 0.25 µm SiGe:C BiCMOS," *IEEE Journal of Solid-State Circuits*, vol. 48, pp. 381–390, Feb. 2013.

[67] T. Gurne, G. Coudyzer, B. V. Lombergen, R. Borkowski, M. Verplaetse, M. Straub, Y. Lefevre, P. Ossieur, R. Bonk, W. Coomans, X. Yin, and J. Maes, "First Demonstration of a 100 Gbit/s PAM-4 Linear Burst-Mode Transimpedance Amplifier for Upstream Flexible PON," in *2022 European Conference on Optical Communication (ECOC)*, pp. 1–4, Sept. 2022.

[68] J. Zhang, Z. Jia, M. Xu, H. Zhang, and L. Alberto Campos, "Efficient Preamble Design and Digital Signal Processing in Upstream Burst-Mode Detection of 100G TDM Coherent-PON," *Journal of Optical Communications and Networking*, vol. 13, pp. A135–A143, Feb. 2021.

[69] S. Xing, G. Li, A. Sun, J. Chen, Z. He, J. Zhang, and N. Chi, "Demonstration of PS-QAM Based Flexible Coherent PON in Burst-Mode With 300G Peak Rate and Ultra-Wide Dynamic Range," *Journal of Lightwave Technology*, vol. 41, pp. 1230–1239, Feb. 2023.

[70] D. Welch, A. Napoli, J. Back, W. Sande, J. Pedro, F. Masoud, C. Fludger, T. Duthel, H. Sun, S. J. Hand, T.-K. Chiang, A. Chase, A. Mathur, T. A. Eriksson, M. Plantare, M. Olson, S. Voll, and K.-T. Wu, "Point-to-multipoint optical networks using coherent digital subcarriers," *Journal of Lightwave Technology*, vol. 39, pp. 5232–5247, Aug. 2021.

[71] I. B. Kovacs, M. S. Faruk, and S. J. Savory, "Simplified Coherent Receivers for Passive Optical Networks," in *2023 European Conference on Optical Communications (ECOC)*, pp. 1182–1185, Oct. 2023.

[72] H. Othman, X. Ouyang, C. Antony, F. Smyth, and P. D. Townsend, "Spectrally-Sliced Coherent Receiver Utilizing a Gain-Switched Optical Frequency Comb," *Journal of Lightwave Technology*, vol. 41, no. 16, pp. 5262–5274, 2023.

[73] H. Othman, G. Jain, M. Deseada Gutierrez Pascual, X. Ouyang, C. Antony, F. Smyth, and P. D. Townsend, "Integrated Comb Laser With Active De-Multiplexer for Spectrally Sliced Coherent Receiver," *IEEE Photonics Technology Letters*, vol. 36, pp. 787–790, June 2024.

[74] M. Imran, P. M. Anandarajah, A. Kaszubowska-Anandarajah, N. Sambo, and L. Potí, "A Survey of Optical Carrier Generation Techniques for Terabit Capacity Elastic Optical Networks," *IEEE Communications Surveys and Tutorials*, vol. 20, no. 1, pp. 211–263, 2017.

[75] L. Lundberg, M. Mazur, A. Mirani, B. Foo, J. Schröder, V. Torres-Company, M. Karlsson, and P. A. Andrekson, "Phase-coherent lightwave communications with frequency combs," *Nature Communications*, vol. 11, no. 1, p. 201, 2020.

[76] C. Browning, D. Dass, P. Townsend, and X. Ouyang, "Orthogonal chirp-division multiplexing for future converged optical/millimeter-wave radio

access networks," *IEEE Access*, vol. 10, pp. 3571–3579, 2022.

[77] M. Mazur, M.-G. Suh, A. Fülöp, J. Schröder, V. Torres-Company, M. Karlsson, K. Vahala, and P. Andrekson, "High spectral efficiency coherent superchannel transmission with soliton microcombs," *Journal of Lightwave Technology*, vol. 39, no. 13, pp. 4367–4373, 2021.

[78] K. Kikuchi and S. Tsukamoto, "Evaluation of sensitivity of the digital coherent receiver," *Journal of Lightwave Technology*, vol. 26, no. 13, pp. 1817–1822, 2008.

[79] D. Nesset, "PON roadmap [invited]," *Journal of Optical Communications and Networking*, vol. 9, no. 1, pp. A71–A76, 2017.

[80] J. Hauck, A. Zazzi, A. Garreau, F. Lelarge, A. Moscoso-Mártir, F. Merget, and J. Witzens, "Semiconductor laser mode locking stabilization with optical feedback from a silicon PIC," *Journal of Lightwave Technology*, vol. 37, no. 14, pp. 3483–3494, 2019.

[81] J. Pfeifle, A. Kordts, P. Marin, M. Karpov, M. Pfeiffer, V. Brasch, R. Rosenberger, J. Kemal, S. Wolf, W. Freude, T. J. Kippenberg, and C. Koos, "Full C and L-Band Transmission at 20 Tbit/s Using Cavity-Soliton Kerr Frequency Combs," in *Conference on Lasers and Electro-Optics (CLEO)*, 2015.

[82] Y. Hu, M. Yu, B. Buscaino, N. Sinclair, D. Zhu, R. Cheng, A. Shams-Ansari, L. Shao, M. Zhang, J. M. Kahn, and M. Lončar, "High-efficiency and broadband on-chip electro-optic frequency comb generators," *Nature Photonics*, vol. 16, no. 10, pp. 679–685, 2022.

[83] M. D. G. Pascual, V. Vujicic, J. Braddell, F. Smyth, P. Anandarajah, and L. Barry, "Photonic integrated gain switched optical frequency comb for spectrally efficient optical transmission systems," *IEEE Photonics Journal*, vol. 9, no. 3, pp. 1–8, 2017.

[84] P. M. Anandarajah, R. Zhou, R. Maher, M. D. G. Pascual, F. Smyth, V. Vujicicand, and L. P. Barry, "Flexible Optical Comb Source for Super Channel Systems," in *Optical Fiber Communication Conference/National Fiber Optic Engineers Conference (OFC/NFOEC)*, 2013.

[85] J. Pfeifle, V. Vujicic, R. T. Watts, P. C. Schindler, C. Weimann, R. Zhou, W. Freude, L. P. Barry, and C. Koos, "Flexible Terabit/s Nyquist-WDM Super-Channels using a Gain-Switched Comb Source," *Optics Express*, vol. 23, no. 2, pp. 724–738, 2015.

[86] Z. Liu and R. Slavík, "Optical Injection Locking: From Principle to Applications," *Journal of Lightwave Technology*, vol. 38, pp. 43–59, Jan. 2020.

[87] G. Jain, D. Gutierrez-Pascual, M. J. Wallace, J. F. Donegan, and P. M. Anandarajah, "Experimental Investigation of External Optical Injection and its Application in Gain-Switched Wavelength Tunable Optical Frequency Comb Generation," *Journal of Lightwave Technology*, vol. 39, no. 18, pp. 5884–5895, 2021.

[88] V. Torres-Company, J. Schröder, A. Fulop, M. Mazur, L. Lundberg, O. B. Helgason, M. Karlsson, and P. A. Andrekson, "Laser Frequency Combs for Coherent Optical Communications," *Journal of Lightwave Technology*, vol. 37, pp. 1663–1670, Apr. 2019.

[89] P. D. Lakshmijayasimha, A. Kaszubowska-Anandarajah, S. Tajammul A., E. P. Martin, and P. M. Anandarajah, "Optical Linewidth Tolerant mmW Generation Employing a Dual-Stage Active Demultiplexer," *IEEE Photonics Technology Letters*, vol. 34, no. 9, pp. 451–454, 2022.

[90] M. Gutierrez, J. Braddell, F. Smyth, and L. Barry, "Monolithically Integrated 1x4 Comb De-multiplexer based on Injection Locking," in *18th European Conference on Integrated Optics (ECIO)*, May 2016.

[91] D. J. F. Barros, J. M. Kahn, J. P. Wilde, and T. A. Zeid, "Bandwidth-Scalable Long-Haul Transmission Using Synchronized Colorless Transceivers and Efficient Wavelength-Selective Switches," *Journal of Lightwave Technology*, vol. 30, pp. 2646–2660, Aug. 2012.

[92] M. Sharma and G. Cohen, "Wavelength Selective Switch," Oct. 2014. US8854597B2.

[93] P. D. Lakshmijayasimha, A. Kaszubowska-Anandarajah, E. P. Martin, M. N. Hammad, P. Landais, and P. M. Anandarajah, "Characterization of a Multifunctional Active Demultiplexer for Optical Frequency Combs," *Optics & Laser Technology*, vol. 134, p. 106637, Feb. 2021.

[94] A. Kaszubowska-Anandarajah, S. T. Ahmad, C. G. H. Roeloffzen, P. W. L. van Dijk, A. Sharma, M. Srivastava, P. D. Lakshmijayasimha, M. D. Gutierrez Pascual, F. Smyth, J. Braddell, and P. M. Anandarajah, "Reconfigurable Photonic Integrated Transmitter for Metro-Access Networks," *Journal of Optical Communications and Networking*, vol. 15, no. 3, pp. A92–A102, 2023.

[95] P. M. Anandarajah, R. Maher, Y. Q. Xu, S. Latkowski, J. O'Carroll, S. G. Murdoch, R. Phelan, J. O'Gorman, and L. P. Barry, "Generation of Coherent Multicarrier Signals by Gain Switching of Discrete Mode Lasers," *IEEE Photonics Journal*, vol. 3, no. 1, pp. 112–122, 2011.

[96] R. Lang, "Injection Locking Properties of a Semiconductor Laser," *IEEE Journal of Quantum Electronics*, vol. 18, pp. 976–983, June 1982.

[97] F. Mogensen, H. Olesen, and G. Jacobsen, "FM Noise Suppression and Linewidth Reduction in an Injection-Locked Semiconductor Laser," *Electronics Letters*, vol. 21, no. 16, p. 696, 1985.

[98] J. Wang, M. Haldar, L. Li, and F. Mendis, "Enhancement of Modulation Bandwidth of Laser Diodes by Injection Locking," *IEEE Photonics Technology Letters*, vol. 8, pp. 34–36, Jan. 1996.

[99] Pilot Photonics, "LYRA-OCS-1000, Optical Comb Laser Module," Sept. 2023. [Online]. Available: https://www.pilotphotonics.com/wp-content/uploads/2023/10/3.-Pilot-LYRA-OCS-1000-Flyer-Sept-2023.pdf.

[100] K. Zanette, J. C. Cartledge, and M. O'Sullivan, "Correlation Properties of the Phase Noise Between Pairs of Lines in a Quantum-Dot Optical Frequency Comb Source," in *2017 Optical Fiber Communications Conference and Exhibition (OFC)*, pp. 1–3, 2017.

[101] X. Ouyang, C. Antony, G. Talli, and P. D. Townsend, "Robust Channel Estimation for Coherent Optical Orthogonal Chirp-Division Multiplexing With Pulse Compression and Noise Rejection," *Journal of Lightwave Technology*, vol. 36, pp. 5600–5610, Dec. 2018.

[102] T. Henauer, A. Sherifaj, C. Füllner, W. Freude, S. Randel, T. Zwick, and C. Koos, "200 GBd 16QAM Signals Synthesized by an Actively Phase-Stabilized Optical Arbitrary Waveform Generator (OAWG)," in *Optical Fiber Communications Conference and Exhibition (OFC)*, pp. 1–3, Mar. 2022.

[103] B. Guan, N. K. Fontaine, R. Ryf, S. Chen, H. Chen, G. Raybon, C. Xie, R. P. Scott, and S. J. B. Yoo, "Optical Spectrally Sliced Transmitter for High Fidelity and Bandwidth Scalable Waveform Generation," *Journal of Lightwave Technology*, vol. 34, pp. 737–744, Jan. 2016.

[104] D. Drayss, D. Fang, A. Sherifaj, H. Peng, C. Füllner, T. Henauer, G. Lihachev, W. Freude, S. Randel, T. Kippenberg, T. Zwick, and C. Koos, "Optical Arbitrary Waveform Generation and Measurement (OAWG/OAWM) Enabling 320 GBd 32QAM Transmission," in *Conference on Lasers and Electro-Optics (CLEO)*, May 2023.